creative commons
COMMONS DEED

저작자표시-비영리-변경금지 2.0 대한민국

이용자는 아래의 조건을 따르는 경우에 한하여 자유롭게

- 이 저작물을 복제, 배포, 전송, 전시, 공연 및 방송할 수 있습니다.

다음과 같은 조건을 따라야 합니다:

저작자표시. 귀하는 원저작자를 표시하여야 합니다.

비영리. 귀하는 이 저작물을 영리 목적으로 이용할 수 없습니다.

변경금지. 귀하는 이 저작물을 개작, 변형 또는 가공할 수 없습니다.

- 귀하는, 이 저작물의 재이용이나 배포의 경우, 이 저작물에 적용된 이용허락조건을 명확하게 나타내어야 합니다.
- 저작권자로부터 별도의 허가를 받으면 이러한 조건들은 적용되지 않습니다.

저작권법에 따른 이용자의 권리는 위의 내용에 의하여 영향을 받지 않습니다.

이것은 이용허락규약(Legal Code)을 이해하기 쉽게 요약한 것입니다.

Disclaimer

dCollection

공학박사학위논문

내산화 코팅층의 기공 및 균열을 통해 침투한 산소에 의한 고온 산화 모델 개발

Modeling of High-Temperature Oxidation Through Pores and Cracks in Oxidation Protective Coatings

2023년 2월

서울대학교 대학원
기계항공공학부
한 다 빈

내산화 코팅층의 기공 및 균열을 통해 침투한 산소에 의한 고온 산화 모델 개발

Modeling of High-Temperature Oxidation Through Pores and Cracks in Oxidation Protective Coatings

지도교수 김 규 홍

이 논문을 공학박사 학위논문으로 제출함

2022년 11월

서울대학교 대학원

기계항공공학부

한 다 빈

한다빈의 공학박사 학위논문을 인준함

2022년 12월

위 원 장 _____

부위원장 _____

위 원 _____

위 원 _____

위 원 _____

Abstract

This study aims to develop improved models for predicting high-temperature oxidation through pores and cracks in oxidation protective coating layers. The oxidation protective layers are generally used to improve the ablation resistance of carbon-based materials vulnerable to oxidation in hypersonic flow environments. However, carbon substrates can be oxidized by oxygen penetrating through splits within the cracked coating or pores within the oxidized layer. The developed models aim to identify the oxidation resistance performance of oxidation-resistant coatings that protect carbon/carbon. The target coating materials are silicon carbide (SiC), hafnium carbide (HfC), and zirconium carbide (ZrC), and the temperature range of the model is from 1,000 °C or more to below the melting point of these materials. The model for cracks predicts the amount of carbon/carbon substrates oxidized by oxygen attack through coating cracks with the width of micrometer units and slots with width in millimeters. The model for pores predicts the oxide growth rate of oxidation-resistant coating caused by the oxidizer diffused into the carbide through the pores in the oxide.

The model for estimating the oxidation rate through cracks is developed based on the complete multi-component gaseous diffusion equation and considers the cavity growing in carbon substrates. The results obtained using the derived model are validated for both coatings with narrow cracks and wide slots with experimental results from the previously published paper. The weight loss by oxidation of C/C underlying SiC coating was measured in the temperature range of 1,000 °C to 1,300 °C, which is copying the thermal environment on the surface of re-entering Space Shuttle. The model results show good agreement with the test data while existing models predict the weight loss of the carbon composite as approximately half of or less than the measurements. Furthermore, the impact of each assumption used in the development of

the model is examined. Finally, oxidation characteristics according to the geometry of the crack and cavity and atmospheric conditions are investigated.

The model predicting the carbide coatings' oxide growth rate is developed based on the simplified version of the multi-component gaseous diffusion equation using the effective diffusion coefficient. The effective diffusion coefficient includes the Knudsen diffusion and the molecular diffusion, which reflect the influence of porous media. The results from the derived model are also validated with experimental results from the previously published paper. The oxide growth rates from the model show good agreement with the test data from 1,200 °C to 2,000 °C in air. Also, the model calculation agrees with the measurements from 1,200 °C to 1,600 °C in oxygen partial pressure of 0.02 atm and 1 atm. The effect of adjustable parameters of the model, such as porosity, pore radius, and tortuosity, on the calculation was researched.

Keywords: oxidation protective layer, metal carbide coating, coating crack, porous oxide layer, oxide growth, diffusion-controlled oxidation

Student Number: 2014-21895

Contents

List of Tables

List of Figures

Chapter 1

Introduction

1.1 Oxidation protective coating

Thermal protection system and materials

Hypersonic vehicles flying, such as space shuttles re-entering the Earth, re-entry capsules, or high-speed guided missiles, are subjected to extreme aerodynamic heating during flight. Due to aerodynamic heating, a high-temperature flow environment of thousands of K or more acts on the surface of the hypersonic vehicle. For example, it is known that the surface temperature of the space shuttle orbiter locally rises to 1,600 K during re-entry to Earth [1]. Because shock waves generated during the flight of an aircraft in the hypersonic region lead to energy loss and an increase in resistance, hypersonic weapons have a sharp shape to tackle this problem [2]. The sharper the shape, the larger the aerodynamic heating, and the temperature of a scramjet cruising at Mach 10 reaches 1,000–2,500 K at the nose tip and the leading edge of the wings [3]. In the case of the X-43a, it is known that the leading edge temperature reaches 1,900 K when flying at Mach 7 and 2,500 K when flying at Mach 10 [4]. There-

fore thermal protection system (TPS) is essential to protect the aircraft from such a high-temperature flow.

There are various thermal protection materials (TPM) for passive TPS, as shown in Fig. 1.1. TPM can be classified into metal-based, carbon-based, silicon-based, and the like. And depending on the material, it shows various types of high-temperature reactions. High-temperature reactions include mechanical ablation, such as shear erosion or spallation; chemical erosion, such as oxidation; phase change, such as melt-

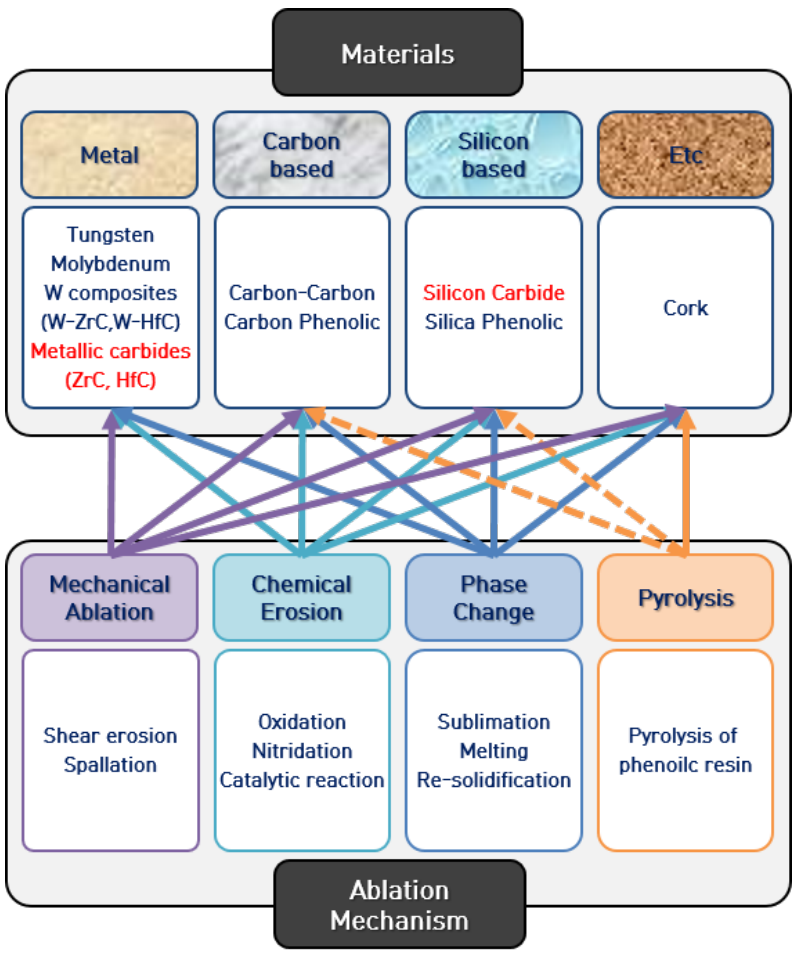

Figure 1.1: Thermal protection materials and thermal responses.

ing or sublimation; and pyrolysis of phenolic materials. Meanwhile, reusable materials, not ablative materials, must be used to reuse the spacecraft multiple times. Non-ablative materials are also appropriate for hypersonic weapons because ablation deforms the sharp leading edge, and the shape change of the control surface can decrease the maneuverability of the system. One of the most effective combinations of non-ablative TPM, which can bear up to 2,500K, is carbon/carbon (C/C) insulators coated with refractory oxidation-resistant ceramic coatings.

Oxidation-resistant coatings on carbon substrates

C/C composites have been commonly used for the thermal protection of re-entering vehicles. C/C composites are selected because of their suitable mechanical properties for high-temperature applications such as high thermal shock resistance, low thermal expansion, and lightweight. However, one critical disadvantage of C/C composites is their vulnerability to oxidation. C/C composites oxidize and can be consequentially ablated due to the oxidizing atmosphere at relatively low temperatures when compared with other thermal-protection materials. When carbon is ablated, a recession occurs, and the shape of the surface changes. When the carbon-based composite is coated adequately with an oxidation protective layer, oxidizing molecules cannot penetrate the coating, and their contact with the carbon-based composites is prevented. These oxidation-resistant layers are called coating layers because they are usually coated on the base material.

Silicon carbide (SiC) and Ultra-high-temperature ceramics (UHTCs) are refractory materials for oxidation protective coating. SiC, which has a history of being used on the nose cap and wing-leading edge of space shuttles [5, 6], is one of the most popular materials for the protective layer. Silica (SiO_2) forms on the surface during flight

and melts slightly under 2,000 K. So bulk SiC coating is suitable for hypersonic vehicles whose maximum surface temperature is estimated to be approximately 1,900 K. UHTCs developed for hypersonic applications include carbides, borides, and nitrides of Group 4-5 elements in the periodic table, such as hafnium carbide (HfC), zirconium carbide (ZrC), and tantalum carbide (TaC), hafnium diboride (HfB_2), and zirconium diboride (ZrB_2) [7]. The operating temperatures of UHTCs can be 1000 degrees higher than SiC based on the melting point listed in Table 1.1. Further, they have high hardness, high melting point, low vapor pressure, and excellent chemical resistance. HfC coating is known to be used on the leading edge of X-43a, and ZrB_2 based ceramic materials are widely investigated as potential TPMs for hypersonic space vehicle at the National Aeronautics and Space Administration (NASA) [8, 9]. Furthermore, HfC and diborides of group 4b elements (HfB_2, ZrB_2) are chosen as TPM for the European project, aero-thermodynamic loads on lightweight advanced structures (ATLLAS) program, at ONERA [10]. The oxidation-resistant coating con-

Table 1.1: Melting temperature of materials for oxidation protective layer.

Material	Melting temperature		
	Oxide (O_2)	Carbide (C)	Boride (B_2)
Silicon (Si)	1,713 °C (1,986 K)	2,830 °C (3,100 K)	
Zirconium (Zr)	2,715 °C (2,988 K)	3,532 °C (3,805 K)	$\sim$ 3,246 °C ($\sim$ 3,520 K)
Hafnium (Hf)	2,758 °C (3,031 K)	3,900 °C (4,170 K)	3,250 °C (3,520 K)

sisting of those refractory materials prevents oxygen penetration into the base material by the following principle. In the case of a protective layer, it can react with oxygen to form an oxide layer and maintain its shape, as shown in Fig 1.3, in contrast to carbon material which is ablated when it reacts with oxygen, resulting in recession and shape change. The oxide layer created at this time becomes another oxidation-resistant layer and protects the substrate and the existing protective layer.

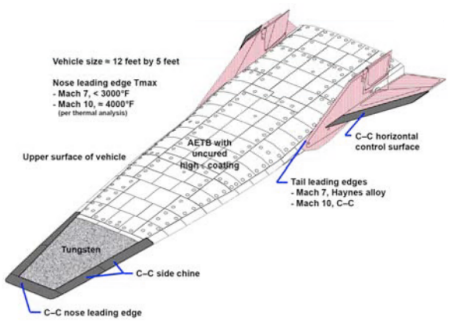

(a) X-43A: reprinted from [4].

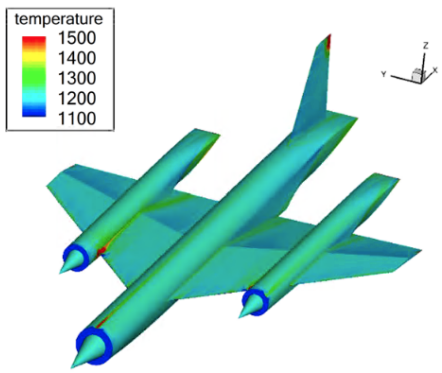

(b) ATLLAS program: reprinted from [10].

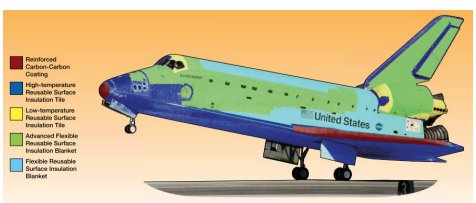

(c) Space shuttle orbiter: reprinted from [5].

(d) Falcon hypersonic space vehicle: reprinted from [7].

Figure 1.2: Hypersonic applications of UHTC coatings.

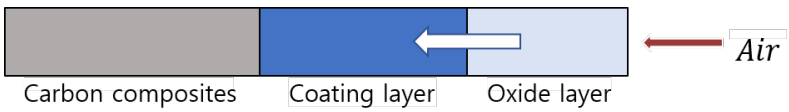

Figure 1.3: Illustration of growing oxide layer.

Anti-oxidation failure

There are three mechanisms of anti-oxidation failure of the coating: melting of the protective layer, oxidation through the through-thickness crack, and oxidation through the oxide layer. When the surface temperature reaches the material's melting point, the coating melts, and the molten layer is swept away by the flow. As a result, the base material is exposed to flow, and the coating layer does not function properly. In the temperature below the melting points, the pores and cracks shown in Fig. 1.4 can be a path of oxygen attack into substrates. When defects, such as cracks, in the layer, the carbon substrate can be oxidized because the gaps act as pathways for the penetration of oxygen molecules into the carbon–SiC interface [11]. In this case, the carbon under the crack is oxidized, and a cavity is created at the same time, and when this cavity grows, it affects the mechanical properties of the base material or the adhesion with the coating. Finally, suppose all the oxidation-resistant layers are oxidized since oxygen can permeate into the oxide layer, and the thickness of the oxide layer increases as the time exposed to the high-temperature flow increases. In that case, oxygen can permeate to the underlying material, and ablation may occur, then the coating layer may fall due to weak bonding at the interface [11].

The coating turns into an oxide layer by two representative mechanisms: thermal (static) oxidation and dynamic oxidation. Thermal oxidation is mainly utilized to make a SiO_2 layer in the semiconductor manufacturing process. Oxygen molecules

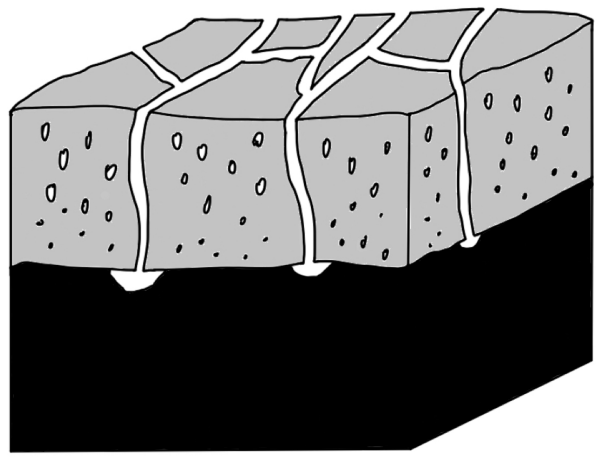

Figure 1.4: Cracks and pores in protective layer.

are absorbed on the surface of SiO_2 and propagated by atomic diffusion inside the solid. Various Deal-Grove models [12, 13] are fitted to experimental data and utilized to predict the thermal oxidation rate. A cristobalite oxide layer is created with a thickness growth rate of nanometers per hour during thermal oxidation, and that nominal growth rate can be neglected for hypersonic applications. Dynamic oxidation is observed in a high-temperature flow environment such as a plasma wind tunnel or hypersonic flight condition. It shows a much higher oxidation rate than thermal oxidation because it is caused by gaseous molecular diffusion, which is much faster than atomic diffusion. When carbide coatings such as SiC, HfC, and ZrC turn into an oxide layer, amorphous oxide layers with pores are created, and the pores become the path of molecular diffusion inside the porous media [14]. Then the thickness of the oxide layer gradually increases due to oxygen penetrating through the pores. When boride coatings such as HfB_2 and ZrB_2 turn into an oxide layer, different thermal phenomena occur depending on the surface temperature [15, 16]. An amorphous oxide layer

is formed, as in the case of carbide coating, and gaseous boron trioxide (B_2O_3) is created as the product at temperatures over 1,800C. However, liquid phase B_2O_3 filling the pores and evaporated gas phase B_2O_3 coexist at temperatures between 1,000 °C and 1,800 °C. Gaseous diffusion in the porous oxide layer and oxygen permeation through liquid B_2O_3 can be the oxidation path.

1.2 Researches on oxidation through cracks and oxides

Experimental researches on oxidation through crack

Through-thickness cracks can be formed owing to thermal expansion mismatch between the coating layer and carbon composites, damage to the material during operation [17], or contamination on the surface [18]. Therefore, various studies have been conducted to suppress crack formation: SiC coatings with various fibers such as C/SiC [19, 20], conversion coatings with crack healing effects [21, 22], mechanisms of damage to SiC [17, 23, 24]. Nevertheless, the problem of cracking in the coating layer still exists, especially when the coating is thick or the layer is coated on a big or curved part. The coating layers adapted to the surface of the hypersonic vehicles are much thicker than other general coatings on the surface of other applications. Usually, even if it exceeds 100 microns, it belongs to a very thick coating, but in the case of the space shuttle, for instance, the thickness of the coating layer ranges from 0.5 to 1.5 mm [25, 17, 26], which is more like a 'layer' than a 'coating.' The thicker the coating, the higher the possibility of the occurrence of cracks or detachment of the coating layer, so prediction of oxidation through cracks becomes essential.

Studies on oxidation attacks through coating cracks, slots, and pinholes have been conducted to understand the mechanism of attacks and predict the degree of oxida-

tion under the assumption of the existence of coating cracks. Various descriptions for coating cracks were characterized and measured by [27]. Parameters to account for material information, such as coating thickness and crack width, which is described in Fig. 1.5a, have been proposed and used in subsequent studies. Jacobson et al. investigated carbon consumption due to the oxidation attack through coating pinholes [11] and artificial slots with comparatively wide crack widths and naturally formed craze cracks with narrow widths [28, 29]. They reported that voids (or cavities) were formed under openings, and their formation varied with respect to the furnace temperature. C/C composites consist of two types of carbon: carbon fibers and carbon

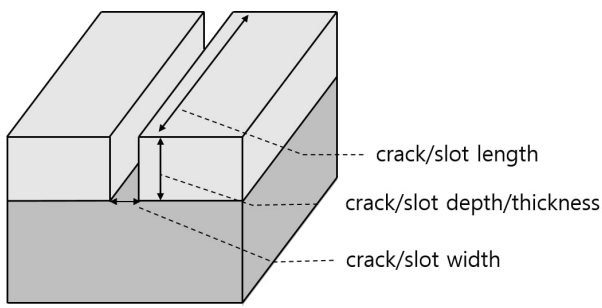

(a) Diagram showing crack length, thickness, and width.

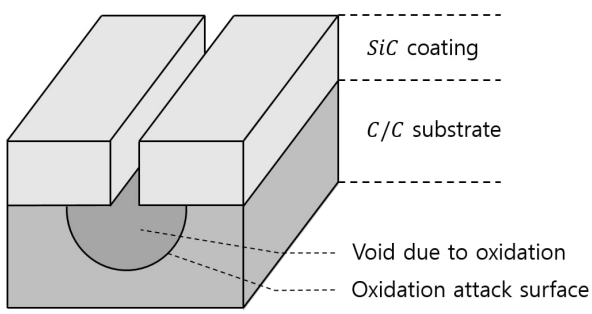

(b) Illustration of void formation by oxidation attack through SiC coating crack.

Figure 1.5: Illustration of crack and void.

matrix. At low temperatures, only the matrix material was oxidized; therefore, no void was observed under the coating. However, there was weight loss at 600 °C. At a higher temperature range of approximately 1,000–1,400 °C, the voids under pinholes and slots were formed in the shape of a hemisphere and semi-cylinder, respectively, as shown in Fig. 1.6. The surface of the carbon substrate was uniformly oxidized, and no preferential oxidation of the carbon matrix was observed at this regime (see also [30]). Moreover, the oxidation rate at this temperature range was controlled by diffusion through the trough. At a significantly higher temperature of approximately 1,600 °C, the coating system was also attacked.

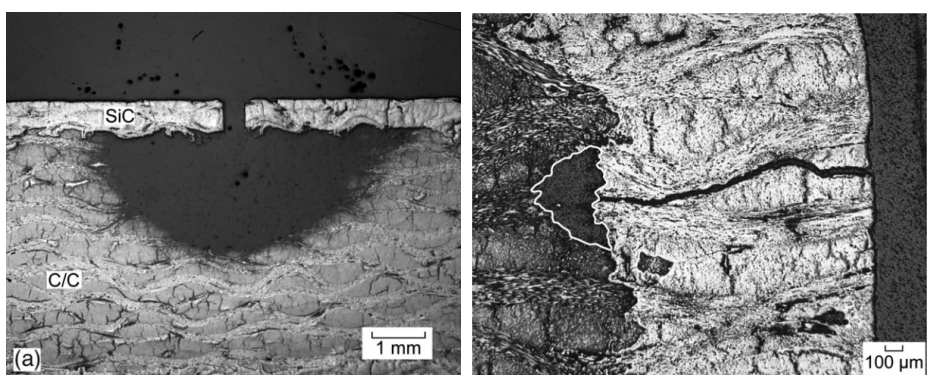

(a) Cavity formed under artificial crack. (b) Cavity formed under natural crack.

Figure 1.6: Cavity formed under cracks: reprinted from [29].

Experimental researches on oxidation through oxide layer

Studies on oxidation attacks through micropores inside the oxidized oxidation protective coating layer have been conducted to understand the mechanism of attacks and predict the degree of oxidation. Wang performed oxyacetylene torch ablation experiments on coated coatings with HfC [31]. Initially, HfC was oxidized to form a porous HfO_2 layer on the surface. After the oxide layer is formed, oxygen penetrating the HfO_2 layer reacts with the HfC layer to form a HfC_xO_y layer between the HfO_2 layer and the HfC layer. And when the oxide layer is heated above the melting point of HfO_2, the HfO_2 layer on the surface melts. The HfC_xO_y layer, the HfO_2 oxide layer and the molten layer inhibit oxygen diffusion, thereby delaying the ablation of the HfC layer. In this study, an experiment was performed to heat the specimen for about 60 seconds with an oxyacetylene torch supplying 0.4 MPa oxygen at 0.42 L/s. As a result, an oxide layer with a thickness of about 60 to 80 μm was produced. Wang produced coatings in three different ways according to the deposition parameters and then tested each coating's oxidation resistance performance [32]. As a result, it was confirmed that depending on the method of coating the composite material with the oxidation-resistant layer, a difference in the oxidation resistance performance of the coating could be more than three times.

Holcomb measured the rate of formation of an oxide layer in the range of 1200-1530 for HfC under oxygen partial pressures of 0.02, 0.21, and 1 atm when the total atmospheric pressure was one [33]. As a result, as the oxide layer becomes thicker, the oxidation rate slows down and tends to increase parabolically. And the parabolic weight gain rate was measured in the range of 10^{-7} to $10^{-5.5}$ $g^2/(cm^4 - s)$ depending on the oxygen partial pressure. The porosity of the formed oxide layer was

about 0.02, the radius of the developed pores was about 0.01 microns around the boundary between carbide and oxide, and the average value of the entire oxide layer was much larger, but not explicitly mentioned. Unlike Wang's study, there was no significant HfCxOy layer between the carbide and oxide layers. HfCxOy can be ignored when micrometer–size pore allows greater oxidation in inter-layer [34]. Yoo [35] studied the oxidation resistance of HfCs coated with 110 micrometers using the vacuum plasma spray coating method. As a result of heating for 60 seconds with a torch, the surface temperature was increased to 2000 C for 20 seconds and then maintained constant for 40 seconds. An oxide layer of about 36 micrometers was formed during the experiment.

Researches on oxidation model

In general, improved models based on the Deal-Grove (DG) model are widely used to predict the oxidation of oxidation-resistant coatings [12, 13]. DG model shows good agreement with test data in the range of temperature (700°–1300°C), partial pressure (0.1–1.0 atm), and oxide thickness (300–20000 Å). However, these are based on thermal-oxidation kinetic, not the kinetics of molecular diffusion, so the model is mainly used to predict and thermal oxidation of silicon in semiconductor device fabrication. In addition, since the growth rate of the oxide layer produced by thermal oxidation is extremely low, it can be ignored when predicting the formation of the oxide layer in the flight environment. For example, the diffusion rate is about 10,000 times greater during dynamic oxidation than during static oxidation. Therefore, to analyze oxygen permeation through a thick oxide layer with pores, it is recommended to use a model that considers physics such as diffusion through liquid B_2O_3 and molecular diffusion through pores in the porous oxide layer.

Various studies to predict oxide growth rates by oxidation through pores in the oxide layer have also been conducted. Bernstein et al. [36] derived the kinetics of the diffusion-limited oxidation-undercut process of a sacrificial layer of carbon based on the following five assumptions:

1. All gases are perfect ideal gases.

2. Binary gaseous diffusion coefficients are independent of mole fractions inside a channel.

3. Oxidation rate is controlled by the diffusion of gases penetrating the trough, and the kinetics can be studied using steady-state gas concentration profiles.

4. Oxygen and carbon monoxide do not coexist in the temperature range of interest, dividing the path into two distinct regions: inner zone with CO and CO_2 gases and outer zone with O_2 and CO_2 gases (see Fig. 2.1).

5. Oxidation of the carbon is faster than the process of diffusion.

These kinetics were applied to the counter-current gaseous diffusion model to describe the oxidation of porous conversion coating such as HfC turning into HfO_2 between 1,200 °C and 1,530 °C [37, 38]. Later, Jacobson et al. (1999) [11] applied the model to describe the oxidation of C/C composites through pinholes in SiC coatings. Jacobson et al. (2008) [29] also proposed a more detailed model for the oxidation of substrates through slots and craze cracks on the coating. The cavity growing at the C/C composites below the coating crack opening (Fig. 1.5b) was included in the diffusion path when deriving the oxidation model. The void was assumed to be cylindrical. Subsequently, the developed model was used in additional studies [39, 40]. In the studies mentioned above, reactions at the surface of graphite and a position

termed the “flame front [38]”, where oxygen and carbon monoxide react, were considered (see Fig. 2.1) and flux equations were derived for both inner and outer regions. Subsequently, solutions of the equations led to the carbon consumption rate. The significant differences between these models are the selection of the composition of gaseous species, geometry of the diffusion paths, consideration of the Knudsen diffusion, and the coordinate systems. Comparisons of the predicted oxidation rate or carbon consumption rate from the model to experimental results usually indicate the model’s effectiveness. Models to predict oxide growth by oxidation through liquid B_2O_3 are also developed by Parthasarathy, et al. [15, 16, 41, 42].

1.3 Motivation

Fig. 1.7 is a flowchart for thermal analysis of UHTC-coated C/C. Suppose the oxidation protective coating is detached or the surface temperature reaches the melting temperature. In that case, a recession occurs, and various models exist for predicting the recession rate by these phenomena. However, these models are suitable for analyzing ablative TPS and not applicable to non-ablative TPS. Therefore, a model capable of predicting the oxidation-preventing performance of the oxidation layer is needed to design TPS for maneuverable and controllable hypersonic vehicles efficiently. Also, it is necessary to predict how the cracks and pores in the coating will allow oxygen penetration to predict the oxidation-preventing performance. However, previously published models that simulate oxidation by oxygen penetration through cracks and oxide layer formation by oxygen penetration through pores show significant errors when compared with the test. Therefore, a new model that can predict similar values to the experiment is needed.

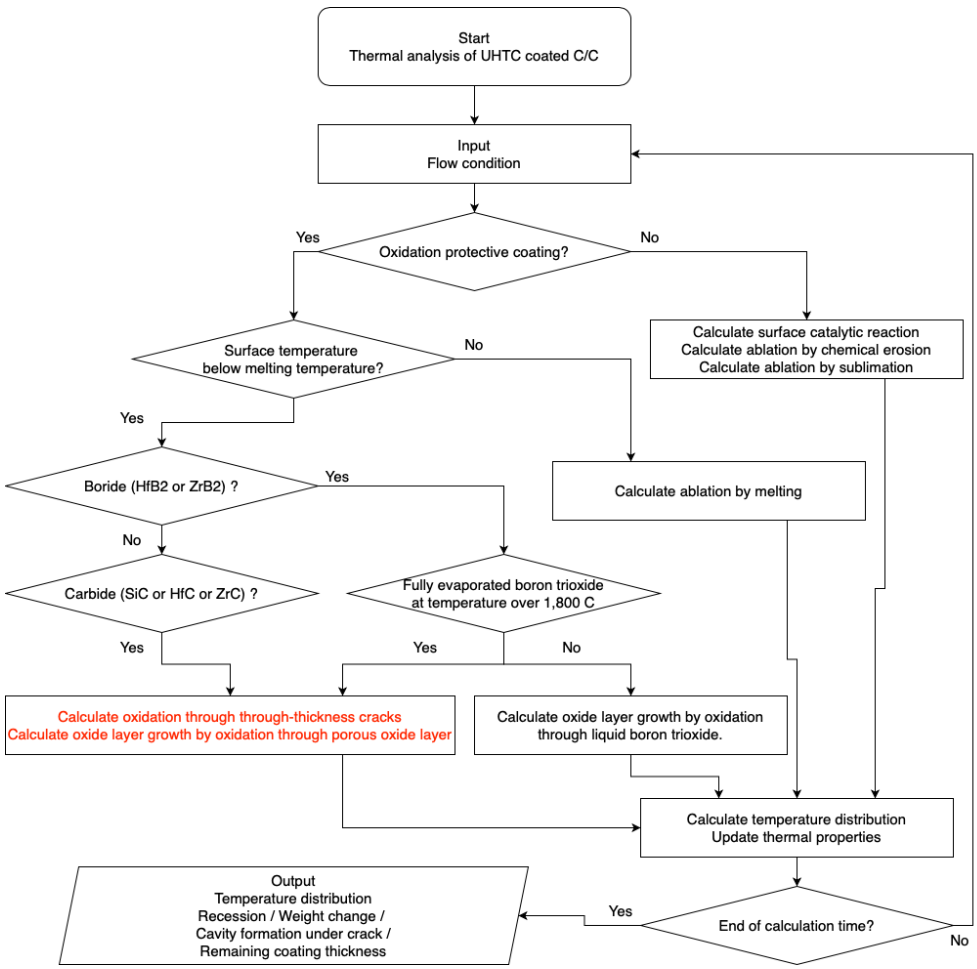

Figure 1.7: Flowchart for thermal analysis of UHTC coated C/C.

In the case of oxidation through craze cracks and slots, the calculation predicted a carbon weight loss rate significantly lower than the measured rate [29]. The measured weight loss rates were 2–4 times larger than those obtained through model calculations. First, molar flux and mass flux were misused in the development process. The model was developed from a binary diffusion equation, so it does not reflect flow obstruction by nitrogen. In addition, the position of the flame front was fixed at the initial situation, so the path length of the inner and outer zones was mispredicted. Zhou et al. [40] attempted to make a model whose calculation matched the experimental results but still needed to revise the model based on physics. Some factors, which do not reflect physical phenomena, were added to the previous model. The modeling procedure is thoroughly examined in the present study, and a more detailed and physically suitable oxidation model through coating slots or cracks is presented. The counter-current gaseous diffusion model is newly developed with four significant improvements:

1. Model is developed from Maxwell-Stefan (MS) diffusion equations;
2. Flame front position is released and moves inward as the void grows;
3. Flame front can be located inside the cavity because the cavity can be deeper than the thickness of the coating;
4. Impact of diffusion through the gap between the wide slot and cavity is considered.

Then the parametric study on the geometry of the crack and the atmospheric conditions is conducted.

The model for oxidation through pores inside the oxide coating layer is also im-

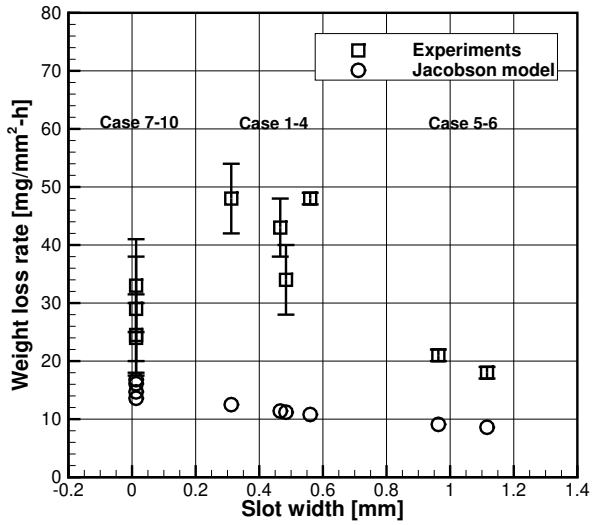

(a) Cases 1–10.

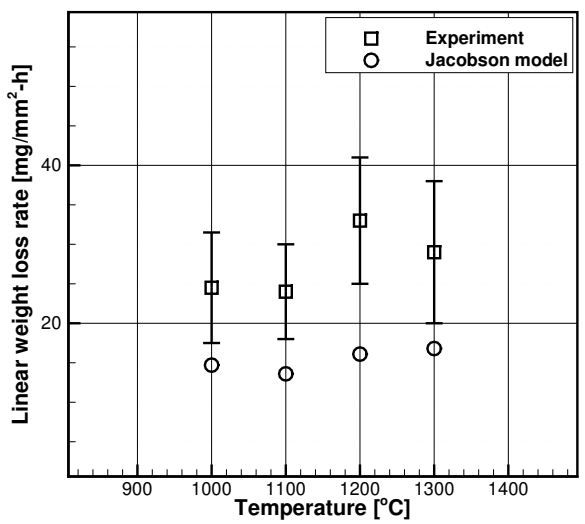

(b) Cases 7–10.

Figure 1.8: Comparison between Jacobson's model and test data.

proved. The model from Holcomb [33, 38] is compared with the experimental result. The primary input for the model was the radius. The pore radius in the oxide layer

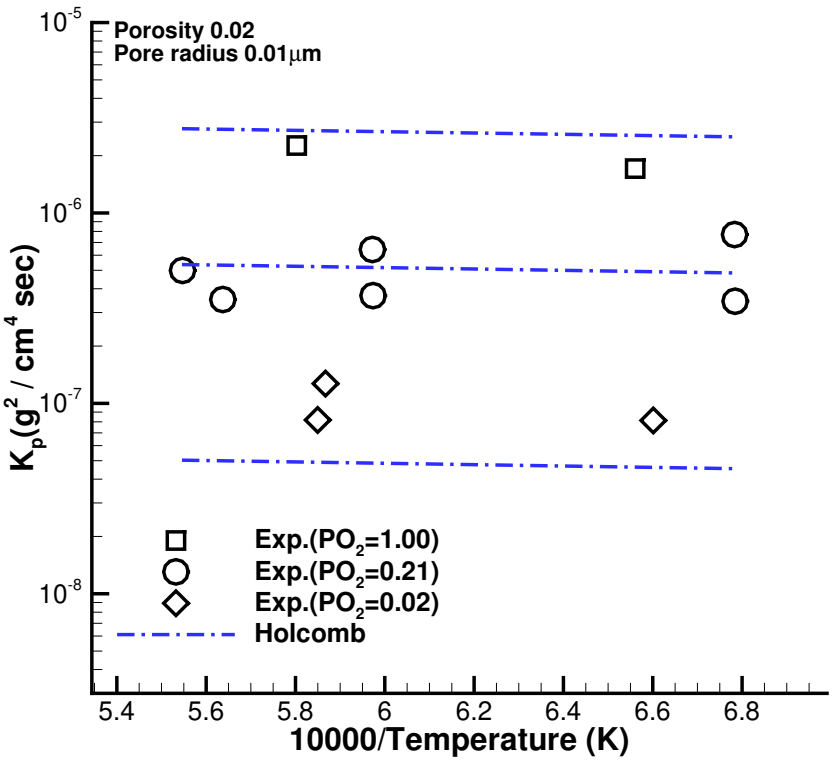

Figure 1.9: Comparision between Holcomb's model and test data.

near the carbide-oxide interface was 0.01 microns, and the average pore radius from hafnium oxide was much larger than 0.01 microns. However, the model calculation using the value of 0.01 microns for the pore radius fits the result with the experimental data. Through this result, the authors suggested that oxygen diffusion through the pores is mainly affected by the pores located on the carbide interface. However, since the model uses the average pore radius for the entire depth of the oxide layer, the

diffusion through pores model should agree with the experiment when the average size of pores inside the oxide layer is input to reflect the diffusion inside the oxide layer well physically. Thus the model over-predicts the oxygen diffusion through the oxide layer. In contrast to the model for the oxidation through the crack, model development from the entire MS equation was impossible because the porous media effect should be included. Then the equations during the model development process seem right, but the effective diffusion coefficient was revised in this study. Then the survey of the influence of parameters such as pore radius, porosity, and tortuosity is investigated. Further, in the case of metal carbides, it can be used even at a high temperature of 2000K or higher where dissociated oxygen atoms, not oxygen molecules, may exist on the surface. The degree of diffusion increase when dissociated atoms are introduced was also studied.

Chapter 2

Modeling for Oxidation Through Cracks

2.1 Counter-current gaseous diffusion model

Many studies on the application of the counter-current gaseous diffusion model have been performed to describe the oxidation damage to substrates under the protective layer [43, 11, 29, 44, 45, 39, 40, 46]. The schematic diagram of the counter-current diffusion process in the crack or slot considered in the present study is illustrated in Fig. 2.1. The counter-current diffusion model consists of two zones because of the incompatibility between O_2 and CO gases. In the zone near the substrate, gaseous species CO, CO_2, and N_2 exist. CO_2 diffused inward to the carbon substrate, and the carbon substrate is oxidized. Subsequently, the reaction releases CO, which moves outward. The reaction at the oxidation attack surface is Eq. (2.1).

$$C(s) + CO_2(g) = 2CO(g) \tag{2.1}$$

The carbon fiber structure can be neglected when predicting oxidation at the surface of the carbon substrate at a high temperature over 1,000°C, so uniform oxidation of carbon substrate is assumed. Gaseous species in the outer region near the surface are

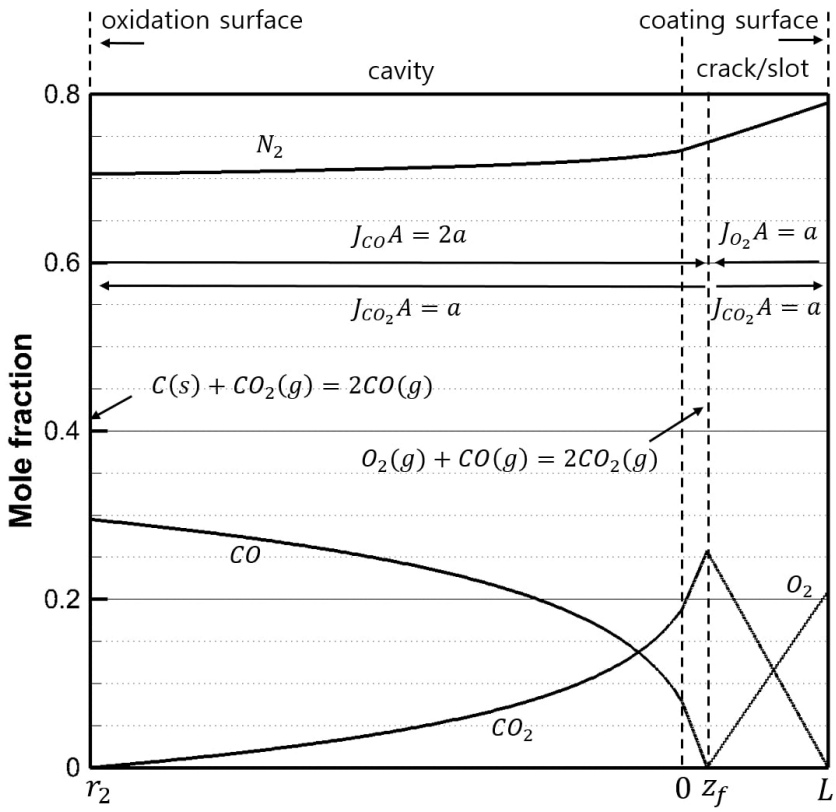

Figure 2.1: Diagram of diffusion process in crack/slot and cavity.

O_2, CO_2, and N_2. Between the substrate-side region and the surface-side region, O_2 and CO react to form CO_2, and that position is termed the "flame front."

$$O_2(g) + 2CO(g) = 2CO_2(g) \tag{2.2}$$

Then the overall reaction is

$$O_2(g) + C(s) = CO_2(g). \tag{2.3}$$

Let region I denote the outer zone near the surface, region II be the inner zone near the oxidation surface, and $J^I_{O_2}$ be the molar flux (in moles/unit area-time) of O_2 in region I. Then $J^I_{CO_2}$ and $J^I_{O_2}$ have the same magnitude but opposite directions.

Note that J is presented in a fixed coordinate system. In region II, J^I_{CO} is double of $J^I_{CO_2}$, and they are in opposite directions. The molar fluxes of CO_2 in regions I and II have the same magnitude but opposite directions. The reaction Eq. (2.1) and the mass balance between CO and O_2 at the flame front are used to obtain the relation between molar fluxes in both regions:

$$J^{II}_{CO}/2 = -J^{II}_{CO_2} = J^I_{CO_2} = -J^I_{O_2} = a. \tag{2.4}$$

The molar flux of N_2 is zero along the path of diffusion. In Eq. (2.4), a is equal to the rate of carbon oxidized (in moles/unit area-time). The product of the species molar flux J and area A (in moles/time) is constant along the path as presented in Eq. (2.5).

$$\frac{\partial J_i}{\partial z} = 0 \text{ (in the crack or slot) or } \frac{\partial \left(r J_i\right)}{\partial r} = 0 \text{ (in the cavity)} \tag{2.5}$$

where z denotes the distance from the carbon-coating interface to the coating surface inside the coating crack or slot and r is the distance from the interface to the void surface inside the cavity, as depicted in Fig. 2.2 and 2.3.

From the definition of the mole fraction, the sum of mole fractions of each species equals 1.

$$\sum x_i = 1 \tag{2.6}$$

Here x_i denotes the molar fraction of species i. The boundary conditions for each region are presented along with the development of equations.

Diffusion equations

The simplified Maxwell–Stefan (MS) equation [47] has been used for many calculations of diffusion in gaseous mixtures. The molar flux of gas species i, J_i, is defined for a fixed coordinate system as Eq. (2.7), where the first and second terms on the right-hand side are the diffusive and the convective terms, respectively. However, in this study, to better understand the mechanism inside the crack and void and to develop a more realistic model, equations were derived using the original MS equation. The simplified equation ignores the gradient of N_2 and can only consider the binary diffusion between CO_2 and O_2 in the outer region and the binary diffusion between CO and CO_2 in the inner area. But the complete equation considers the multi-component effect (ternary diffusion for this model), including N_2. The original form of the MS equation used in this study is given as Eq. (2.8) [48].

$$J_i = -cD_{i,N_2}\left(\frac{\partial x_i}{\partial z}\right) + x_i \sum_j J_j \tag{2.7}$$

$$\nabla x_i = -\sum_{j=1}^{N} \frac{1}{cD_{i,j}} \left(x_j J_i - x_i J_j\right) \tag{2.8}$$

In these equations, c is the total sum of gaseous concentration and $D_{i,j}$ is the gas phase inter-diffusion coefficients between species i and j are calculated using the Chapman–Enskog theory [49]:

$$D_{i,j} = 1.8583 \times 10^{-3} \frac{T^{3/2}}{P\sigma_{ij}^2 \Omega_{i,j}} \left(\frac{1}{M_i} + \frac{1}{M_j}\right)^{1/2} \tag{2.9}$$

where $D_{i,j}$ is in cm^2/s, M_i is the molecular weight of species i in g/mol, T is the absolute temperature in K, and P is the pressure in atm. Parameter Ω_{ij} is the collision integral for diffusion, a dimensionless quantity tabulated as a function of dimensionless temperature kT/ϵ_{ij}. Parameter σ is the collision diameter and ϵ is

the maximum energy attraction; these are interaction parameters appearing in the Lennard–Jones 6–12 potential between one molecule of i and one of j. Parameter σ_{ij} is the arithmetic mean of pure components $\sigma_{ij} = (\sigma_i + \sigma_j)/2$, and ϵ_{ij} is the geometric mean of components $\epsilon_{ij} = \sqrt{\epsilon_i \epsilon_j}$. Parameters σ, ϵ and the value of Ω according to the value of kT/ϵ used in this study are shown in Table. A.1 and A.3. Parameter k is Boltzmann's constant.

2.2 Model with flame front located inside the crack

First, this section shows the model development for the case when the flame front is inside the crack. The coordinate system for this section is depicted in Fig. 2.2). The region between $r = 0$ and $r = r_1$ is ignored. The path is divided into three regions. Region I is the outer region, and regions II and III are inner regions inside the crack and the void, respectively. In region I, Eq. (2.10) can be obtained by introducing $J_{N_2} = 0$ into Eq. (2.8).

$$\frac{\partial x_{N_2}}{\partial z} = \frac{1}{c}\left(\frac{1}{D_{N_2O_2}} - \frac{1}{D_{N_2CO_2}}\right) x_{N_2} J^I_{O_2} \tag{2.10}$$

Because the molar flux is constant, Eq. (2.11) is given by Eq. (2.10).

$$\frac{\partial J_{O_2}}{\partial z} = \frac{\partial}{\partial z}\left(\frac{cD^{\text{eff}}_{N_2}}{x_{N_2}}\frac{\partial x_{N_2}}{\partial z}\right) = 0 \tag{2.11}$$

$D^{\text{eff}}_{N_2}$ is defined as $D^{\text{eff}}_{N_2} = (1/D_{N_2O_2} - 1/D_{N_2CO_2})^{-1}$. With proper boundary conditions, x_{N_2}=$x_{N_2,L}$ at $z = L$ and x_{N_2}=x_{N_2,z_f} at $z = z_f$, x_{N_2} is obtained as Eq. (2.12).

$$x_{N_2} = x_{N_2,L}\left(\frac{x_{N_2,z_f}}{x_{N_2,L}}\right)^{\frac{L-z}{L-z_f}} \tag{2.12}$$

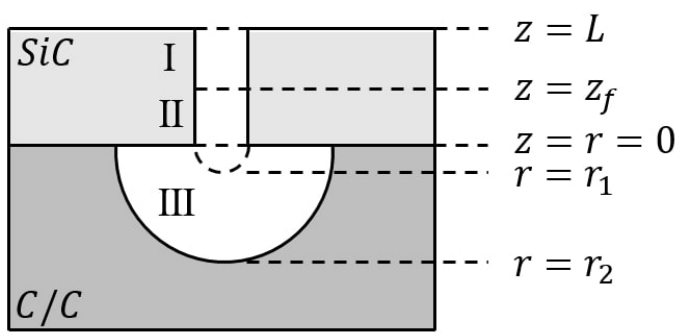

Figure 2.2: Coordinate description: flame front inside the crack.

When Eqs. (2.11-2.12), the relations $x_{N_2,z_f} + x_{CO_2,z_f} = 1$ and $x_{N_2,0} + x_{O_2,L} = 1$ are combined, and J_{O_2} becomes Eq. (2.13).

$$J^I_{O_2} = cD^{\text{eff}}_{N_2} \ln \left(\frac{1 - x_{CO_2,z_f}}{1 - x_{O_2,L}} \right) \frac{1}{z_f - L} \tag{2.13}$$

Similarly, the relation for O_2 is given as Eq. (2.14).

$$\frac{\partial x_{O_2}}{\partial z} = -\frac{1}{c} \left(\frac{x_{N_2}}{D_{O_2N_2}} + \frac{1 - x_{N_2}}{D_{O_2CO_2}} \right) J_{O_2} \tag{2.14}$$

By combining Eqs. (2.10,2.12,and 2.14) , J_{O_2} can be eliminated and $\partial x_{O_2}/\partial z$ is obtained as Eq. (2.15).

$$\frac{\partial x_{O_2}}{\partial z} = -\frac{\dfrac{x_{N_2,L} \left(\frac{x_{N_2,z_f}}{x_{N_2,L}} \right)^{\frac{L-z}{L-z_f}}}{D_{O_2N_2}} + \dfrac{1 - x_{N_2,L} \left(\frac{x_{N_2,z_f}}{x_{N_2,L}} \right)^{\frac{L-z}{L-z_f}}}{D_{O_2CO_2}} \dfrac{\ln \left(x_{N_2,z_f} / x_{N_2,z_f} \right)}{z_f - L}}{\dfrac{1}{D_{N_2O_2}} - \dfrac{1}{D_{N_2CO_2}}} \tag{2.15}$$

Integrating Eq. (2.15) with respect to z and introducing relations $x_{O_2,L} + x_{N_2,L} = 1$, $x_{CO_2,z_f} + x_{N_2,z_f} = 1$ gives the relation between x_{CO_2,z_f} and $x_{O_2,L}$ (Eq. (2.16)).

$$x_{O_2,L} = \frac{\dfrac{\left(x_{O_2,L} - x_{CO_2,z_f} \right)}{D_{O_2N_2}} + \dfrac{\ln \left(\dfrac{1 - x_{CO_2,z_f}}{1 - x_{O_2,L}} \right) - \left(x_{O_2,L} - x_{CO_2,z_f} \right)}{D_{O_2CO_2}}}{\dfrac{1}{D_{N_2O_2}} - \dfrac{1}{D_{N_2CO_2}}} \tag{2.16}$$

Next, x_{CO_2,z_f} can be calculated by solving this equation (Table 2.1, x_{CO_2,z_f} from ternary relation).

In Region II the gradient of x_{CO_2} is expressed as Eq. (2.17).

$$\frac{\partial x_{CO_2}}{\partial z} = -\frac{1}{cD_{CO_2N_2}} \left(x_{N_2} J_{CO_2} \right) - \frac{1}{cD_{CO_2CO}} \left(x_{CO} + 2x_{CO_2} \right) J_{CO_2} \tag{2.17}$$

Table 2.1: x_{CO_2,z_f} values from the binary and ternary assumption ($x_{O_2} = 0.21, P = 1\mathrm{atm}$).

Temperature (°C)	x_{CO_2,z_f} (binary relation)	x_{CO_2,z_f} (ternary relation)	difference (%)
1000	0.2706	0.2537	6.7
1100	2.2707	0.2538	6.7
1200	0.2714	0.2543	6.7
1300	0.2722	0.2548	6.8

As the maximum difference between two diffusion coefficients was less than 1% in the temperature range of this study, the effective coefficient can be used as follow: $D^{\text{eff}}_{CO2} \approx D_{CO_2N_2} \approx D_{CO_2CO}$ [50]. Subsequently, the equation becomes Eq. (2.18).

$$\frac{\partial x_{CO_2}}{\partial z} = -\frac{1}{cD^{\text{eff}}_{CO2}} \left(1 + x_{CO_2}\right) J^{II}_{CO_2} \tag{2.18}$$

The relation between z and x_{CO_2} can be induced by combining proper boundary conditions, $x_{CO_2} = x_{CO_2,0}$ at $z = 0$ and $x_{CO_2} = x_{CO_2,z_f}$ at $z = z_f$, with Eq. (2.19).

$$\frac{\partial J^{II}_{CO_2}}{\partial z} = \frac{\partial}{\partial z}\left(\frac{cD^{\text{eff}}_{CO_2}}{1 + x_{CO_2}} \frac{\partial x_{CO_2}}{\partial z}\right) = 0 \tag{2.19}$$

Next, $J^{II}_{CO_2}$ is obtained as Eq. (2.20) by substituting the result into Eq. (2.18).

$$J^{II}_{CO_2} = -cD^{\text{eff}}_{CO_2} \ln\left(\frac{1 + x_{CO_2,z_f}}{1 + x_{CO_2,0}}\right) \frac{1}{z_f} \tag{2.20}$$

Recalling relation $J^{II}_{CO_2} = J^{I}_{O_2}$, Eqs. (2.13) and (2.20) can be merged into one rela-

tion between z_f and $x_{CO_2,0}$ as Eq. (2.21).

$$-cD^{\text{eff}}_{CO_2} \ln\left(\frac{1+x_{CO_2,z_f}}{1+x_{CO_2,0}}\right)\frac{1}{z_f} = cD^{\text{eff}}_{N_2} \ln\left(\frac{1-x_{CO_2,z_f}}{1-x_{O_2,L}}\right)\frac{1}{z_f-L} \tag{2.21}$$

Let III denote the region inside the cavity. The radial gradient of x_{CO_2} in region III is expressed using the same equation as Eq. (2.18) for region II, representing r and III instead of z and II, respectively. The radial gradient of the steady state molar flux entering the area of cylindrical geometry is given by Eq. (2.22).

$$\frac{\partial\left(rJ^{III}_{CO_2}\right)}{\partial r} = \frac{\partial}{\partial r}\left(cD^{\text{eff}}_{CO_2}\frac{r}{1+x_{CO_2}}\frac{\partial x_{CO_2}}{\partial r}\right) = 0 \tag{2.22}$$

The relation between r and x_{CO_2} can also be derived from Eq. (2.22) using the following boundary conditions: $x_{CO_2} = x_{CO_2,r_1} = x_{CO_2,0}$ at $r = r_1$ (note that the region between $r = 0$ and $r = r_1$ is ignored in this section) and $x_{CO_2} = x_{CO_2,r_2} \approx 0$ at $r = r_2$. Note that the equilibrium constant of the wall reaction (Eq. (2.1)), P^2_{CO}/P_{CO_2}, is approximately 190–3,400 in the temperature range of 1,000–1,400 °C [51]. Therefore, it is reasonable to assume that CO_2 molecules hitting the wall react fully and x_{CO_2,r_2} can be approximated to zero. Substituting the relation into Eq. (2.18), the molar flux of CO_2 in region III can be derived using Eq. (2.23).

$$J^{III}_{CO_2} = cD^{\text{eff}}_{CO_2}\frac{\ln\left(1+x_{CO_2,r_1}\right)}{r\ln\left(r_2/r_1\right)} \tag{2.23}$$

There is a semi-circular section between positions $z = 0$ and $r = r_1$; this region is neglected in this process, but will be discussed later in sec. 2.3. Now the quantities at $z = 0$ are assumed to be equal to those at $r = r_1$. At this position, Eq. (2.24) is given as

$$J^{III}_{CO_2}A_{r_1} = -J^{II}_{CO_2}A_0. \tag{2.24}$$

Here $A_{r_1} = \pi r_1 l$ and $A_0 = wl$, where w and l are width and length of the crack, respectively . The sign of the right-hand side is reversed because the Cartesian and cylindrical coordinates are in opposite directions. By substituting Eqs. (2.20) and (2.23) into Eq. (2.24), $x_{CO_2,0}$ can be expressed as a function of r_2 and z_f (Eq. (2.25)).

$$\ln\left(1 + x_{CO_2,0}\right) = \frac{\ln\left(r_2/r_1\right)\ln\left(1 + x_{CO_2,z_f}\right)}{\ln\left(r_2/r_1\right) + \left(\pi z_f/w\right)} \tag{2.25}$$

$x_{CO_2,0}$ can be eliminated by inserting Eq. (2.25) into Eq. (2.21). Next, z_f is obtained as a function of r_2.

$$\frac{\pi z_f}{w} = \frac{-\ln\left(r_2/r_1\right) + \alpha\beta}{1 + \alpha} \tag{2.26a}$$

$$\alpha = \frac{D^{\text{eff}}_{CO_2}}{D^{\text{eff}}_{N_2}} \frac{\ln\left(1 + x_{CO_2,z_f}\right)}{\ln\left(\dfrac{1 - x_{CO_2,z_f}}{1 - x_{O_2,L}}\right)},\ \beta = \frac{\pi L}{w} \tag{2.26b}$$

Subsequently, $J^{III}_{CO_2}$ is obtained by inserting Eqs. (2.25) and (2.26a) into Eq. (2.23).

$$J^{III}_{CO_2} = \frac{cD^{\text{eff}}_{CO_2}\ln\left(1 + x_{CO_2,z_f}\right)}{r\left[\ln\left(r_2/r_1\right) + \beta\right]} \frac{1 + \alpha}{\alpha} \tag{2.27}$$

Assuming that most of CO_2 particles react with the carbon wall, weight the loss rate of carbon can be given by Eq. (2.28)

$$\left.\frac{dW_C}{dt}\right|_{r=r_2} = M_C J^{III}_{CO_2} A_{r_2} \tag{2.28}$$

where W_C denotes the weight of carbon substrate, M_C is the molecular weight of carbon. The recession rate of the void can be expressed as Eq. (2.29)

$$\frac{dV}{dt} = \frac{d\left(\pi r^2 l/2\right)}{dt} = \pi r l \frac{dr}{dt} \tag{2.29}$$

where V is the volume of the cavity. The relation between the recession rate of the cavity and J_{CO_2} flux is expressed as Eq. (2.30).

$$\frac{1}{\rho}\frac{dW_C}{dt}\bigg|_{r=r_2} = \frac{dV}{dt}\bigg|_{r=r_2} = \pi r_2 l \frac{dr_2}{dt} = \frac{M_C}{\rho} J^{III}_{CO_2} A_{r_2} \tag{2.30}$$

Here, ρ is the density of the C/C substrate. Eq. (2.30) can be used to predict weight change and cavity growth over time for a specific flight trajectory heating condition. On the other hand, for steady atmospheric conditions, the weight change and cavity radius for a particular time can be calculated using the integral model derived through the process below. By combining Eqs. (2.30) and (2.27), Eq. (2.31) is obtained.

$$r_2 \frac{dr_2}{dt} = \frac{M_C}{\rho} \frac{c D^{\text{eff}}_{CO_2} \ln\left(1 + x_{CO_2,z_f}\right)}{\ln\left(r_2/r_1\right) + \beta} \frac{1+\alpha}{\alpha} \tag{2.31}$$

By integrating Eq. (2.31), t from 0 to t and r from r_1 to r_2, a model of the time and cavity radius, r_2 can be obtained.

$$t = \frac{\rho}{2 M_C c D^{\text{eff}}_{CO_2} \ln\left(1 + x_{CO_2,z_f}\right)} \left[r_2^2 \ln\frac{r_2}{r_1} + \left(r_2^2 - r_1^2\right)\left(\beta - \frac{1}{2}\right) \right] \frac{\alpha}{\alpha+1} \tag{2.32}$$

Finally, the radius of the semi-cylindrical void at a specific time, r_2, is the only unknown and can be calculated using Eq. (2.32), and the void size can be converted into weight loss rate of the carbon substrate using Eq. (2.33).

$$\Delta W_C / At = \frac{1}{2}\rho\pi\left(r_2^2 - r_1^2\right)/wt \tag{2.33}$$

2.3 Model with flame front located inside the cavity

Note that the numerator in Eq. (2.26a) can be negative when $\ln(r_2/r_1)$ is greater than $\alpha\beta$ as r_2 increases. This signifies that the derived model may not be useful when the flame front is formed in the void. To make the model applicable to this situation, a model assuming that the flame front is inside the void is also described in this section. In this section, the region numbers and the position of the flame front in the cavity r_f are redefined, as depicted in Fig. 2.3. Region I is the outer region in the coating slot, region II is the outer region in the void, and region III is the inner region. The region between $r = 0$ and $r = r_1$ is ignored in this section.

In region I, Eqs. (2.34) and (2.35) can be obtained through a process similar to Eqs. (2.10-2.16), with the following boundary conditions: $x_{O_2} = x_{O_2,L}$ at $z = L$, $x_{O_2} = x_{O_2,0} \neq 0$ at $z = 0$.

$$J^I_{O_2} = -cD^{\text{eff}}_{N_2} \ln\left(\frac{x_{N_2,0}}{x_{N_2,L}}\right)\frac{1}{L} \tag{2.34}$$

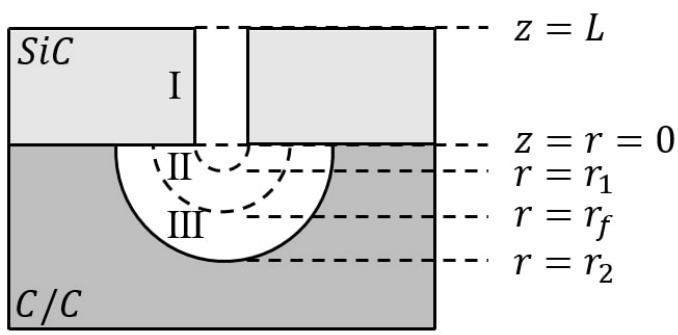

Figure 2.3: Coordinate description: flame front inside the cavity.

$$x_{O_2,L} - x_{O_2,0} = \frac{\dfrac{(x_{N_2,0} - x_{N_2,L})}{D_{O_2N_2}} + \dfrac{\ln(x_{N_2,0}/x_{N_2,L}) - (x_{N_2,0} - x_{N_2,L})}{D_{O_2CO_2}}}{\dfrac{1}{D_{N_2O_2}} - \dfrac{1}{D_{N_2CO_2}}} \tag{2.35}$$

The radial gradients of mole fractions in region II are expressed using the same equations for region I by representing r and II instead of z and I, respectively, as Eq. (2.36).

$$\frac{\partial\left(rJ_{O_2}^{II}\right)}{\partial r} = \frac{\partial}{\partial r}\left(cD_{N_2}^{\text{eff}}\frac{r}{x_{N_2}}\frac{\partial x_{N_2}}{\partial r}\right) = 0 \tag{2.36}$$

x_{N_2} can be obtained using Eq. (2.37) by integrating Eq. (2.36).

$$x_{N_2} = x_{N_2,r_1}\left(r/r_1\right)^{\gamma},\ \gamma = \frac{\ln\left(x_{N_2,r_f}/x_{N_2,r_1}\right)}{\ln\left(r_f/r_1\right)} \tag{2.37}$$

Next, combining Eqs. (2.37) and (2.10) gives Eq. (2.38).

$$J_{O_2}^{II} = cD_{N_2}^{\text{eff}}\frac{\ln\left(x_{N_2,r_f}/x_{N_2,r_1}\right)}{r\ln\left(r_f/r_1\right)} \tag{2.38}$$

Replacing x_{N_2} and J_{O_2} in Eq. (2.14) with Eqs. (2.37) and (2.38), respectively, gives the equation of radial gradient of x_{O_2}.

$$\frac{\partial x_{O_2}}{\partial r} = -D_{N_2}^{\text{eff}}\left(\frac{x_{N_2,r_1}\left(r/r_1\right)^{\gamma}}{D_{O_2N_2}} + \frac{1 - x_{N_2,r_1}\left(r/r_1\right)^{\gamma}}{D_{O_2CO_2}}\right)\frac{\gamma}{r} \tag{2.39}$$

The equation for x_{O_2,r_1} can be obtained by integrating Eq. (2.39) using following the boundary equation: $x_{O_2} = x_{O_2,r_f} = 0$ at $r = r_f$, $x_{O_2} = x_{O_2,r_1}$ at $r = r_1$.

$$x_{O_2,r_1} = \frac{\dfrac{\left(x_{N_2,r_f} - x_{N_2,r_1}\right)}{D_{O_2N_2}} + \dfrac{\ln\left(x_{N_2,r_f}/x_{N_2,r_1}\right) - \left(x_{N_2,r_f} - x_{N_2,r_1}\right)}{D_{O_2CO_2}}}{\dfrac{1}{D_{N_2O_2}} - \dfrac{1}{D_{N_2CO_2}}} \tag{2.40}$$

Summation of Eqs. (2.35) and (2.40) gives the equation of x_{co_2,r_f}, which is consistent with Eq. (2.16). Hence the position of the flame front has no impact on the value of x_{CO_2}. Combining Eqs. (2.34) and (2.38), the equation of x_{N_2,r_1} can be obtained.

$$\ln x_{N_2,r_1} = \frac{\dfrac{\pi L}{w}\dfrac{1}{\ln\left(r_f/r_1\right)}\ln x_{N_2,r_f} + \ln x_{N_2,L}}{1 + \dfrac{\pi L}{w}\dfrac{1}{\ln\left(r_f/r_1\right)}} \tag{2.41}$$

The relation between r and x_{CO_2} in region III can also be derived from Eq. (2.22) with the following boundary conditions: $x_{CO_2} = x_{CO_2,r_f}$ at $r = r_f$, $x_{CO_2} = x_{CO_2,r_2} \approx 0$ at $r = r_2$. Substituting the relation into Eq. (2.18), Eq. (2.42) can be derived.

$$J^{III}_{CO_2} = cD^{\text{eff}}_{CO_2}\frac{\ln\left(1 + x_{CO_2,r_f}\right)}{r\ln\left(r_2/r_f\right)} \tag{2.42}$$

Because $J^{III}_{CO_2} = J^{II}_{O_2}$ at $r = r_f$, Eqs.(2.38) and (2.42) are combined into Eq. (2.43).

$$D^{\text{eff}}_{CO_2}\frac{\ln\left(1 + x_{CO_2,r_f}\right)}{\ln\left(r_2/r_f\right)} = D^{\text{eff}}_{N_2}\frac{\ln\left(x_{N_2,r_f}/x_{N_2,r_1}\right)}{\ln\left(r_f/r_1\right)} \tag{2.43}$$

Merging Eq. (2.41) into Eq. (2.43), the relation between r_2 and r_f can be obtained as Eq. (2.44).

$$\ln\left(r_2/r_f\right) = \left(\ln\left(r_2/r_1\right) + \beta\right)\alpha/\alpha + 1 \tag{2.44}$$

$J^{III}_{CO_2}$ can be obtained by inserting Eq. (2.44) into Eq. (2.42). It is in the same form as Eq. (2.27). Next, this equation is substituted into Eq. (2.30) to obtain an equation that is the same as Eq. (2.31). Therefore, the model assuming that the flame front is inside the void matched the model that assumed that the flame front is inside the crack.

2.4 Model with the intermediate space

In case of wide slots, as in Fig. 2.4, the intermediate space R_3 between $z = 0$ and $r = r_1$ should be considered because the diffusion path occupied by this gap is considerable compared to the coating thickness and cavity size. It can be inferred that the mole fractions are constant along the $r = r_1$ line when the crack width is extremely small (Fig. 2.5a); however, the mole fractions may not be constant along the curve when the slot width is not small, because the diffusion may not be radial, as illustrated in Fig. 2.5b. Therefore, the gas diffusion paths leading to $r = r_1$ are separately calculated by dividing the line with infinitesimal areas, as depicted in Fig. 2.6.

Equations for the R_3 region are derived in quasi-1D coordinates. The ζ axis represents the distance from $z = 0$ ($\zeta = 0$) to $r = r_1$ ($\zeta = \zeta_r$), and the η axis represents the distance from the center of the slot in the width direction. Then, the infinitesimal area normal to the molar flux can be represented as $A'_\zeta = [\zeta_r + (\pi/2 - 1)\,\zeta]\,d\eta/\zeta_r$ by assuming the area change was linear, thereby $A'_{\zeta=0} = d\eta$ and $A'_{\zeta=\zeta_r} = \pi d\eta/2$. Parameter ζ_r can be represented as Eq. (2.45) assuming that the species through the point η on the line $z = 0$ is moving toward the point $(r_1 \cos(\pi\eta/2r_1), r_1 \sin(\pi\eta/2r_1))$ on

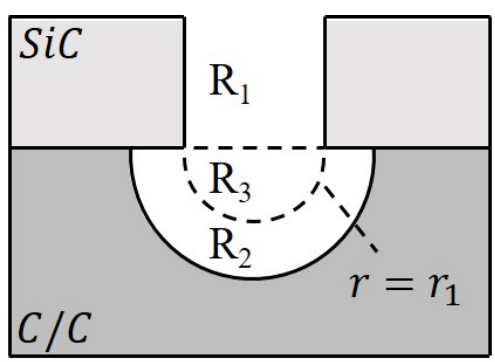

Figure 2.4: Illustration of the intermediate space.

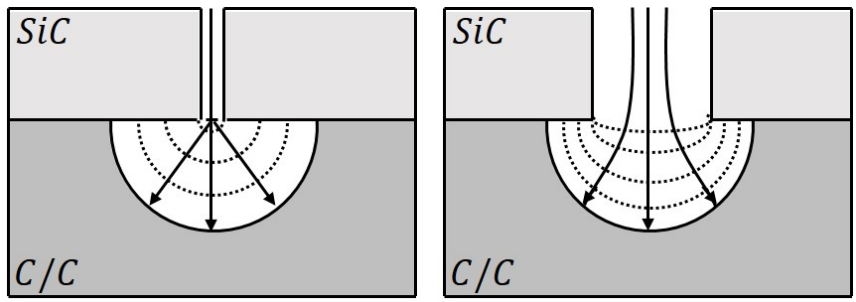

(a) (b)

Figure 2.5: (a) Illustration of radial molar flux when the crack width is small. (b) Illustration of non-radial molar flux when the slot is wide when compared with coating thickness.

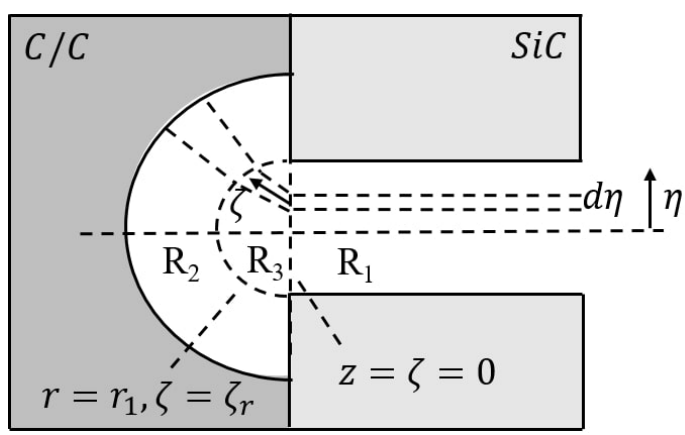

Figure 2.6: Coordinate descriptions for the diffusion model with quasi-1D intermediate region.

the line $r = r_1$.

$$\zeta_r(\eta) = r_1 \sqrt{\cos^2\left(\frac{\pi}{2}\frac{\eta}{r_1}\right) + \left(\sin\left(\frac{\pi}{2}\frac{\eta}{r_1}\right) - \eta\right)^2} \tag{2.45}$$

Let the R_3 region be denoted by symbol *. The gradient of the molar flux of CO_2 can be expressed by Eq. (2.46).

$$\frac{\partial}{\partial\zeta}\left(J^*_{CO_2} dA^*\right) = \frac{\partial}{\partial\zeta}\left(-cD^{\text{eff}}_{CO_2}\frac{d\eta}{\zeta_r}\frac{\left[\zeta_r + (\pi/2-1)\,\zeta\right]}{1+x_{CO_2}}\frac{\partial x_{CO_2}}{\partial\zeta}\right) = 0 \tag{2.46}$$

Together with boundary conditions $x_{CO_2} = x_{CO_2,\zeta_0}$ at $\zeta = 0$ and $x_{CO_2} = x_{CO_2,\zeta_r}$ at $\zeta = r_1$, the molar flux of CO_2 can be represented as Eq. (2.47).

$$J^*_{CO_2} = -cD^{\text{eff}}_{CO_2}\frac{\pi/2-1}{\ln(\pi/2)}\frac{\ln\left[\left(1+x_{CO_2,\zeta_r}\right)/\left(1+x_{CO_2,\zeta_0}\right)\right]}{\left[\zeta_r + (\pi/2-1)\,\zeta\right]} = 0 \tag{2.47}$$

Because $J^*_{CO_2} = -J^{II}_{CO_2}$ at $\zeta = 0$, combining Eqs.(2.47) and (2.20) gives Eq. (2.48a).

$$\ln\left(1+x_{CO_2,0}\right) = \frac{\xi z_f \ln\left(1+x_{CO_2,r_1}\right) + \ln\left(1+x_{CO_2,z_f}\right)}{\xi z_f + 1} \tag{2.48a}$$

$$\xi = \frac{\pi/2-1}{\zeta_r \ln(\pi/2)} \tag{2.48b}$$

The product of the molar flux and area must be constant in the path, and Eq. (2.24) must also be satisfied. Owing to the presence of region R_3, Eq. (2.24) can be represented as Eq. (2.49) instead of Eq. (2.25).

$$\ln\left(1+x_{CO_2,r_1}\right) = \frac{\xi \ln(r_2/r_1)\ln\left(1+x_{CO_2,z_f}\right)}{\xi\ln(r_2/r_1) + (\xi z_f + 1)\,\pi/w} \tag{2.49}$$

Eq. (2.50) can be obtained by combining Eqs. (2.48a) and (2.49).

$$\ln\left(\frac{1+x_{CO_2,z_f}}{1+x_{CO_2,0}}\right) = \frac{\pi z_f}{w}\frac{\xi\ln\left(1+x_{CO_2,z_f}\right)}{\xi\ln(r_2/r_1) + (\xi z_f+1)\,\pi/w} \tag{2.50}$$

Subsequently, Eq. (2.50) can be inserted into Eq. (2.21) to eliminate $x_{CO_2,0}$.

$$\frac{\pi}{w}\left(z_f+\frac{1}{\xi}\right)=\frac{-\ln\left(r_2/r_1\right)+\alpha\left(\beta+\beta^*\right)}{1+\alpha} \tag{2.51a}$$

$$\beta^*=\frac{\pi}{w\xi}=\frac{\pi}{w}\frac{\ln\left(\pi/2\right)}{\pi/2-1}\zeta_r \tag{2.51b}$$

By substituting x_{co_2,r_1} with Eq. (2.49), Eq. (2.23) leads to Eq. (2.52).

$$J_{CO_2}^{III}\times r\left[\frac{\pi L}{w}+\ln\left(\frac{r_2}{r_1}\right)+\frac{\pi}{w}\frac{\ln\left(\pi/2\right)}{\pi/2-1}\zeta_r\right]=\frac{cD_{CO_2}^{\text{eff}}\ln\left(1+x_{CO_2,z_f}\right)}{\alpha/\left(1+\alpha\right)} \tag{2.52}$$

By calculating the average of ζ_r from $\eta=-r_1$ to $\eta=r_1$, $\bar{\zeta_r}\approx 0.32865w$ can be obtained. Finally, the final model of this study can be derived in the same manner as depicted in previous sections.

$$t=\frac{\rho}{2M_C cD_{CO_2}^{\text{eff}}\ln\left(1+x_{CO_2,z_f}\right)}\left[r_2^2\ln\frac{r_2}{r_1}+\left(r_2^2-r_1^2\right)\left(\beta+\bar{\beta}^*-\frac{1}{2}\right)\right]\frac{\alpha}{\alpha+1} \tag{2.53}$$

2.5 Application of model to natural craze cracks

The values of the variables in Table 2.2 are required to apply the developed model to actual cracks. Given the specific flow conditions, the thickness of the coating, the width and length of the crack, and the density of the carbon matrix are required concerning the crack shape. The coating thickness and the density of the carbon substrate can be measured. The problem is measuring the width and length distribution of naturally occurring cracks. The crack length is different for all cracks, and many cracks have various widths. However, it is not evenly distributed over a wide range, and many cracks with widths around a specific value are observed so that the most frequent value can be used as the crack width [30]. The crack length is measured by measuring the total crack length in a specific area of the specimen to measure the crack length per unit surface area. At this time, a clear crack skeleton image can be obtained by slightly grinding the crack coating surface [29].

When a natural crack exists, the entire surface is divided into a coating surface and a surface opened by cracks in the surface view. When the oxidation weight change per unit surface area is measured, the oxidation amount for the area opened

Table 2.2: Inputs of model for oxidation through crack.

Crack geometry	coating thickness, crack width, crack length
Material property	C/C density
Flow condition	total pressure, partial pressures, temperature

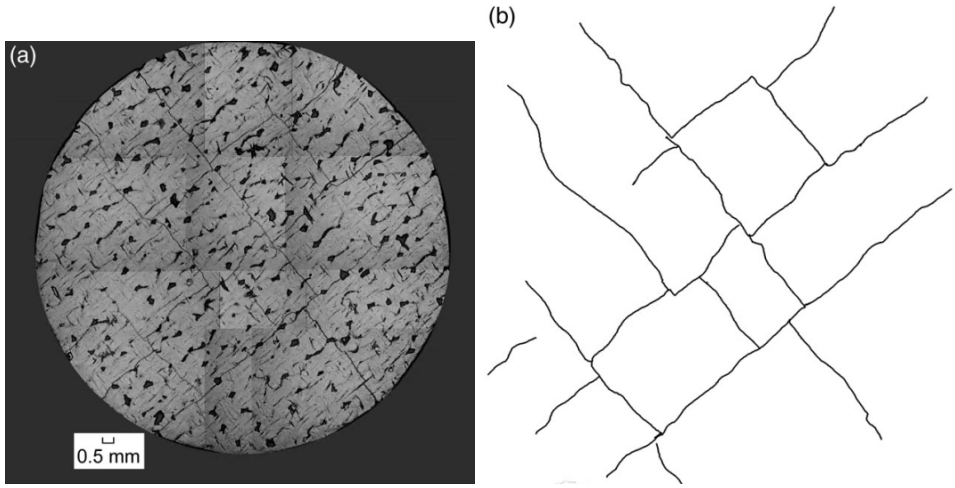

(a) Grinded surface with natural cracks. (b) Skeleton image of natural cracks.

Figure 2.7: Natural craze cracks: reprinted from [29].

by the crack can be converted through the following equation.

$$\left(\frac{\Delta W}{A_{surface}}\right) = \left(\frac{\Delta W}{A_{crack}}\right)\left(\frac{A_{crack}}{A_{surface}}\right) \tag{2.54}$$

$A_{surface}$ denotes the area of entire surface, and A_{crack} denotes the surface area opened by cracks. And since this equation corresponds to Eq. (2.33), it can be converted to the cavity size. In conclusion, the a of the cavity created under the interspersed cracks from the change in weight per unit area.

Chapter 3

Modeling for Oxidation Through Pores

3.1 Counter-current gaseous diffusion model

Many studies on the application of the counter-current gaseous diffusion model have been performed to describe the oxidation of the protective coatings [36, 37, 38, 52, 53, 54]. The schematic diagram of the counter-current diffusion process through the pores considered in the present study is illustrated in Fig. 3.1. The figure is representative of hafnium carbide/oxide, but it is equally applicable to Silicon carbide/oxide and zirconium carbide/oxide.

The path of diffusion consists of two zones because of the incompatibility between O_2 and CO gases as in the model of oxidation through cracks. In the zone near the carbide, gaseous species CO, CO_2, and N_2 exist. CO_2 diffused inward reacts with carbon, and the carbon substrate is oxidized by this reaction. Subsequently, the reaction releases CO, which moves outward. The reaction at the oxidation attack surface is as follow:

$$HfC(s) + 3CO_2(g) = HfO_2(s) + 4CO(g). \tag{3.1}$$

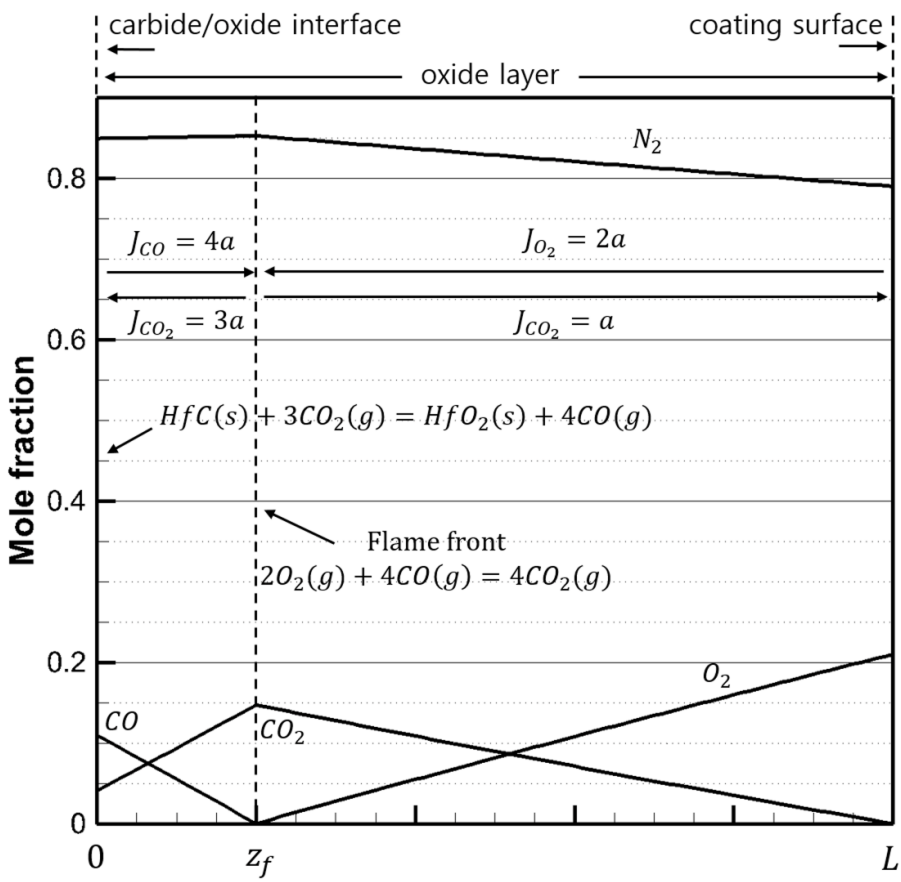

Figure 3.1: Schematic diagram of diffusion through porous oxide layer.

Gaseous species present in the outer region are O_2, CO_2, and N_2. Between these two regions, O_2 and CO react to form CO_2 at flame front.

$$2O_2(g) + 4CO(g) = 4CO_2(g) \tag{3.2}$$

Then the overall reaction is:

$$HfC(s) + O_2(g) = HfO_2(s) + CO_2(g). \tag{3.3}$$

Let region I denote the outer zone, region II be the inner zone, and $J^I_{O_2}$ be the molar flux (in moles/unit area-time) of O_2 in region I. Then $J^I_{CO_2}$ has opposite direction from $J^I_{O_2}$ and have the half magnitude. In region II, J^I_{CO} and $J^I_{CO_2}$ are in opposite direction. The reaction Eq. (3.1) and mass balance between CO and O_2 at the flame front are used to obtain the relation between molar fluxes in both regions:

$$\begin{aligned} J^{II}_{CO}/2 &= 4a, \\ J^{II}_{CO_2} &= -3a, \\ J^I_{CO_2} &= a, \\ J^I_{O_2} &= -2a. \end{aligned} \tag{3.4}$$

The molar flux of N_2 is zero along the path of diffusion. The species molar flux is constant along the path as presented in Eq. (2.5).

$$\frac{\partial J_i}{\partial z} = 0 \tag{3.5}$$

where z denotes the distance from the carbide-oxide interface to the coating surface inside the protective layer, as depicted in Fig. 3.1.

Diffusion equation

Unlike the diffusion model of oxygen through cracks, the simplified MS equation using effective diffusion coefficients (Eq. (3.6)) is adapted for the diffusion through

the pores because the model development from the Maxwell-Stefan equation is too complicated.

$$J_i = -cD_{i,eff}\left(\frac{\partial x_i}{\partial z}\right) + x_i \sum_j J_j \tag{3.6}$$

The most significant difference between the two equations is whether the mole fraction changes according to the position inside each region and whether the resulting diffusion coefficient can be used. In particular, since the distance at which molecules can freely move through the pores inside the oxide layer may be a short time longer than the mean free path, not only the gas phase inter-diffusion but also the Knudsen diffusion should be considered. This problem prevents the direct derivation of a model from the MS formula. Eq. (3.6) can be rewritten as Eq. 3.7.

$$-c\frac{\partial x_i}{\partial z} = \frac{J_i - x_i \sum_{j=1}^{N} J_j}{D_{i,eff}} = \frac{\sum_{j=1}^{N}\left(x_j J_i - x_i J_j\right)}{D_{i,eff}} \tag{3.7}$$

On the one hand, the effective diffusion coefficients should satisfy Eq. (3.8) in the porous media [55].

$$-c\frac{\partial x_i}{\partial z} = \frac{J_i}{D_{i,K}} + \sum_{j=1}^{N} \frac{x_j J_i - x_i J_j}{D_{i,j,M}} \tag{3.8}$$

In Eq. (3.8), $D_{i,K}$ is the Knudsen diffusion coefficient, and $D_{i,j,M}$ is the effective molecular diffusion coefficient. From Eq. 3.7 and Eq. 3.8,

$$D_{i,eff} = \frac{\sum_{j=1}^{N}\left(x_j J_i - x_i J_j\right)}{\dfrac{J_i}{D_{i,K}} + \sum_{j=1}^{N} \dfrac{x_j J_i - x_i J_j}{D_{i,j,M}}} \tag{3.9}$$

Although x_i varies through the diffusion path and the effective diffusion coefficient depends on species composition, the average values of each gas species in each region are used [47].

The Knudsen diffusion coefficient is defined as

$$D_{i,K} = \frac{4}{3} v_i K, \tag{3.10}$$

where v_i is the average molecular velocity of species i and K is the Knudsen permeability. The average molecular velocity and the Knudsen permeability are in Eq. (3.11) and (3.12).

$$v_i = \sqrt{\frac{8kT}{\pi M_i}} \tag{3.11}$$

$$K = r_p/2 \tag{3.12}$$

In Eq. (3.12), r_p is the radius of pore inside the porous oxide.

The effective molecular diffusion coefficient $D_{i,j,M}$ is obtained by correcting the gas phase inter-diffusion coefficient in consideration of the effect of diffusion being hindered by the oxide layer. Three components such as tortuosity (τ), restrictive factor ($\mathcal{F}$), and porosity (ϕ) are considered as Eq. (3.13).

$$D_{i,j,M} = \frac{D_{i,j}\phi}{\tau}\mathcal{F} \tag{3.13}$$

Tortuosity generally means the ratio of actual flow distance to straight distance. When tortuosity increases, the effective molecular diffusion decreases. Tortuosity is mostly expressed as a function of porosity. When the porosity is one, the tortuosity is one, and it increases as the porosity decreases. The forms of typical torsion functions are as follows [56, 57].

$$\begin{gathered} \tau = (y\phi^{1-p})^q \\ \tau = \phi + y(1-\phi) \\ \tau = 1 - yln\phi \end{gathered} \tag{3.14}$$

y, p, q are adjustable parameters. Some tortuosity functions are shown in Fig. 3.2. Since tortuosity function $\tau = phi^{-0.4}$ is used most often, this function was also

used in this study. However, since the functions are models suitable for 0.2 or more porosity, some functions increase rapidly as the porosity approaches zero. Therefore, in this study, a study on the tortuosity function was also conducted, which will be described later.

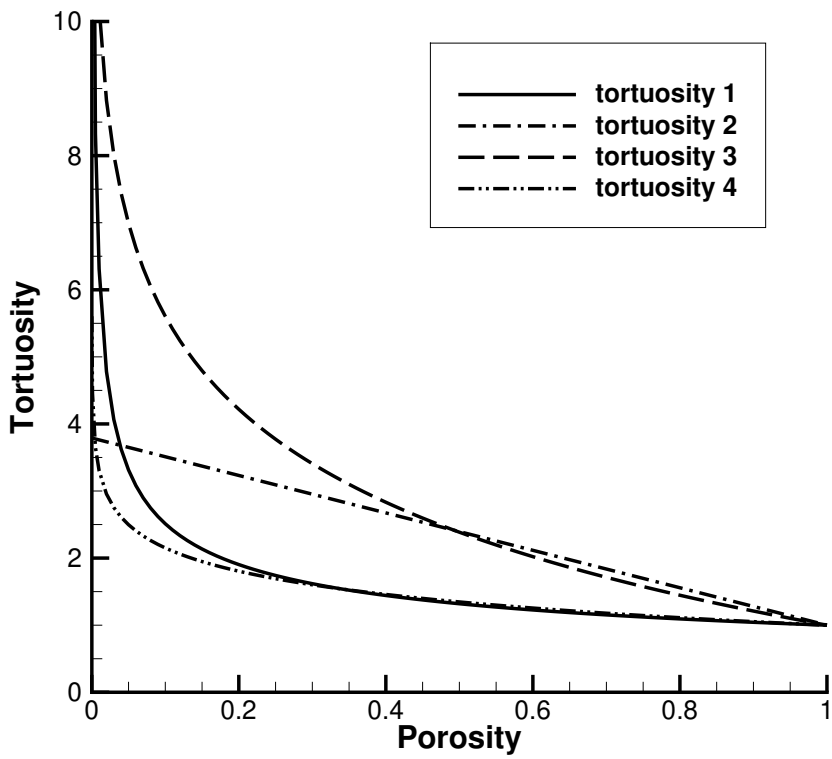

Figure 3.2: Various tortuosity models. tortuosity 1: $\tau = \phi^{-0.4}$, tortuosity 2: $\tau = \phi + 3.79(1-\phi)$, tortuosity 3: $\tau = 1 - 2ln\phi$, tortuosity 4: $\tau = 1 - 0.5ln\phi$

Restrictive factor $\mathcal{F}$ is adapted for the constrictivity, which is essential when the pore is exceptionally tiny, and the path is narrow, similar to the diameter of the diffusing molecule. It is expressed as a function of $lambda$, as shown in Eq. (3.15) [58].

$$\begin{aligned} \mathcal{F}(\lambda) &= (1-\lambda)^{3.5} \\ \lambda &= d_i/d_p \end{aligned} \tag{3.15}$$

d_i is the solute critical molecular diameter and d_p is the pore diameter. Because λ is the ratio between the diffusing particle diameter to the pore diameter, in this study, the kinetic diameter of each gas molecule is used for d_i. The kinetic diameter of each gas molecule is tabulated in Table 3.1 because they are frequently used for the diffusion of gas molecules [59]. The factor is almost one when the pore diameter is over 300 $\mathring{A}$ and rapidly decreases when the pore diameter is below 100 $\mathring{A}$. Restrictive factors for four gas species are shown in Fig. 3.3.

Table 3.1: Kinetic diameter of gas molecules.

Gas species	N2	O2	CO2	CO	O
Kinetic diameter (pm)	364	346	376	330	152[a]

[a]Diameter of atomic oxygen is from Van der Waals diameter.

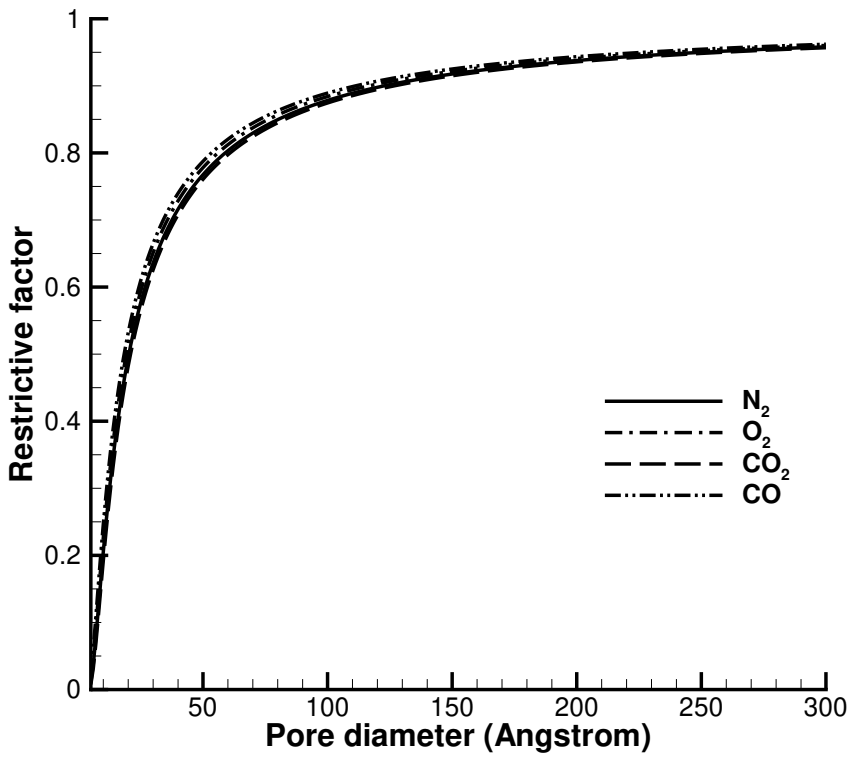

Figure 3.3: Restrictive factor.

3.2 Model without oxygen dissociation

Model development starts from Eq. (3.6). Molar concentration of each species c_i is used instead of the molar fraction x_i for convenience. Note that c is for total concentration, and c_i is the concentration of each species. Then Eq. (3.6) can be rewritten as Eq. (3.16).

$$J_i = -D_{i,eff}\left(\frac{\partial c_i}{\partial z}\right) + \frac{c_i}{c}\sum_j J_j \tag{3.16}$$

Then the equation can be transformed into an integrable form.

$$\frac{1}{c_i\sum_j J_j - cJ_i}dc_i = \frac{1}{cD_{i,eff}}dz \tag{3.17}$$

Integrating Eq. (3.17) with respect to the carbide-side zone, region II, gives the molar concentration according to the position as Eq. (3.18).

$$c_i = \left(c_{i,z_f} - \frac{cJ_i}{\sum_j J_j}\right)\exp\left[\frac{(z-z_f)\sum_j J_j}{cD^{II}_{i,eff}}\right] + \frac{cJ_i}{\sum_j J_j} \tag{3.18}$$

Recall that $J_{CO} = 4a$, $J_{CO_2} = -3a$, $\sum_j J_j = a$ in region II, then Eqs. (3.19)–(3.21) can be obtained.

$$c_{CO} = \left(c_{CO,z_f} - 4c\right)\exp\left[\frac{a(z-z_f)}{cD^{II}_{CO,eff}}\right] + 4c \tag{3.19}$$

$$c_{CO_2} = \left(c_{CO_2,z_f} + 3c\right)\exp\left[\frac{a(z-z_f)}{cD^{II}_{CO_2,eff}}\right] - 3c \tag{3.20}$$

$$c_{N2} = \left(c_{N_2,z_f}\right)\exp\left[\frac{a(z-z_f)}{cD^{II}_{N_2,eff}}\right] \tag{3.21}$$

Integrating Eq. (3.17) with respect to the surface-side zone, region I, gives the molar concentration according to the position as Eq. (3.22).

$$c_i = \left(c_{i,L} - \frac{cJ_i}{\sum_j J_j} \right) \exp \left[\frac{(z-L)\sum_j J_j}{cD^I_{i,eff}} \right] + \frac{cJ_i}{\sum_j J_j} \tag{3.22}$$

Recall that $J_{O_2} = -2a$, $J_{CO_2} = a$, $\sum_j J_j = -a$ in region II, then Eqs. (3.24)–(3.25) can be obtained.

$$c_{O_2} = (c_{O_2,L} - 2c) \exp \left[\frac{a(L-z)}{cD^I_{O_2,eff}} \right] + 2c \tag{3.23}$$

$$c_{CO_2} = (c_{CO_2,L} + c) \exp \left[\frac{a(L-z)}{cD^I_{CO_2,eff}} \right] - c \tag{3.24}$$

$$c_{N_2} = (c_{O_2,L}) \exp \left[\frac{a(L-z)}{cD^I_{N_2,eff}} \right] \tag{3.25}$$

Eq. (3.19) becomes because CO is all consumed at the flame front ($c_{CO,z_f} = 0$).

$$c_{CO,0} = (-4c) \exp \left[\frac{-az_f}{cD^{II}_{CO,eff}} \right] + 4c. \tag{3.26}$$

Similarly, Eq. (3.23) can be rearranged as Eq. (3.27) because O_2 is all consumed at the flame front ($c_{O_2,z_f} = 0$).

$$\ln \left(\frac{2c}{2c - c_{O_2,0}} \right) = \frac{a(L-z_f)}{cD^I_{O_2,eff}} \tag{3.27}$$

The relation between the molar flux and the position of flame front can be obtained from Eq. (3.27).

$$az_f = aL - cD^I_{O_2,eff} \ln \left(\frac{2c}{2c - c_{O_2,0}} \right) \tag{3.28}$$

Substituting Eq. (3.28) into Eq. (3.26) leads to Eq. (3.29).

$$c_{CO,0} = (-4c)\exp\left[-\frac{aL}{cD^{II}_{CO,eff}} + \frac{D^{I}_{O_2,eff}}{D^{II}_{CO,eff}}\ln\left(\frac{2c}{2c - c_{O_2,0}}\right)\right] + 4c \tag{3.29}$$

The molar concentration of CO_2, $c_{CO_2,0}$, can be written as Eq. (3.30) from Eq. (3.20).

$$c_{CO_2,0} = \left(c_{CO_2,z_f} + 3c\right)\exp\left[\frac{-az_f}{cD^{II}_{CO_2,eff}}\right] - 3c \tag{3.30}$$

Two unknown variables c_{CO_2,z_f} and z_f exist in Eq. (3.20). z_f can be eliminated by adapting Eq. (3.28). c_{CO_2,z_f} can be obtained from Eq. (3.24).

$$c_{CO_2,z_f} = (c_{CO_2,L} + c)\exp\left[\frac{a(L - z_f)}{cD^{I}_{CO_2,eff}}\right] - c \tag{3.31}$$

z_f in Eq. (3.31) also can be eliminated by adapting Eq. (3.28). Combining Eqs. (3.28), (3.30) and (3.31) leads to $c_{CO_2,0}$ with unknown aL only.

$$\begin{aligned} c_{CO_2,0} = &\left[(c_{CO_2,L} + c)\exp\left[\frac{D^{I}_{O_2,eff}}{D^{I}_{CO_2,eff}}\ln\left(\frac{2c}{2c - c_{O_2,0}}\right)\right] + 2c\right] \\ &\times \exp\left[-\frac{aL}{cD^{II}_{CO_2,eff}} + \frac{D^{I}_{O_2,eff}}{D^{II}_{CO_2,eff}}\ln\left(\frac{2c}{2c - c_{O_2,0}}\right)\right] - 3c \end{aligned} \tag{3.32}$$

Eq. (3.29) and (3.32) can be used to calculated aL. Assuming that CO and CO_2 are in an equilibrium state at the carbide-oxide interface, the equilibrium equation is used to calculate the molar concentration of CO and CO_2. When Eqs. (3.29) and (3.32) are substituted into Eq. (3.33), the only unknown variable aL can be obtained.

$$\frac{c^4_{CO,0}}{c^3_{CO_2,0}} = K_{eq} \tag{3.33}$$

Because of the molar volume difference between carbide and oxide, coating thickness may increase as the oxide layer grow, as depicted in Fig. 3.4. The relation between the recession rate and the molar flux is as follows.

$$\frac{dL_{XO_2}}{dt} = \mathcal{V}_{XO_2} a \tag{3.34}$$

$$\frac{dL_{XC}}{dt} = -\mathcal{V}_{XC} a \tag{3.35}$$

$$\frac{dL_{coating}}{dt} = (\mathcal{V}_{XO_2} - \mathcal{V}_{XC}) a \tag{3.36}$$

$\mathcal{V}$ is the molar volume of porous scale in $cm^3/mole$, which can be obtained by dividing the molecular weight by the density.

$$\mathcal{V}_{XO_2} = M_{XO_2}/\rho_{XO_2} \tag{3.37}$$

Assuming that the permeability aL is constant, the parabolic oxidation rate of the oxide thickness, k_p° in cm^2/s, can be defined as follow. Variables without subscript for either oxide or carbide denote variables for oxide below.

$$k_p^\circ = 2\mathcal{V}(aL) = 2L\frac{dL}{dt} \tag{3.38}$$

Then thickness change can be calculated by Eq. (3.39).

$$\Delta L = \frac{k_p^\circ}{2L}\Delta t \tag{3.39}$$

$$\Delta L_{XC} = -\frac{\mathcal{V}_{XC}}{\mathcal{V}_{XO_2}}\Delta L \tag{3.40}$$

$$\Delta L_{coating} = \left(1 - \frac{\mathcal{V}_{XC}}{\mathcal{V}_{XO_2}}\right)\Delta L \tag{3.41}$$

Eq. (3.42) is used at the first time step to avoid the infinite problem when L is zero.

$$\Delta L = \sqrt{k_p^{\circ} \Delta t} \tag{3.42}$$

The parabolic oxidation rate of the weight change, k_p in $g^2/(cm^4 - s)$, can be obtained from Eq. (3.43).

$$k_p = \left(\frac{M_{XO_2} - M_{XC}}{\mathcal{V}} \right)^2 k_p^{\circ} \tag{3.43}$$

Similarly, the oxide thickness change can be converted into the weight change of the protective layer.

$$\Delta W = \left(\frac{M_{XO_2} - M_{XC}}{\mathcal{V}} \right) \Delta L \tag{3.44}$$

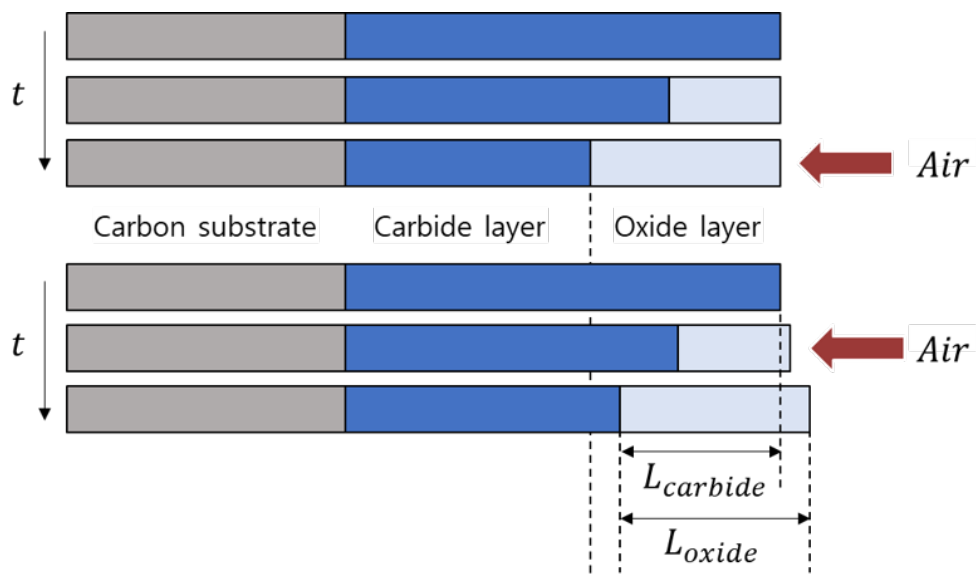

Figure 3.4: Thickness of carbide and oxide layers.

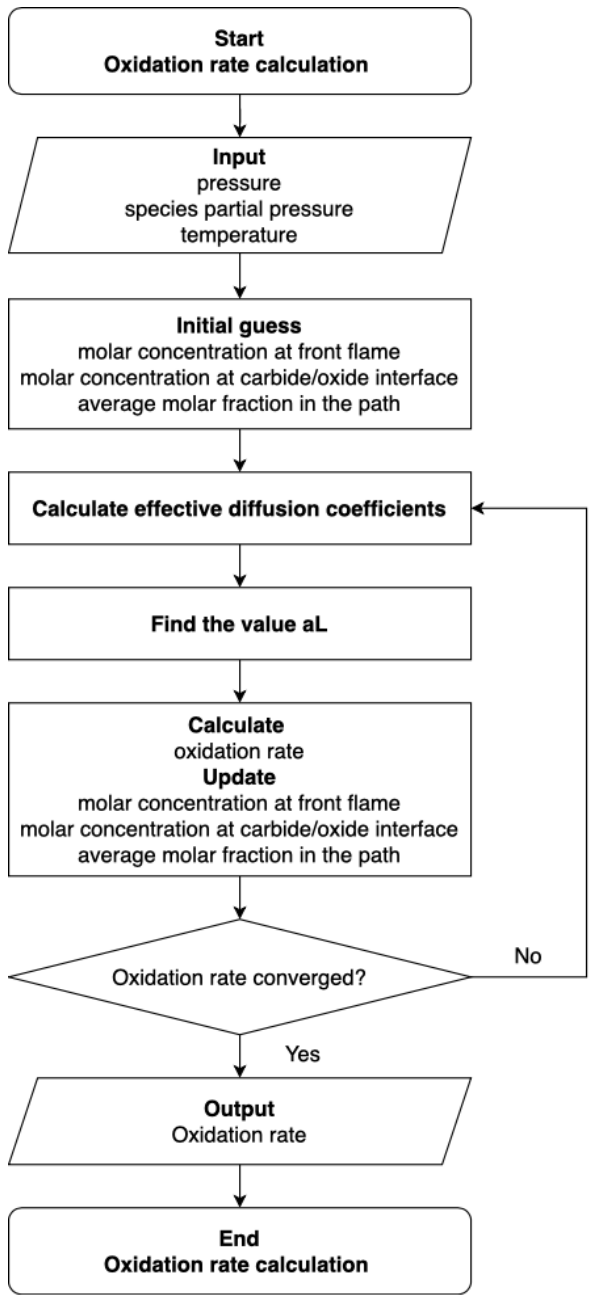

Figure 3.5: Flow chart of calculating oxide growth rate.

3.3 Model with oxygen dissociation

In the hypersonic flight condition, the molecules after shock can be dissociated, and O, N atoms, and NO molecules are expected to exist. The amount of N and NO at the surface of the protective layer may be negligible, but the dissociation of O2 into O can be significant. So a model considering the O molecule in the surface-side region is developed in this section.

The diffusion path consists of two zones because of the incompatibility between O and CO gases, as in the model of oxidation through cracks. In the zone near the carbide, gaseous species CO, CO_2, and N_2 exist. CO_2 diffused inward reacts with carbon, and this reaction oxidizes the carbon substrate. Subsequently, the reaction releases CO, which moves outward. The reaction at the oxidation attack surface is as follow:

$$HfC(s) + 3CO_2(g) = HfO_2(s) + 4CO(g). \tag{3.45}$$

Gaseous species in the outer region are O_2, CO_2, and N_2. Between these two regions,

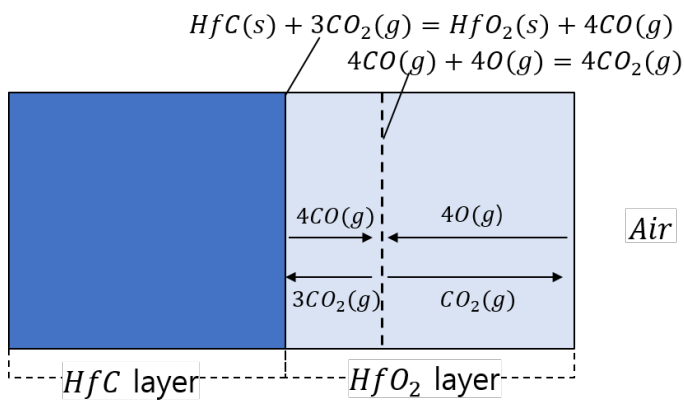

Figure 3.6: Schematic diagram of diffusion through porous oxide layer when O_2 is dissociated.

O and CO react to form CO_2 at the flame front.

$$4O(g) + 4CO(g) = 4CO_2(g) \tag{3.46}$$

Then the overall reaction is:

$$HfC(s) + 2O(g) = HfO_2(s) + CO_2(g). \tag{3.47}$$

The reaction Eq. (3.45) and mass balance between CO and O_2 at the flame front are used to obtain the relation between molar fluxes in both regions:

$$\begin{aligned} J^{II}_{CO}/2 &= 4a, \\ J^{II}_{CO_2} &= -3a, \\ J^{I}_{CO_2} &= a, \\ J^{I}_{O} &= -4a. \end{aligned} \tag{3.48}$$

In the same manner with sec. 3.2, Eq. (3.49) and (3.50) can be obtained.

$$\begin{aligned} c_{CO_2,0} = &\left[\left(c_{CO_2,L} + \frac{c}{3} \right) \exp \left[\frac{D^I_{O_2,eff}}{D^I_{CO_2,eff}} \ln \left(\frac{4c}{4c - 3c_{O_2,0}} \right) \right] + \frac{8}{3}c \right] \\ &\times \exp \left[-\frac{aL}{cD^{II}_{CO_2,eff}} + \frac{3D^I_{O_2,eff}}{D^{II}_{CO_2,eff}} \ln \left(\frac{4c}{4c - 3c_{O_2,0}} \right) \right] - 3c \end{aligned} \tag{3.49}$$

$$c_{CO,0} = (-4c) \exp \left[-\frac{aL}{cD^{II}_{CO,eff}} + \frac{D^I_{O_2,eff}}{D^{II}_{CO,eff}} \ln \left(\frac{4c}{4c - 3c_{O_2,0}} \right) \right] + 4c \tag{3.50}$$

aL can be obtained by combining Eqs. (3.33), (3.29), and (3.32). The oxidation rate can be calculated.

3.4 Measurement of input variables

The values of the variables in Table 3.2 are required to apply the developed model to predict the oxide growth speed. Assuming that flow conditions are given and oxide thickness is estimated at the previous time step during calculation, inputs according to porous media and oxide density is in need. Oxide density can be easily measured. Porosity can be measured using various techniques: direct method, optical method, computed tomography (CT) method, and gas expansion method. The direct method determines porosity with the bulk volume and the skeleton volume. The optical method estimates the porosity value by visually checking the cross-section. CT method uses CT scanning to render the internal geometry and then calculate porosity utilizing a program. The gas expansion method proceeds as follows. After filling a container with a sample and gas, the gas is transferred to another container of the same volume. Then the porosity can be calculated from the pressure difference between the two containers. The gas expansion method is the most recommended because it excludes isolated pores and can measure relatively accurately only the porosity by open pores that can reach the gas penetrating through the surface. Pore radius can be measured by gas adsorption experiment [60]. Gas adsorption experiments measure the surface area, pore radius, and volume of those pores open to the surface. This method is suitable for pore radius range from 0.35 nm to 100 nm. A

Table 3.2: Inputs of model for oxidation through pores.

Porous media	porosity, pore radius, tortuosity, oxide thickness
Material property	oxide density
Flow condition	total pressure, partial pressures, temperature

sample is typically held at the boiling temperature of the gas such as N_2 and Ar, and the difference in volume in the equilibrium state is measured for a range of pressure. Then the data is converted into the pore size distribution using various theories such as the Brunauer–Emmett–Teller (BET) method. The diffusion method is a direct method for measuring tortuosity because the tortuosity is the ratio of the average pore length for the major flow or diffusion pathway to the length of the porous medium along flow or diffusion axis [61, 62].

Chapter 4

Result of Modeling Oxidation Through Cracks

4.1 Previously published experimental cases

Measurements for carbon oxidation through artificial wide slots and natural craze cracks have been reported by Jacobson et al. [29]. The temperature range of this experiment targets the thermal environment around the re-entering Space Shuttle. Most of the Space Shuttle surface did not get hotter than 1,260 °C [63], and this test was conducted up to 1,300 °C. In wide slot cases, slots were artificially made on the SiC coated on reinforced carbon/carbon (RCC) disk with a diameter of 1.91 cm. The coating thickness was 0.78 ± 0.14 mm, the width of the slot was between 0.312 and 1.116 mm, and the length of the slot was approximately 7–8 mm. These slotted specimens are shown in Fig. 4.1. The density of carbon was assumed to be 1.362 g/cm^3. The specimens with an artificial slot were oxidized in a box furnace. Bottled air at 1 atm was used, and the tests were performed at 1,200 °C for 2.5 h. The weight difference was measured at every 0.5 h. The test conditions and measured weight loss rates for six artificial slot cases are tabulated in Table 4.1. The oxidation attack through

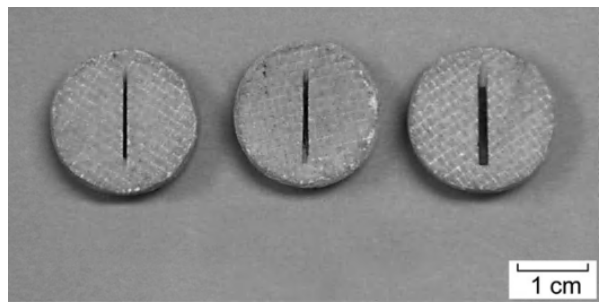

Figure 4.1: RCC disks with artificial slots: reprinted from [29].

Table 4.1: Case conditions and weight loss rates of SiC-coated RCC specimens with machined slots at 1,200 °C in air [29].

Case number	Slot width (mm)	Slot length (mm)	Weight loss rate (mm/mm^2-h)
case 1	0.484 ± 0.062	8.177 ± 0.923	34 ± 6
case 2	0.312 ± 0.033	8.284 ± 0.63	48 ± 6
case 3	0.560 ± 0.013	7.094 ± 0.132	48 ± 1
case 4	0.466 ± 0.04	7.114 ± 0.019	43 ± 5
case 5	1.116 ± 0.024	7.602 ± 0.101	18 ± 1
case 6	0.963 ± 0.0041	7.624 ± 0.039	21 ± 1

cracks naturally formed on the SiC coating was investigated in craze crack cases. The thickness and width of the crack were approximately 1.6 mm and 12.8 μm, respectively. Crack widths were measured near the surface. The crack length per unit area was determined using the surface image of 0.3 mm-grinded coating. The total crack length was obtained by multiplying the geometrical surface area by the crack length per unit area. The specimens with natural cracks were oxidized in a vertical tube furnace. Bottled air at 1 atm was used, and the tests were performed at 1,000, 1,100,

1,200, and 1,300 °C for 2–2.5 h. The specimens were suspended from a recording electro-balance by a sapphire fiber with a platinum wire basket into the vertical tube furnace. The results are provided in the form of a weight change plot in Fig. 4.4–4.7. The weight loss appears negative at the beginning of the experimental period at higher temperatures owing to the passive oxidation of the SiC coating. The weight change plot can be fitted using the combined SiC passive oxidation/carbon oxidation law [29], Eq. (4.1), and the carbon consumption rate can be derived.

$$\left(\frac{\Delta W}{A_{surface}}\right) = \sqrt{k_p t} - k_l t \left(\frac{A_{crack}}{A_{surface}}\right) \tag{4.1}$$

where ΔW is the weight change, $A_{surface}$ is the geometrical surface area of the test specimen, A_{crack} is the area of carbon exposed by craze cracks, k_p is the parabolic weight gain rate by SiC passive oxidation, and k_l is the linear weight loss rate by carbon oxidation. The parabolic and linear oxidation rates that best followed the experimental results were selected within reasonable ranges. Subsequently, the derived linear rate can be directly compared with the weight loss rate calculated from Eq. (2.33) because $k_l = \Delta W_c / A_{crack} t$. The test conditions and plot-fitted weight loss rates for four craze crack cases are tabulated in Table 4.2. The fitting curves using the selected rates are also presented in Fig. 4.4–4.7.

Table 4.2: Case conditions and fitted oxidation rates for SiC-coated RCC specimens with craze cracks.

Case number	Temperature (°C)	Geometrical surface area (mm^2)	Total crack length (mm)	linear rate (mg/mm^2h)	parabolic rate (mg/mm^2-h)
case 7	1,000	850.2±10	281±34	24.5±7	-
case 8	1,100	935.5±10	309±37	24.5±6	6.5×10^{-3}
case 9	1,200	946.8±10	312±37	33±8	3.3×10^{-2}
case 10	1,300	940.2±10	310±37	27±9	2.8×10^{-2}

Conditions are from Jacobson et al. [29] and rates are fitted in this study.

4.2 Validation of model

The results from the present model, earlier model, and experiments are plotted in Fig. 4.2, and the results for the craze crack cases are shown separately in Fig. 4.3. For results from an earlier model, values published in a previously presented paper [29] were used.

The results from the present model validate the effectiveness of the model. In cases 1–4, values smaller than the experimental results were still predicted; how-

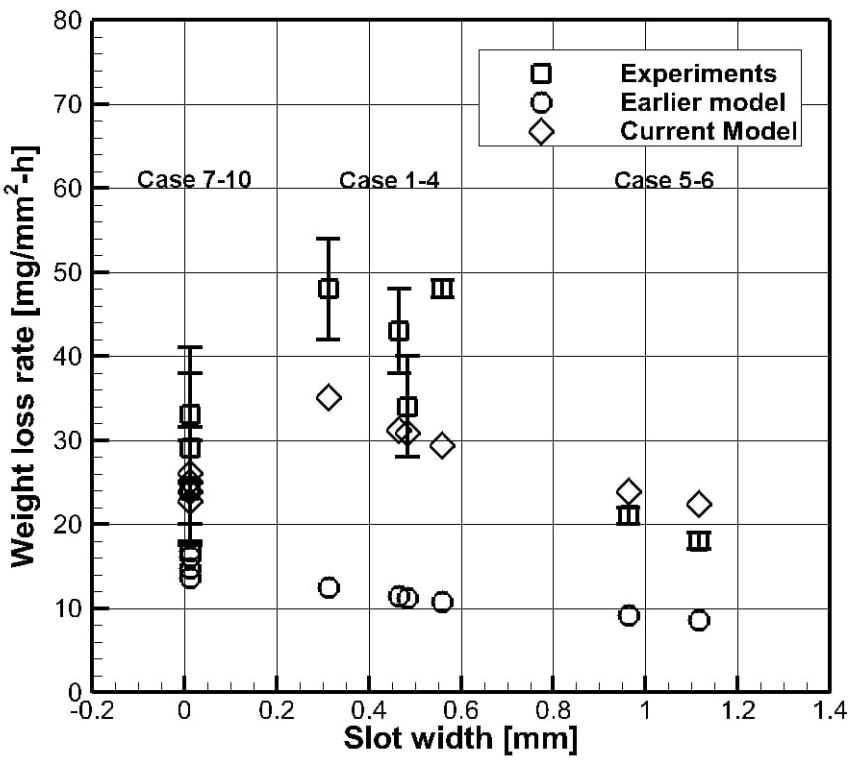

Figure 4.2: Validation of the model. Experimental data (squares), results of the earlier model (circles), and results of the current model (diamonds): cases 1–10.

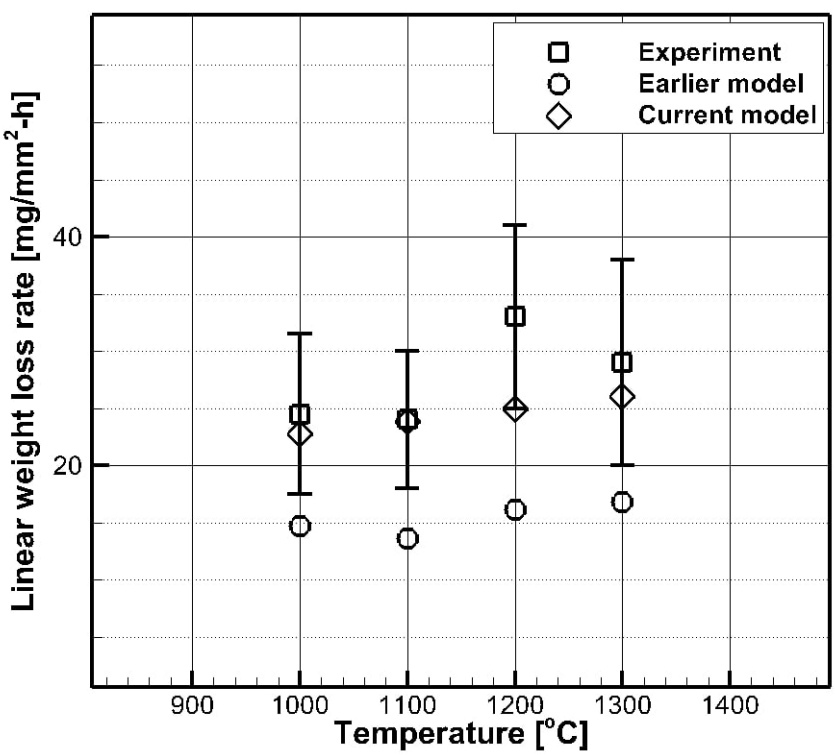

Figure 4.3: Validation of the model. Experimental data (squares), results of the earlier model (circles), and results of the current model (diamonds): cases 7–10.

ever, the values are closer to the experimental ones when compared with those of the previous model. Although there were some differences between the calculations and experimental results, those differences seem permissible because variations in results can occur because of factors not considered in the proposed model: additional oxidation through craze cracks, vaporization of impurities, and non-uniform thickness of the coating, and winding cracks [29]. In cases 5–6, in contrast to cases 1–4, the calculations exhibited results slightly larger than the values from the experiments; however, it can be said that the calculation predicted the oxidation rate well, even for oxidation through wide slots.

The predictions for cases 7–10 are in good agreement with the experimental values, though uncertainties such as non-uniform crack thickness and tortuosity in the crack path may exist. Weight change plots are compared in Fig. 4.4–4.7. Solid lines depict experimental results. Double-dotted lines are curves with the fitted rates listed in Table 4.2. Dotted lines are curves with the rates obtained from an earlier model, and dashed lines are curves with the rates obtained from the current model. Except for the case of 1,200 °C, the results obtained from the present model are in good agreement with experimental curves. In summary, the proposed model predicted the oxidation attack through the narrow crack and wide slot more efficiently when compared with the experimental results. Thus the model developed is validated on an oxidation rate model under 1,000 °C and 1,400 °C, where the diffusion-controlled model can appropriately estimate oxidation.

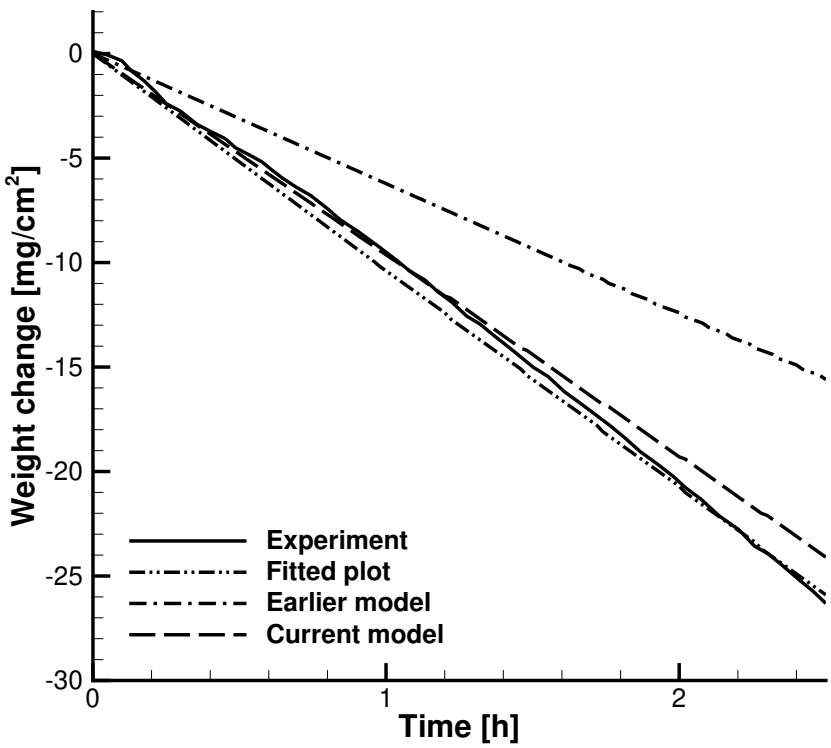

Figure 4.4: Weight change plots for case 7.

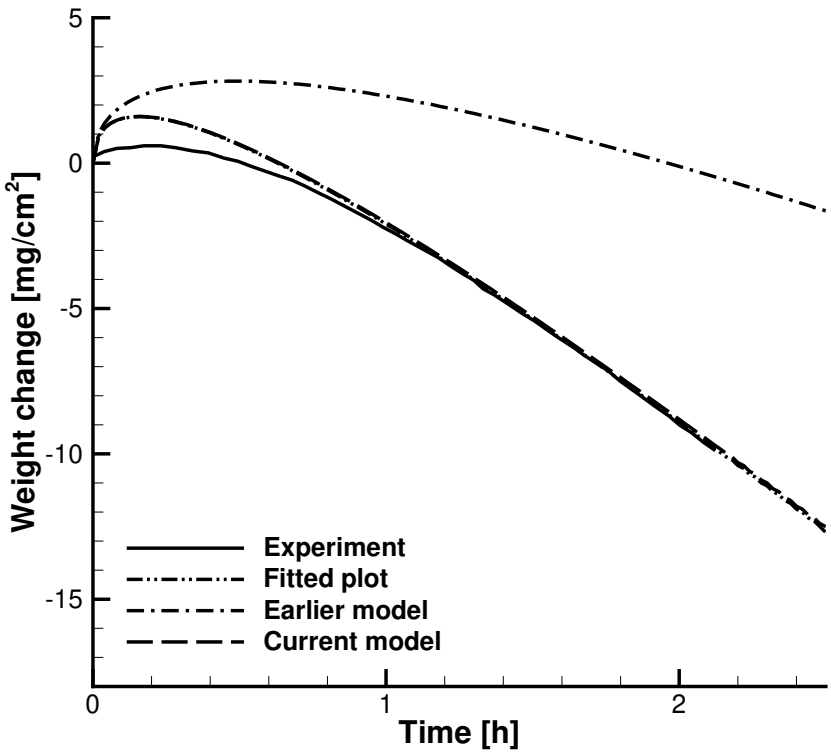

Figure 4.5: Weight change plots for case 8.

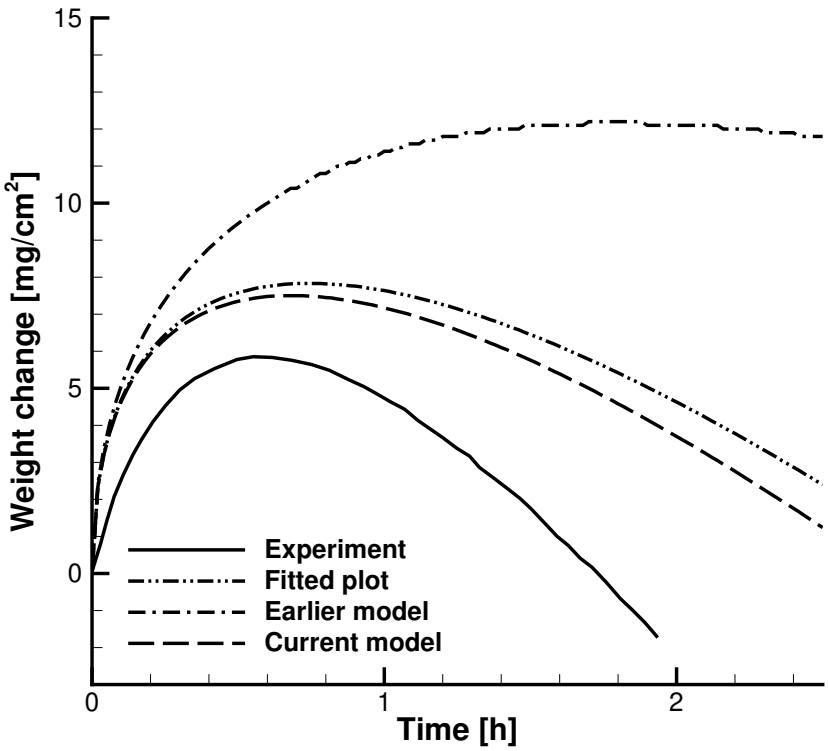

Figure 4.6: Weight change plots for case 9.

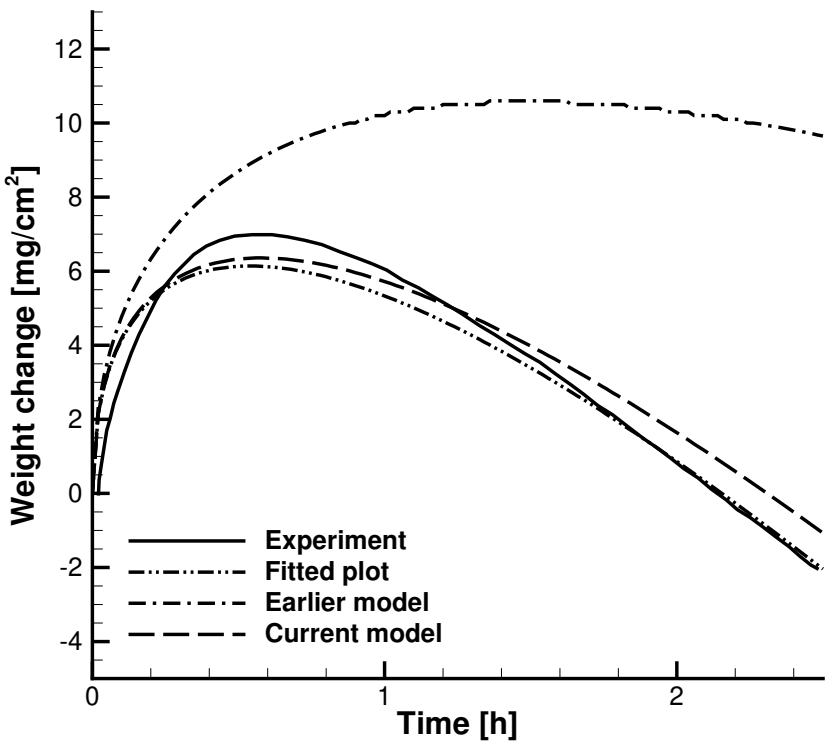

Figure 4.7: Weight change plots for case 10.

4.3 Discussions

4.3.1 Impact of assumptions on calculation

Four models listed in Table 4.3 were compared to investigate the impact of each assumption on the estimation of carbon consumption by oxidation attack. The models were developed based on assumptions listed in Table 4.3. The models' details were omitted for this paper's clarity and conciseness. The fixed-binary model was developed from the simplified MS equation, and the position of the flame front was fixed at the initial location, whereas the void was growing. The fixed-ternary model was developed from the original MS equation; however, the position of the flame front was fixed. The moving-ternary model is given by Eq. (2.32), and the current model is given by Eq. (2.53). The results from the models are presented in Fig. 4.8 and Fig. 4.9. The fixed-binary and fixed-ternary models were compared to ascertain the need to use the original MS equation rather than the simplified equation. The fixed-ternary and moving-ternary models were compared to evaluate the impact of the released front flame on the calculation.

Table 4.3: Descriptions of models with various assumptions.

Model	Assumptions		
	Diffusion	Flame front	Intermediate path
fixed-binary model	binary	fixed	X
fixed-ternary model	ternary	fixed	X
moving-ternary model	ternary	released	X
current model	ternary	released	O

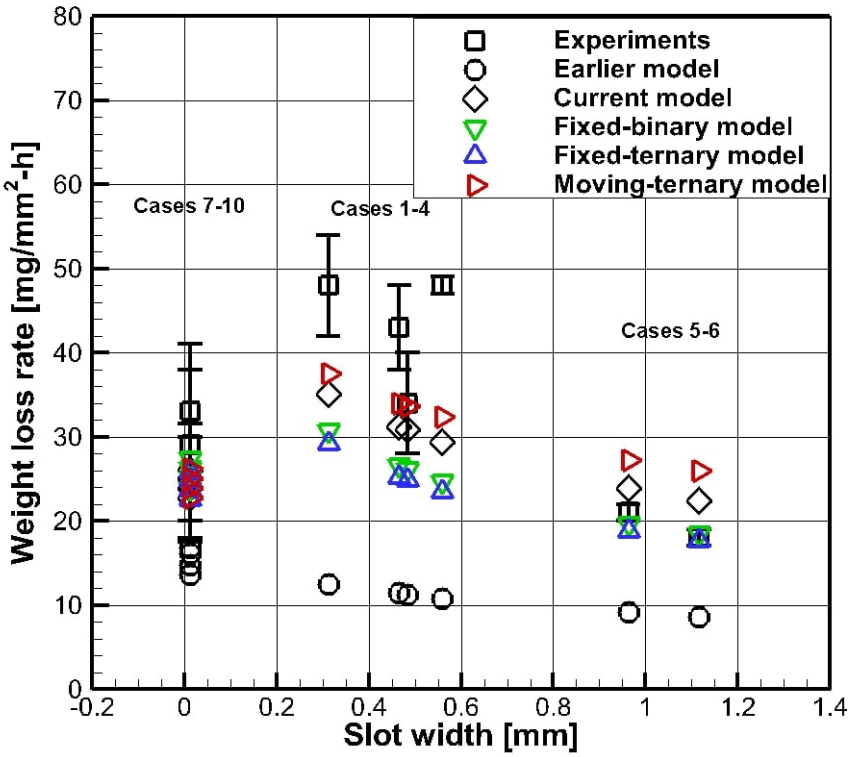

Figure 4.8: Weight loss rates calculated using various models: cases 1–10.

Furthermore, the moving-ternary and final models were compared to study the impact of the intermediate region. The assumptions for the earlier model in Fig. 4.8 and Fig. 4.9 were the same as for the fixed-binary model; however, some revisions were made to the fixed-binary model. Some errors in the formula derivation, such as using molar flux instead of mass flux and a fault in the equation rearrangement, were corrected, and the model was developed without approximations of the logarithmic terms using Taylor expansions.

Compared with the fixed-binary model, the fixed-ternary model exhibits 6–7 %

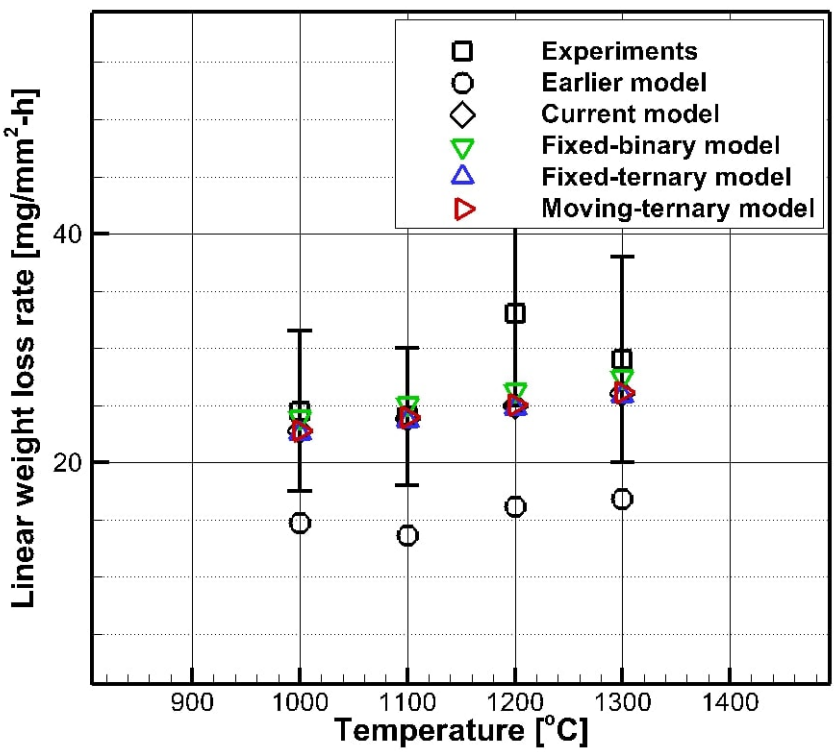

Figure 4.9: Weight loss rates calculated using various models: cases 7–10.

lower weight loss rates. This difference appears because the simplified MS equation ignores the impact of the N_2 gas in the outer region. With proper boundary conditions, combining Eqs. (2.4) and (2.7) leads to Eq. (4.2).

$$x_{CO_2,zf} = x_{O_2,L} D^{\text{eff}}_{O_2} / D^{\text{eff}}_{CO_2} \tag{4.2}$$

The ratio $D^{\text{eff}}_{O_2}/D^{\text{eff}}_{CO_2}$ is approximately 1.29 in the range of 1000–1300 °C. Because x_{CO_2,z_f} is greater than $x_{O_2,L}$, x_{N_2,z_f} must be smaller than $x_{N_2,L}$. However, Eq. (2.7) takes the form of Eq. (4.3) when referring to N_2, $x^I_{N_2}$ is constant regardless of its location.

$$J_{N_2} = -cD^{\text{eff}}_{N_2} \left(\partial x_{N_2}/\partial z\right) = 0 \tag{4.3}$$

Assuming that $x_{O_2,L}$ at the coating surface is 0.21, the sum of mole fractions at $z = z_f$ becomes 1.06, which means that the law of conservation of mass is not satisfied in the outer region (see Table 4.4). Furthermore, the x_{CO_2,z_f} value calculated using the binary equation is approximately 6.7 % larger than those obtained from the ternary equation (Table 2.1). This difference appears to result in a weight loss rate deviation of 6–7% because x_{CO_2,z_f} appears in the final model and directly affects the results.

Without ignoring the multi-component term, the MS equation can be reorganized into a form similar to the simplified equation [64]:

$$J_i = -cD^{\text{eff}}_i \left(\frac{\partial x_i}{\partial z}\right) + x_i D^{\text{eff}}_i \sum_j \frac{J_j}{D_{ij}}\,,\ D^{\text{eff}}_i = \sum_j \frac{x_j}{D_{ij}} \tag{4.4}$$

And in the previous model, a more simplified Equation, Eq. (2.7), was used. The effective diffusion coefficient D^{eff}_i has been approximated as the binary diffusion coefficient between species i and N_2, which is denoted as D_{i,N_2}. The final term is

Table 4.4: Weight loss rates at 1200 °C in air for SiC-coated RCC specimen with machined slots.

Temperature (°C)	$D_{O_2}^{\text{eff}}$	$D_{CO_2}^{\text{eff}}$	$D_{O_2}^{\text{eff}}/D_{CO_2}^{\text{eff}}$	$\sum x_{i,z_f}$
1000	2.389	1.854	1.289	1.060
1100	2.705	2.099	1.289	1.060
1200	3.038	2.351	1.292	1.061
1300	3.390	2.616	1.296	1.062

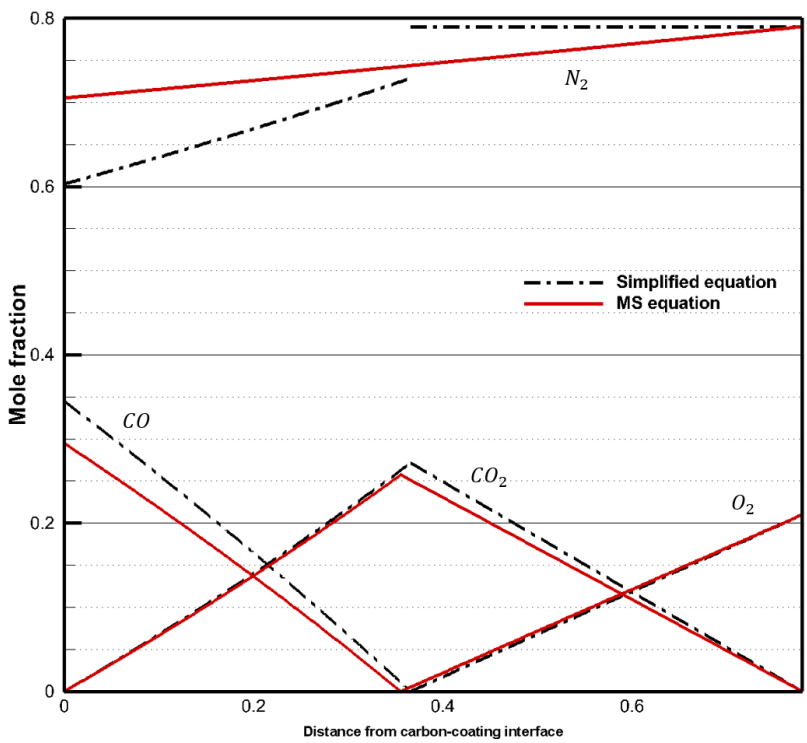

Figure 4.10: Mole fraction discontinuity at flame front.

nonzero for N_2, and the sum of mole fractions remains one when the term is considered. It can be inferred that the existing model predicted a smaller loss than the experimental result despite ignoring the impact of nitrogen and predicting a larger carbon consumption rate than that of the model with a multi-component effect. In conclusion, modeling based on the simplified MS equation is suitable for approximations; however, the multi-component MS equation is necessary for precise estimation and a detailed understanding of the oxidation mechanism.

Impact of moving flame front

The moving-ternary model exhibits weight loss rates 25–50 % larger in cases 1–6 than those predicted by the fixed-ternary model; there is little difference in cases 7–10. In the previous fixed model, $x_{CO_2,0}$ in Eq. (2.21) is assumed to be zero when calculating z_f and z_f is fixed at one position as Eq. (4.5), even though it has to be shifted inward as the void grew.

$$\frac{L}{z_f} = 1 + x_{O_2,L}\frac{D_{O_2,\text{eff}}}{D_{CO_2,\text{eff}}}\left[\ln\left(1 + \frac{D_{O_2,\text{eff}}x_{O_2}}{D_{CO_2,\text{eff}}}\right)\right]^{-1} \tag{4.5}$$

In that case, $z_f/L \approx 0.47$; however, the flame front moves inward as it is released in the current model, as depicted in Fig. 4.12.

When the width is narrow, as in the case of a 0.01 mm wide crack, owing to an insufficient supply of gas molecules, the molar flux per unit area in the cavity is extremely small, and the mole fraction gradient inside the void is minimal. Therefore, $x_{CO_2,0} \approx x_{CO_2,r_2}$ and the flame front exhibits almost no movement. In contrast, when the crack width is sufficiently wide, as in the case of a width of 1 mm, the amount of flux into the carbon surface increases, as depicted in Fig. 4.13, when the flame front is released, yielding a result that is up to 60% larger than that of the fixed model. Finally, the term z_f does not explicitly appear in the current model, unlike in previous models. The location of the flame front is no longer a significant factor in estimating carbon degradation in the current model; only the path geometry of cracks and cavities affects the calculation.

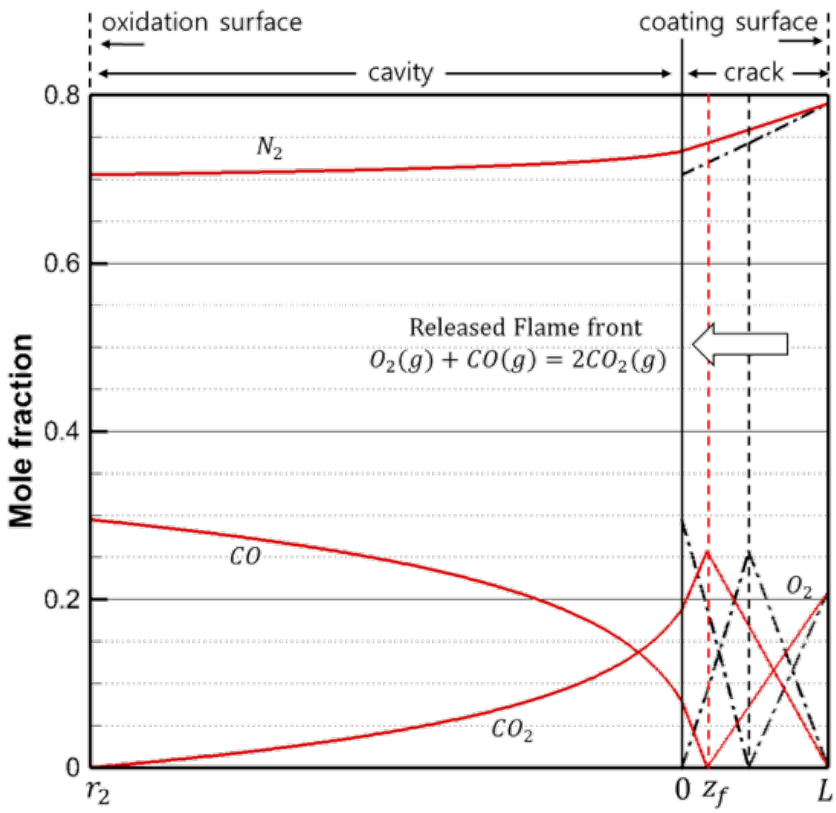

Figure 4.11: Released flame front.

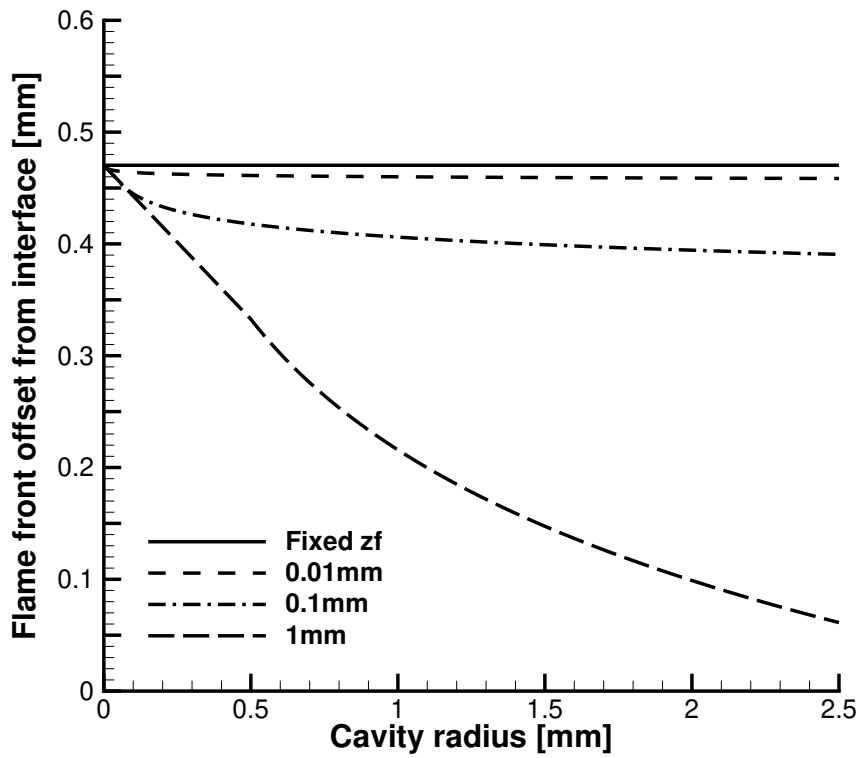

Figure 4.12: Location of flame front calculated using fixed-ternary and final models for 1 mm thick coating with 0.01 mm, 0.1 mm, and 1 mm wide cracks at 1200 °C in air at 1 atm.

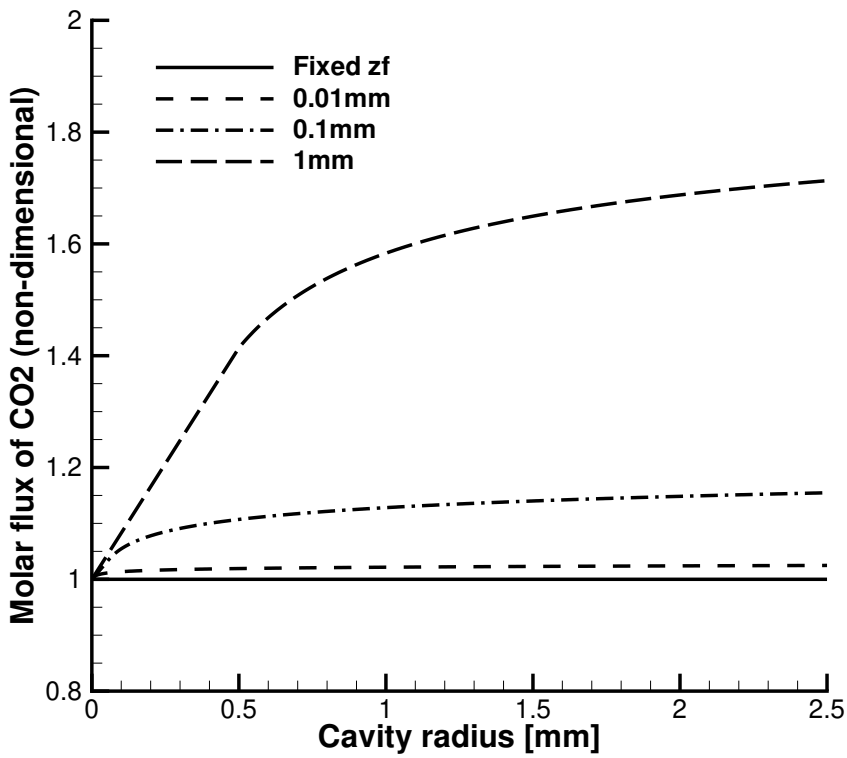

Figure 4.13: Molar flux of CO_2 calculated using fixed-ternary and final models for 1 mm thick coating with 0.01 mm, 0.1 mm, and 1 mm wide cracks at 1200 °C in air at 1 atm.

Effect of path geometry

The magnitudes of the flux and coating thickness are always observed together as a product, which has units of permeability, in equations [38]. Similarly, Eq. (2.53) can be expressed as Eq. (4.6).

$$J_{CO_2}^{III} \times r\left[R_1 + R_2 + R_3\right] = \frac{cD_{CO_2}^{\text{eff}} \ln\left(1 + x_{CO_2,z_f}\right)}{\alpha/\left(1+\alpha\right)} \tag{4.6}$$

Terms $\pi L/w$, $\ln\left(r_2/r_1\right)$, and $\dfrac{\pi}{w}\dfrac{\ln\left(\pi/2\right)}{\pi/2-1}\xi_r$ correspond to terms R_1, R_2, and R_3, respectively. The second term on the left-hand side is the diffusion path geometry, and the right-hand side corresponds to permeability. Therefore, J_{CO_2} is affected mainly by the diffusion path term because the right-hand side term is fixed when atmospheric conditions are given.

When R_3 was considered in the final model, the model predicted a weight loss rate lower than that predicted by the moving-ternary model. The difference between the two models became more prominent as the slot width increased. As depicted in Fig. 4.14, the ratio of R_3 for R_1 increases as the crack width increases, and the magnitude is in a similar order of R_2. Owing to the complexity in the derivation process, area A_ζ was assumed to be proportional to ζ in the quasi-1D region; however, in fact, it may be proportional to ζ^p, where p would be more significant than 1 (e.g., 1.5). Subsequently, the calculated results would increase as the slot width decreases and decrease as the slot width increases; therefore, the model results may show better agreement with the test results when compared with the current model. The results obtained using fixed models coincide with experimental results by chance because the impact of the moving flame front, which predicted larger values, and the impact of the region R_3, which predicted more minor values, canceled out. For craze crack

cases, the difference between the ternary models was minimal because the cavity size was significantly smaller than the coating thickness, and there was no impact on the cavity.

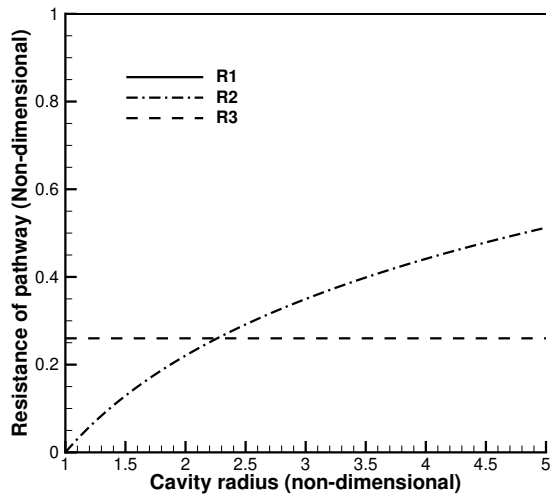

(a) Crack width of 1 mm.

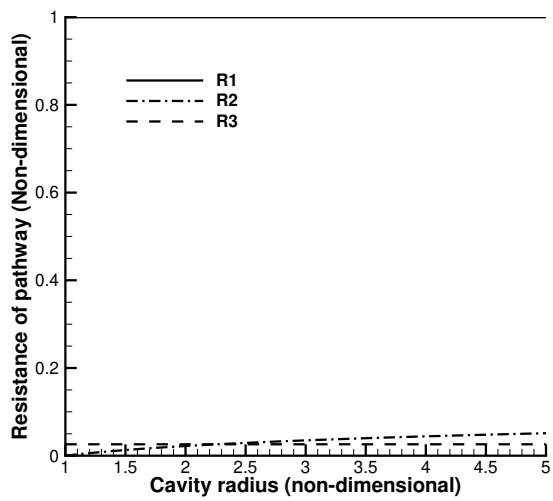

(b) Crack width of 0.1 mm.

Figure 4.14: Ratios of R_2 and R_3 of pathway resistance with respect to R_1 for 1 mm-thick coating.

4.3.2 Characteristics of weight loss by oxidation attack through cracks

As mentioned above, the degradation of carbon substrates through cracks is only controlled by the path's geometry and atmospheric conditions. The characteristics of the weight loss of carbon substrates caused by oxidation attack through coating cracks are investigated in this section based on crack geometry and atmospheric conditions.

Dependency on geometry of coating crack and void

The weight loss rates for specimens with various coating thicknesses and crack widths are depicted in Fig. 4.15. With reference to the case of the space shuttle [25, 17, 26], coating thicknesses and widths within 0.5–1.5 mm and 0–1.2 mm, respectively, were used. Figs. 4.15a and 4.15b depict the carbon consumption rate as $\Delta W_C/wlt$ and $\Delta W_C/lt$, respectively. The rate increases as the coating thickness decrease; it increases as the crack width increases. In contrast, the weight loss per crack width decreases as the crack widens. When the crack width is approximately 10 μm, the rate can be calculated using the current model, as shown in cases 7–10. In addition, because crack healing is not effective at temperatures under 1300 °C [65, 66], it is unnecessary to consider crack healing. However, when the crack width is of the order of 1 μm, the binary diffusion coefficients should be replaced with the effective diffusion coefficients, which are combinations of the molecular diffusion coefficients and Knudsen diffusion coefficients, to calculate diffusion in the crack path in which the mean free path of molecules is significantly greater than the crack width [38, 67, 29, 54]. In this condition, the weight loss rate would be decreased.

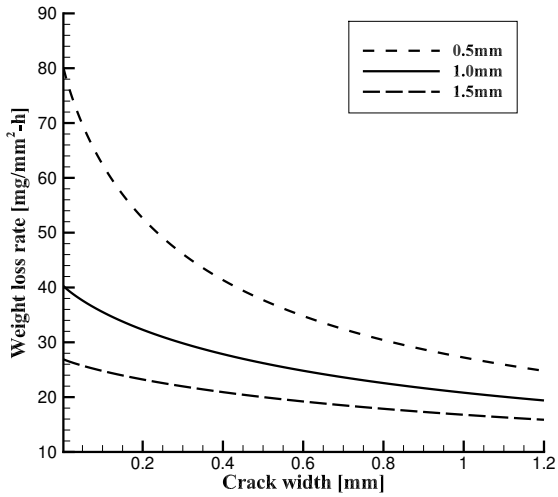

(a) Weight loss rate per unit area.

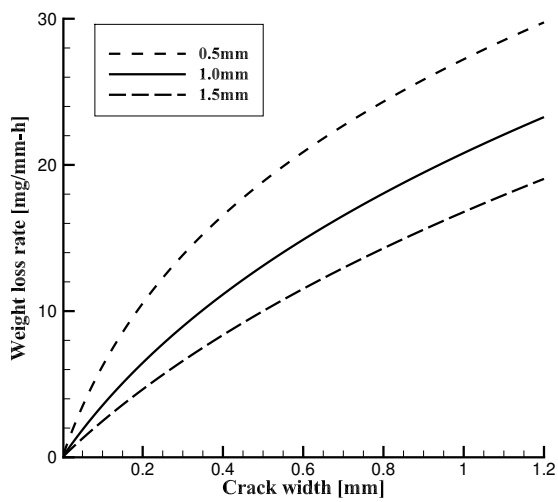

(b) Weight loss rate per unit length.

Figure 4.15: Weight loss rate in air of 1200 °C based on coating thickness and crack width.

Dependency on atmospheric conditions

Weight loss rates for various atmospheric conditions are depicted in Fig. 4.16. The speed of carbon degradation is proportional to $T^{0.6}$–$T^{0.7}$ in 1,000–2,500 °C range for 0.01–1 mm widths. Therefore, the rate at 2,500 °C is approximately 40% larger than that at 1,000 °C. The weight loss rate is almost proportional to the partial pressure of oxygen when the total pressure is constant because the partial pressure means the number of oxygen molecules. However, the oxidation speed is inversely proportional to the total pressure when the partial pressure of oxygen is constant. This trend happens because the number of other molecules in the path hindering oxygen diffusion increases as the total pressure increases.

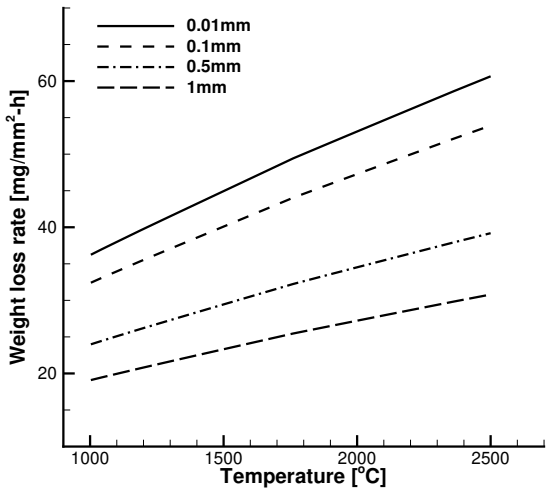

(a) Weight loss rate versus temperature for various crack widths.

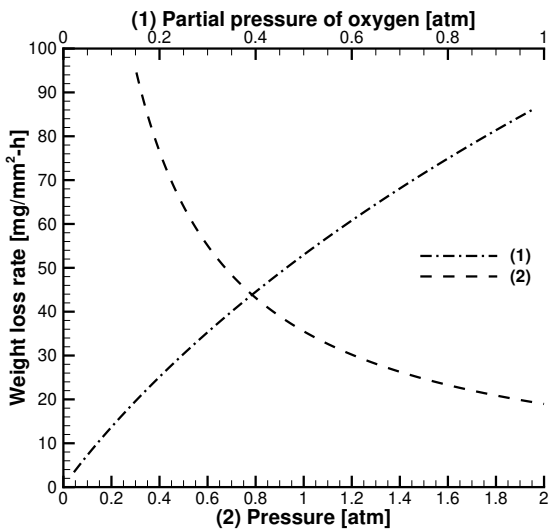

(b) Weight loss rate based on (1) partial pressure of oxygen and (2) atmospheric pressure of air (crack width 0.5 mm).

Figure 4.16: Weight loss rate under 1 mm-thick coating crack under various atmospheric conditions.

Chapter 5

Result of Modeling Oxidation Through Pores

5.1 Previously published experimental cases

Measurements for oxidation of hafnium carbide coating have been reported by Holcomb [29]. The carbide specimens were made by cutting a large hot-pressed compact into approximately 1.5 $\times$0.8 $\times$0.1 cm. Two experiments on the oxidation of hafnium carbide were conducted according to the temperature range by dividing the 1,200-1,530 degree range and the 1,800-2,200 degree range. A weight change test was conducted in the vertical reactor chamber for the low-temperature range. The specimen was placed on an alumina basket suspended by platinum wire and lowered into the furnace. Then the mass of the sample was recorded in real-time by an electronic balance. The test was performed under the condition that the total atmospheric pressure was 1 atm and the oxygen partial pressure was 0.02, 0.21, and 1.0 atm, respectively. In the temperature range over 1,800 degrees, the specimen was oxidized by heating the sample with a CO_2 laser and injecting air. In this case, the thickness of the oxide layer was measured after the test, and then the weight change was estimated,

assuming the density of dense hafnia.

5.2 Model results and validation

The results from the present model, earlier model, and experiments are plotted in Fig. 5.1. When calculating the model, a porosity of 0.02 and a pore radius of 0.01 microns were used as in previous studies. The horizontal axis represents the recip-

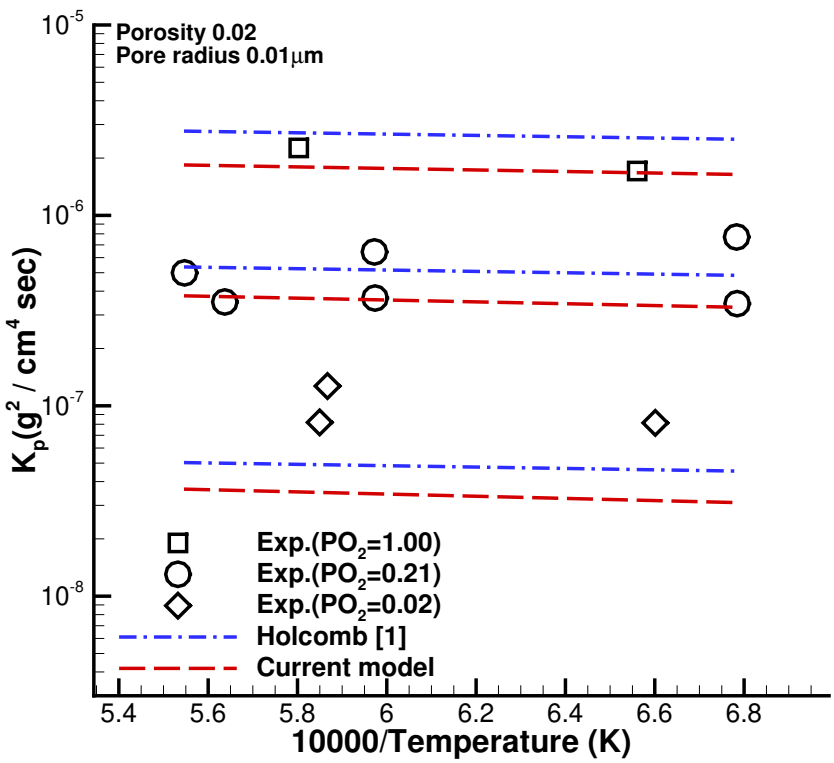

Figure 5.1: Comparison between HfC oxidation experiment and base model: pore radius 0.01 microns.

rocal of the temperature, and the vertical axis represents the weight growth layer of the oxide layer on a log scale. In the case of an oxygen partial pressure of 0.21 atm, both models belong to the range similar to the test results. Still, the existing model is close to the middle of the experimental values, and the current model calculates a low oxidation rate. When the partial pressure of oxygen is 1 atm, the previous model predicts more than the test result, and the current model measures less than the previous model. And when the oxygen partial pressure is 0.02 atm, both models are calculated lower than the test results.

For all three oxygen partial pressure conditions, the current model predicts 30 to 35% less than the previous model. Compared with the experiment, the current model is more incorrect than the previous model, but this is likely because the pore radius was set to 0.01 microns for calculation. As mentioned in the introduction, the average pore radius from hafnium oxide was much larger than 0.01 microns. So the model should agree with the experiment when the average size of pores inside the oxide layer is input to reflect the diffusion inside the oxide layer well physically. Thus the previous model over-predicts the oxygen diffusion through the oxide layer, and the current model predicts the correct oxide growth rate for the 0.01-micron pore radius. Since the effective diffusion coefficient is improved in the current model, the error in the existing model is improved, and the current model results show more physically accurate results.

5.3 Study on adjustable parameters

Wang [32] produced HfC coatings on C/C composites in various ways according to the precipitation parameters and then tested the oxidation/abrasive resistance performance of each. It was confirmed that a difference of about 2-3 times occurred in the oxidation resistance performance of the coating material. Therefore, measuring the porosity and pore radius generated after the experiment is necessary, and adjusting tortuosity to match the experimental results is essential. Adjustable parameters in the model are pore radius, porosity, tortuosity, and the restrictive factor. The influence of these parameters on the calculation results was examined.

Porosity and pore radius

First, the oxide layer growth rate according to the porosity is analyzed, as shown in Fig. 5.2. Fig. 5.2 is the result at 1,200K when the pore radius is fixed at 0.01 microns. The log value shows a difference of approximately two depending on the porosity. It is particularly affected as the porosity becomes smaller. The diffusion coefficient is affected by the porosity and the tortuosity, and it is considered that the currently applied tortuosity function greatly increases in the area of small porosity.

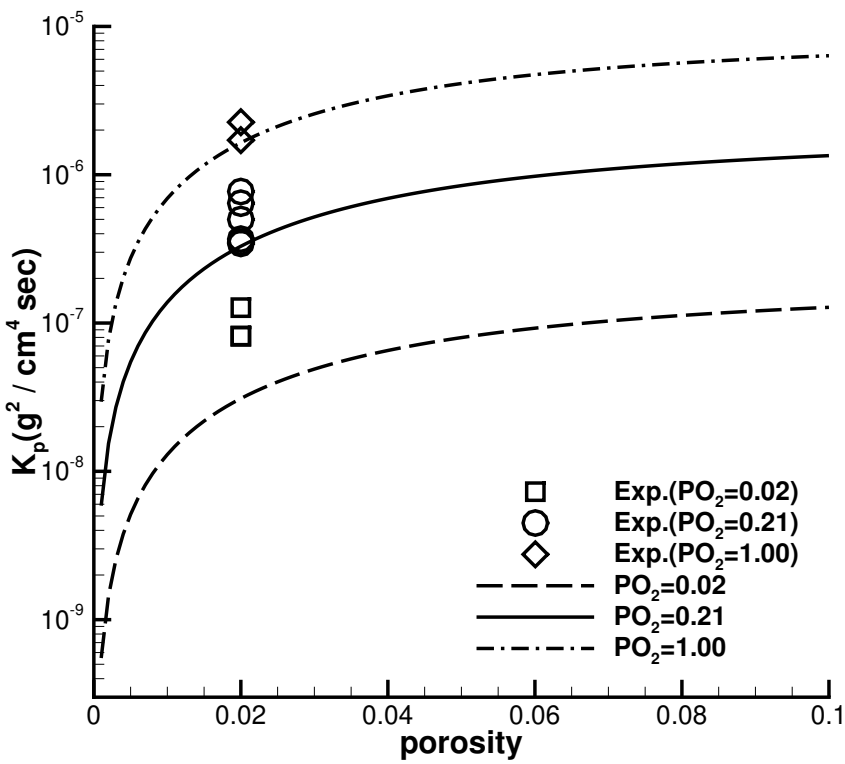

Figure 5.2: Oxide growth rate according to porosity.

When the porosity was fixed at 0.02, the effect of the pore radius on the oxidation rate was examined in Fig. 5.3. When the pore radius is larger than 0.02 microns, it does not have much impact, and within 0.02 microns, the pore radius starts to be significantly affected. In particular, it decreases rapidly in an area smaller than 0.01 µm. This area is presumed to be where the influence of Knudsen diffusion becomes extreme. When comparing the experimental results with the model results, the radius was set to 0.01 microns, close to the radius of pores formed directly on the carbide surface. A value much smaller than the average value observed in the actual experiment was used. Therefore, it is reasonable to use a larger value for the pore radius. Since the oxidation rate is almost constant when the radius is 0.02 microns or more, it will not matter if a larger value is set arbitrarily.

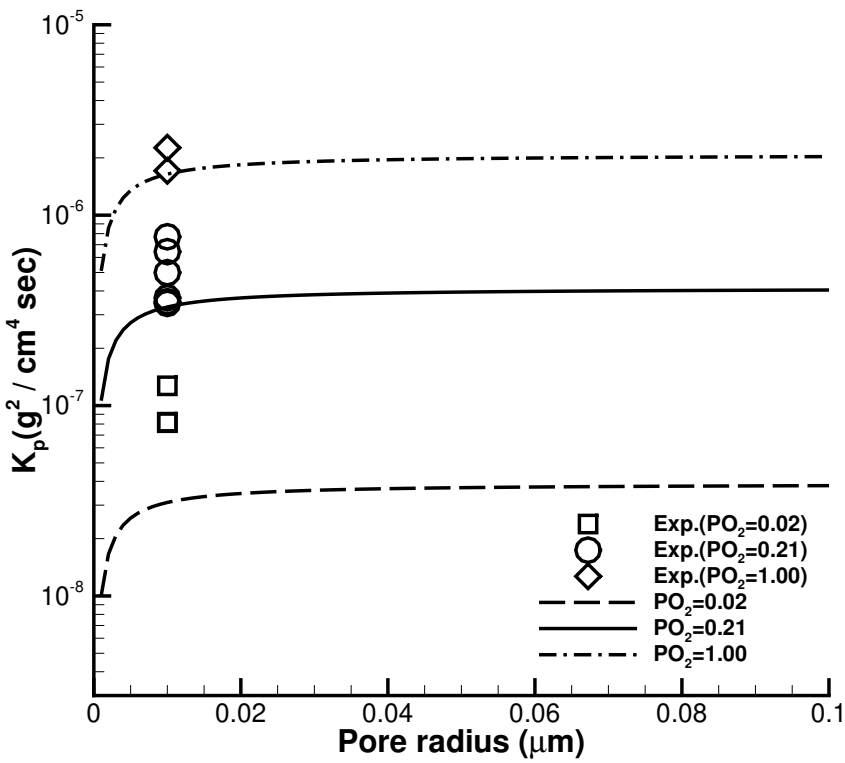

Figure 5.3: Oxide growth rate according to pore radius.

The pore radius range where the oxidation rate is constant can vary depending on the porosity. So The effects of the porosity and the pore radius are plotted together in Fig.5.4-5.6. The porosity ranged from 0.005 to 0.1, and the pore radius ranged from 0.001 microns to 0.2 microns. Fig. 5.4, 5.5, and 5.6 correspond to the conditions of 0.02 atm, 0.21 atm, and 1.0 atm of oxygen partial pressure, respectively. The porosity has a much more significant effect on the rate of oxide layer formation than the pore radius. The smaller the porosity, the smaller the pore radius becomes the starting point of the porosity-controlled zone in which the pore radius does not affect the oxidation rate. When the porosity is 0.1, the rapid change in the oxide growth rate stops at a pore radius of approximately 0.05 microns. Still, the oxidation rate slightly increases even in a pore radius bigger than that. These trends are all observed regardless of the oxygen partial pressure conditions. When comparing the model with the experimental results, the pore radius was set as 0.05, the result not to be affected by the pore radius.

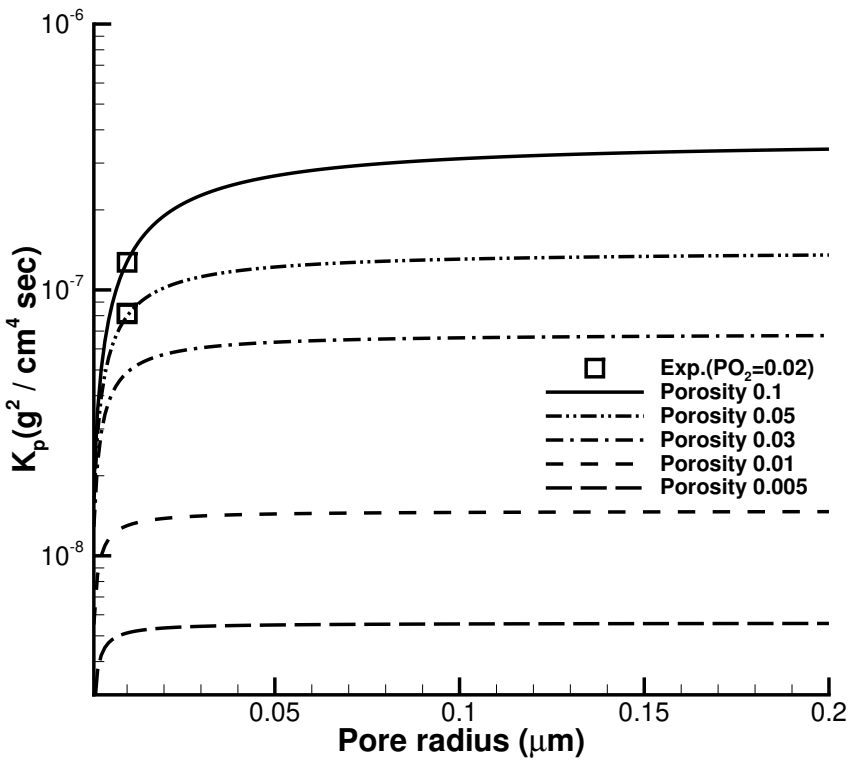

Figure 5.4: Oxide growth rate according to porosity and pore radius: P_{O_2} 0.02 atm, 1200 K.

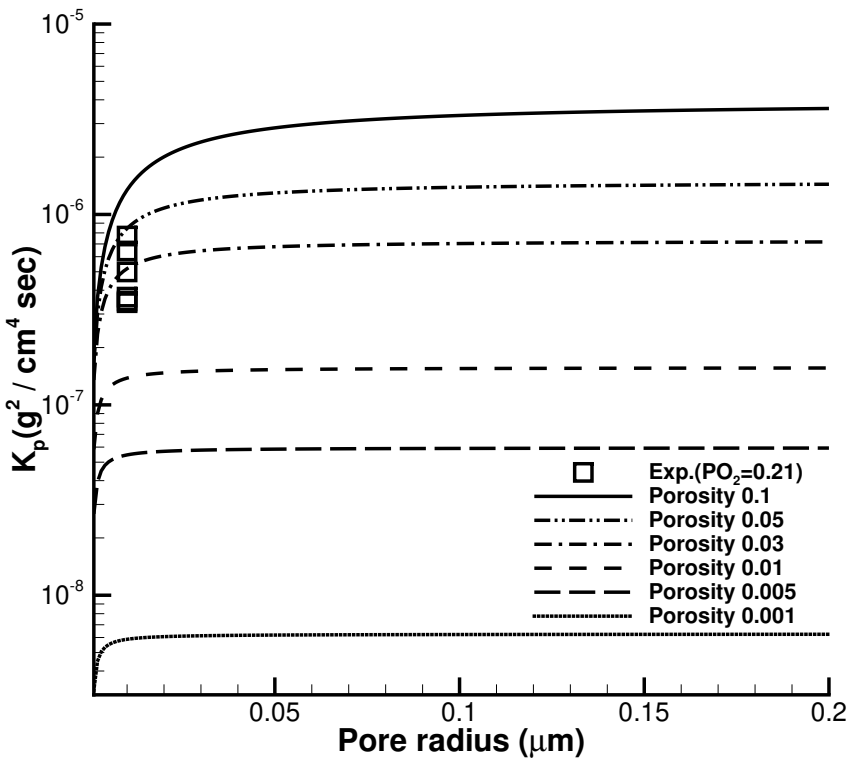

Figure 5.5: Oxide growth rate according to porosity and pore radius: P_{O_2} 0.21 atm, 1200 K.

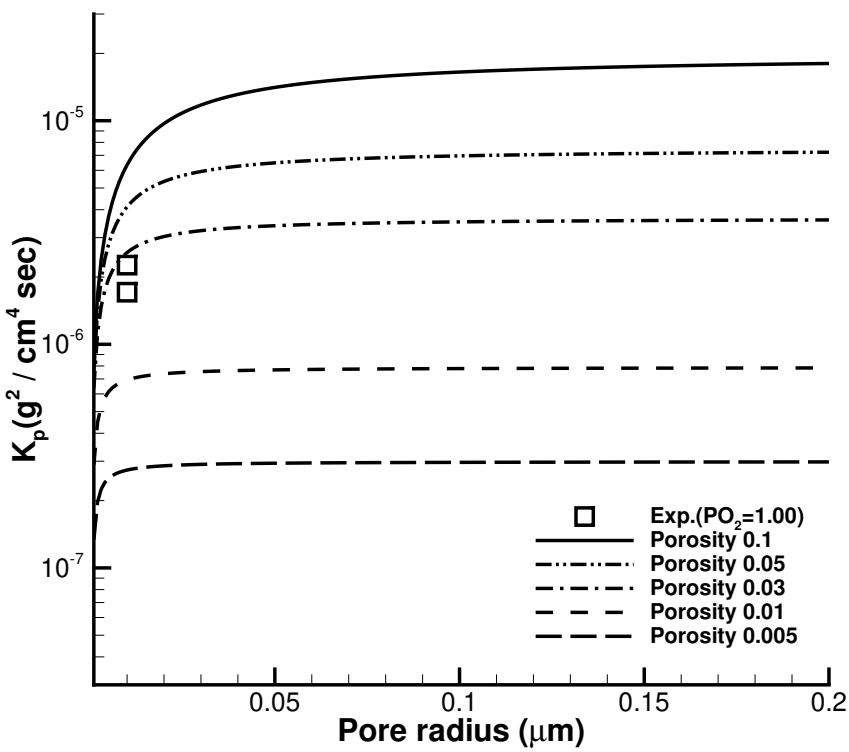

Figure 5.6: Oxide growth rate according to porosity and pore radius: P_{O_2} 1.00 atm, 1200 K.

The model results when the porosity is assumed to be 0.02 and the pore radius is 0.05 micro are compared with the experimental results and the model results when the pore radius is 0.01, as shown in the Fig. 5.7. As expected, the oxide layer growth rate was increased when the pore radius was 0.05. Under conditions of 1 atm and 0.21 atm of oxygen partial pressure, the values are similar to the experimental values. Still, at 0.02 atm, the oxidation rate is much lower than that of the experiment.

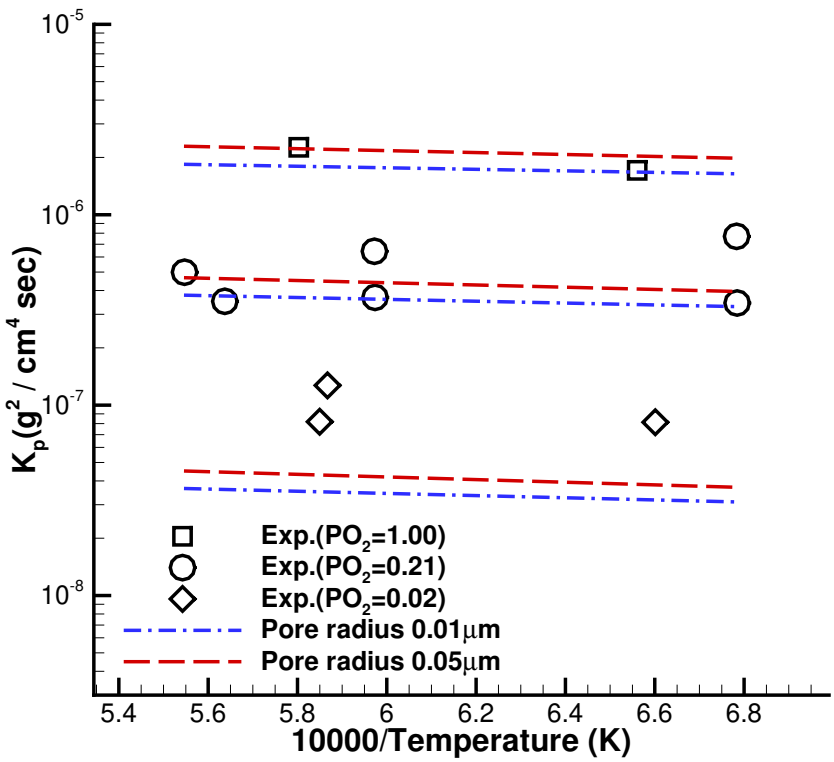

Figure 5.7: Model results compared with measurements: pore radius 0.01 and 0.05 microns.

The rate of increase is the same overall. The changing pattern can be more easily grasped by looking at the oxidation rate again with the horizontal axis as the oxygen partial pressure. It can be seen that the smaller the oxygen fraction, the smaller the tendency. For the model to match the experimental results, increasing the oxidation rate in the section where the oxygen fraction is low is necessary. However, it is difficult to seek a change in some areas because the change in temperature or pore radius brings about an overall uniform change.

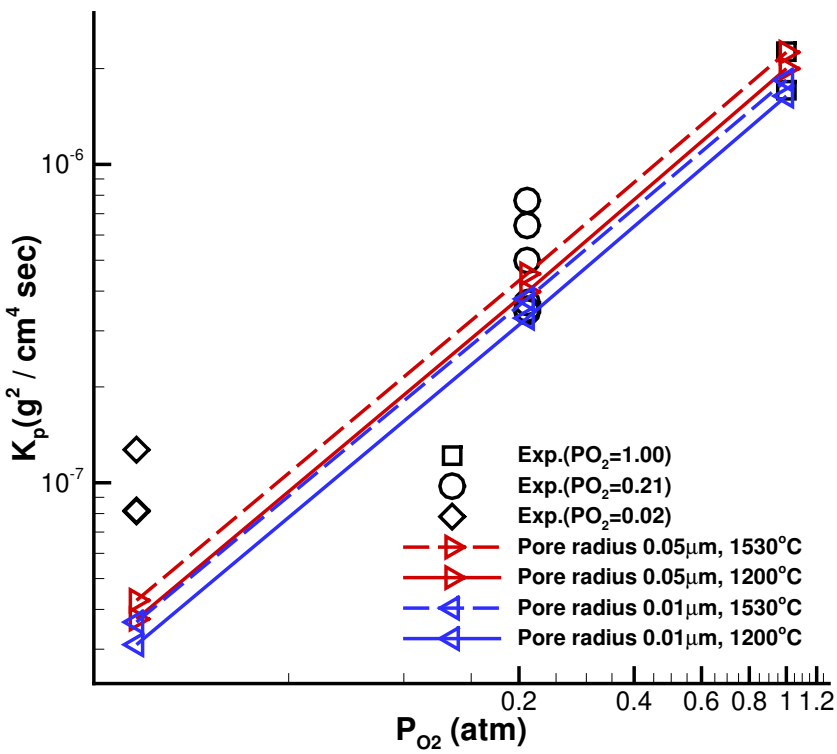

Figure 5.8: Oxide growth rate according to P_{O_2} and pore radius.

Tortuosity

The conditions of 0.21 atm and 1.00 atm of oxygen partial pressure agree with the experimental value. However, under the condition of 0.02 atm of oxygen partial pressure, it is measured at about 40% of the observed value. The tortuosity function was changed to solve this problem in this study. According to Holcomb, grains formed under 0.02 atm were very fine, unlike the cases where the oxygen partial pressure was 0.21 and 1.00 atm. When grains are finely formed, tortuosity usually decreases. The parameters of the tortuosity functions are often fitted to match the experiment in the porosity range of 0.1-0.5. So there is a high possibility of overestimating when porosity is as small as 0.02. It can be seen that the tortuosity tends to increase rapidly near the porosity of 0.02 in Fig. 3.2. The current model has a tortuosity value of about 4.78 at a porosity of 0.02. According to Chantong et al. [58], the tortuosity was approximately 1.4 when the grains were finely formed under a low oxidation layer growth rate. Therefore the tortuosity needs to be reduced when the oxidation reaction is low, such as in the oxygen partial pressure of 0.02 atm. There is a need. To develop the tortuosity function, the effect of tortuosity when the porosity is 0.02 was examined for each oxygen partial pressure and temperature condition. The range of tortuosity was set from 1 to 6.

Figs. 5.9 and 5.10 show the oxide growth rate as a function of tortuosity at an oxygen partial pressure of 0.21 atm. At a temperature of 1200, the model is similar to the experiment when the tortuosity is from 2 to 5. At a temperature of 1500, the model result fits the test data when the tortuosity is from 3 to 5. For those two temperatures, the tortuosity of 4 seems the most appropriate. The oxide growth rate as a function of tortuosity at an oxygen partial pressure of 0.02 atm is shown in Figs. 5.11 and 5.12.

At a temperature of 1200, the model is similar to the experiment when the tortuosity is from 1 to 2. When the temperature is 1500, the model result fits the test data when the tortuosity is from approximately 1.5 to 2. As mentioned above, these values are close to 1.4, corresponding to the case where the grains are finely formed. Figs. 5.13 and 5.14 show the oxide growth rate as a function of tortuosity at an oxygen partial pressure of 1 atm. At a temperature of 1200, the model is similar to the experiment when the tortuosity is from 4 to 5. When the temperature is 1530, the tortuosity value 4 to 5 fits the experimental data well. For those two temperatures, a tortuosity value between 4 and 5 seems the most appropriate. In summary, a model that fits the data well can be obtained if the tortuosity function has a value close to 1.4 when the oxide growth rate is low and has values between 4 and 5 when the oxide growth rate is sufficiently large.

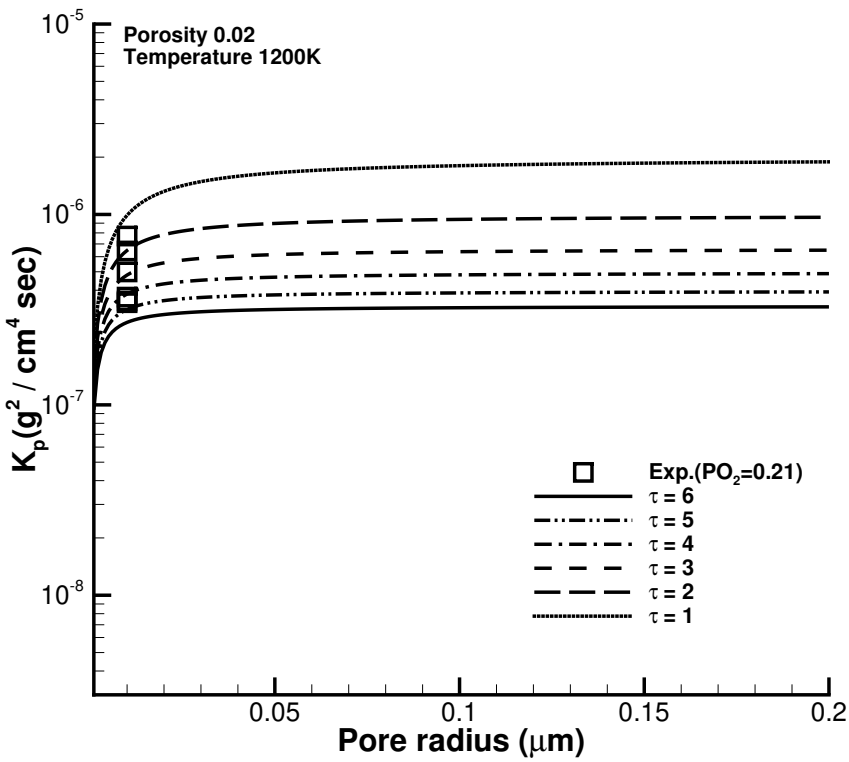

Figure 5.9: Oxide growth rate according to pore radius and tortuosity: porosity 0.02, P_{O2}=0.21 atm, 1,200K.

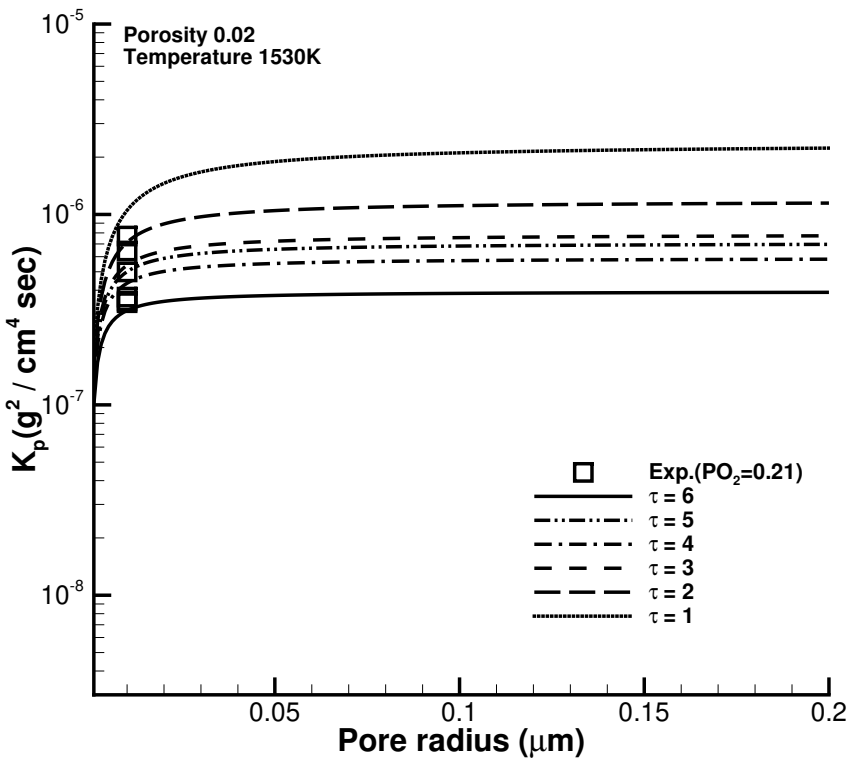

Figure 5.10: Oxide growth rate according to pore radius and tortuosity: porosity 0.02, P_{O2}=0.21 atm, 1,530K.

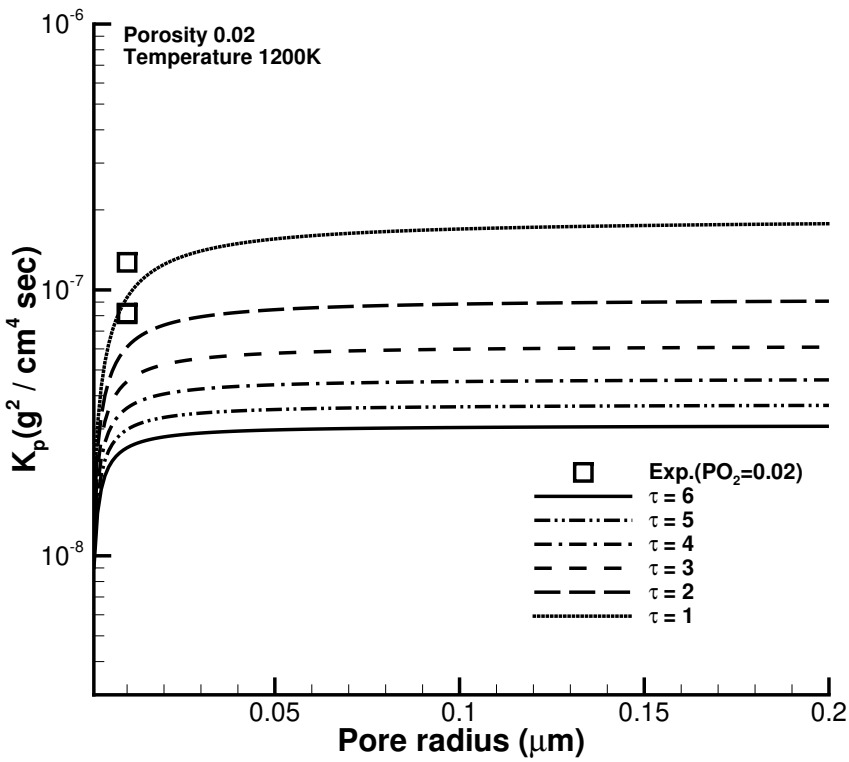

Figure 5.11: Oxide growth rate according to pore radius and tortuosity: porosity 0.02, P_{O2}=0.02 atm, 1,200K.

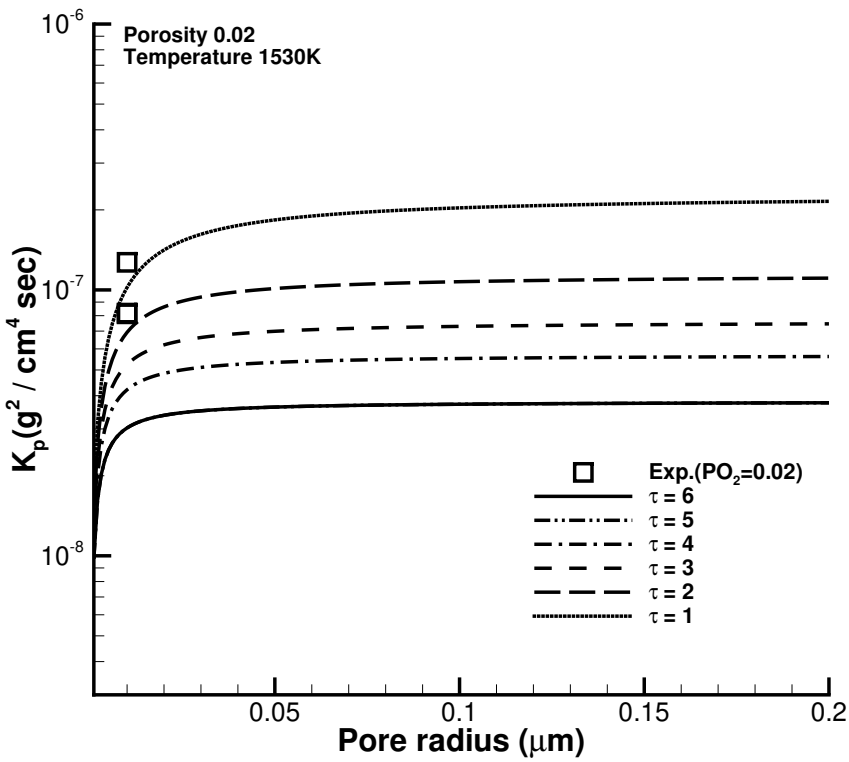

Figure 5.12: Oxide growth rate according to pore radius and tortuosity: porosity 0.02, P_{O2}=0.02 atm, 1,530K.

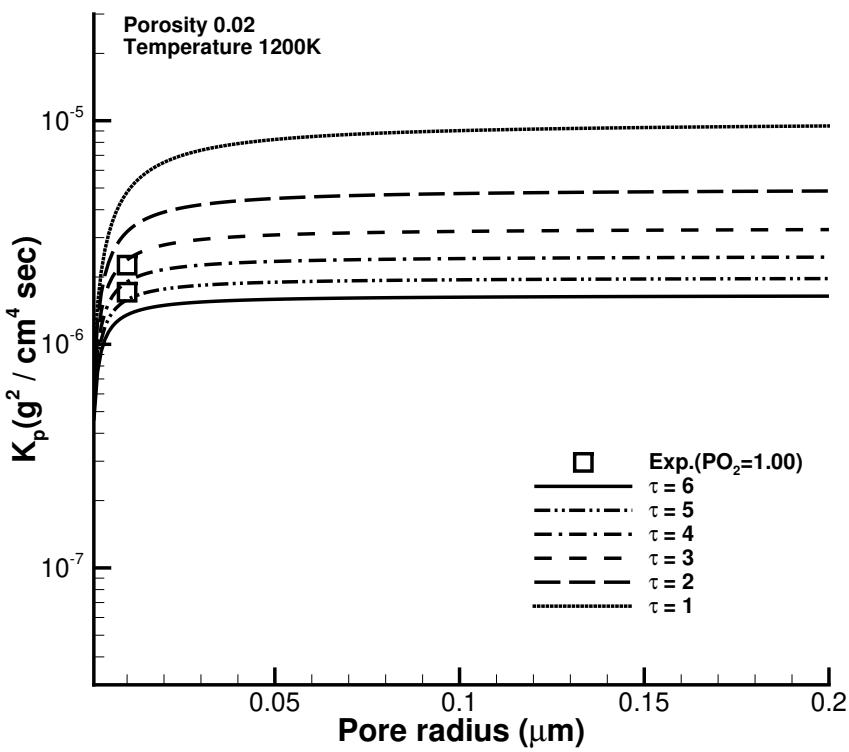

Figure 5.13: Oxide growth rate according to pore radius and tortuosity: porosity 0.02, P_{O2}=1.00 atm, 1,200K.

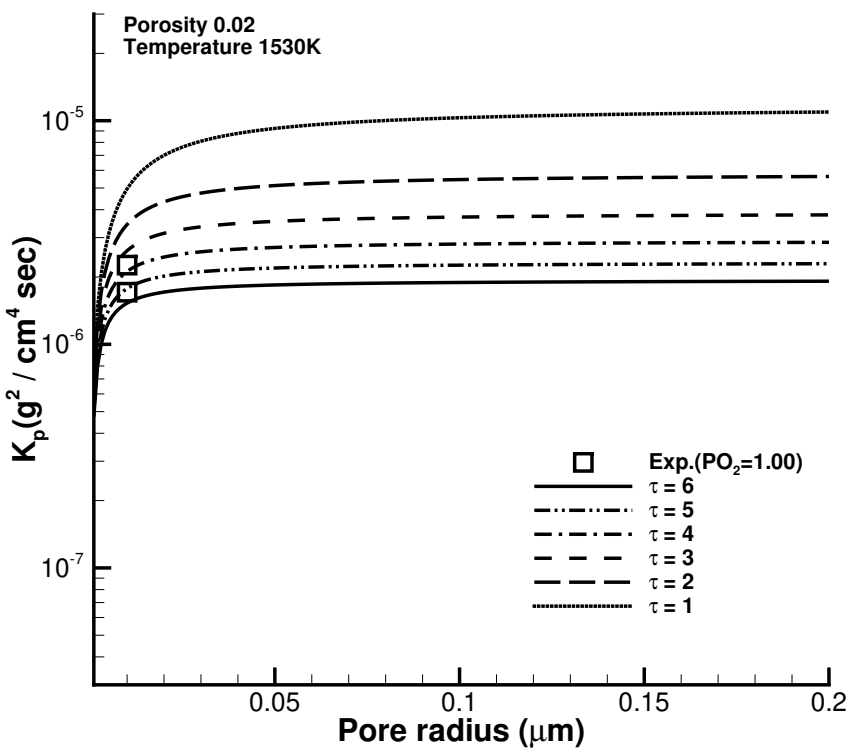

Figure 5.14: Oxide growth rate according to pore radius and tortuosity: porosity 0.02, P_{O2}=1.00 atm, 1,530K.

Tortuosity function

A tortuosity function is developed to fit the experimental data for all oxygen pressure conditions. The tortuosity goes to 1.4 when the oxide growth rate is extremely low, and the tortuosity goes to 5 when the growth rate is normal. The tortuosity function with the form of $\tau = \phi + y(1-\phi)$ is the most adjustable form among the typical types of tortuosity shown in Eq. (3.14). The adjustable parameter in the tortuosity function, y, is assumed to be a function of oxide weight growth rate k_p in $g^2/cm^2 - s$ as shown in Eq. (5.1) and Fig. 5.15.

$$\begin{aligned} \tau &= \epsilon + y(1-\epsilon) \\ y &= 1.3 \arctan 2(\log(k_p) + 6.5) + 3.4 \end{aligned} \tag{5.1}$$

Then the tortuosity value from the developed function is demonstrated in Fig. 5.16. Finally, the result from the model with modified tortuosity function is compared with the experimental data as shown in Fig. 5.17. The model predictions agree with the experimental data for all oxygen partial pressure conditions.

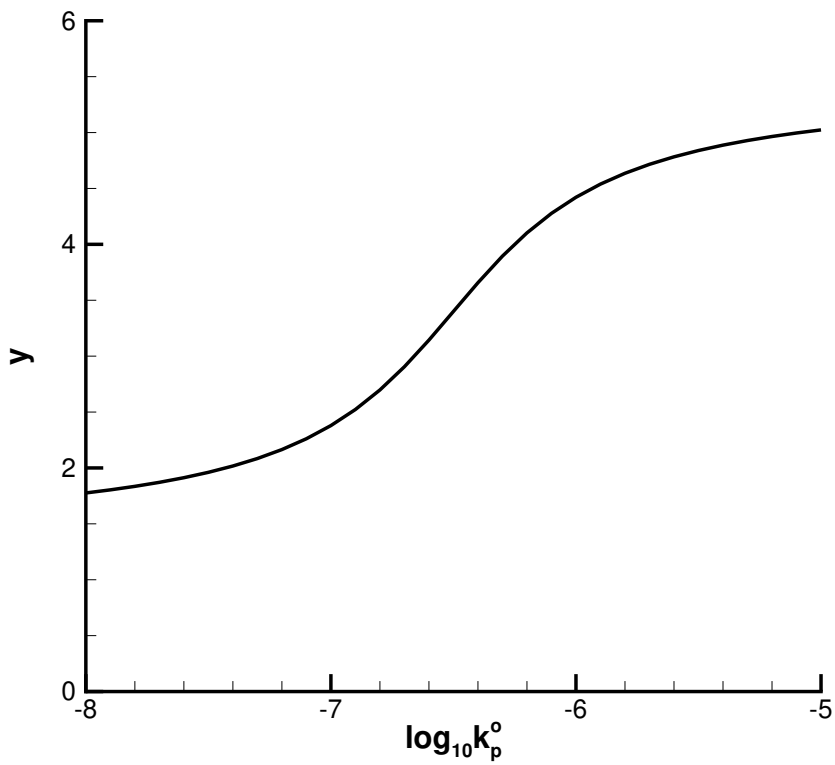

Figure 5.15: Designed y function for tortuosity model.

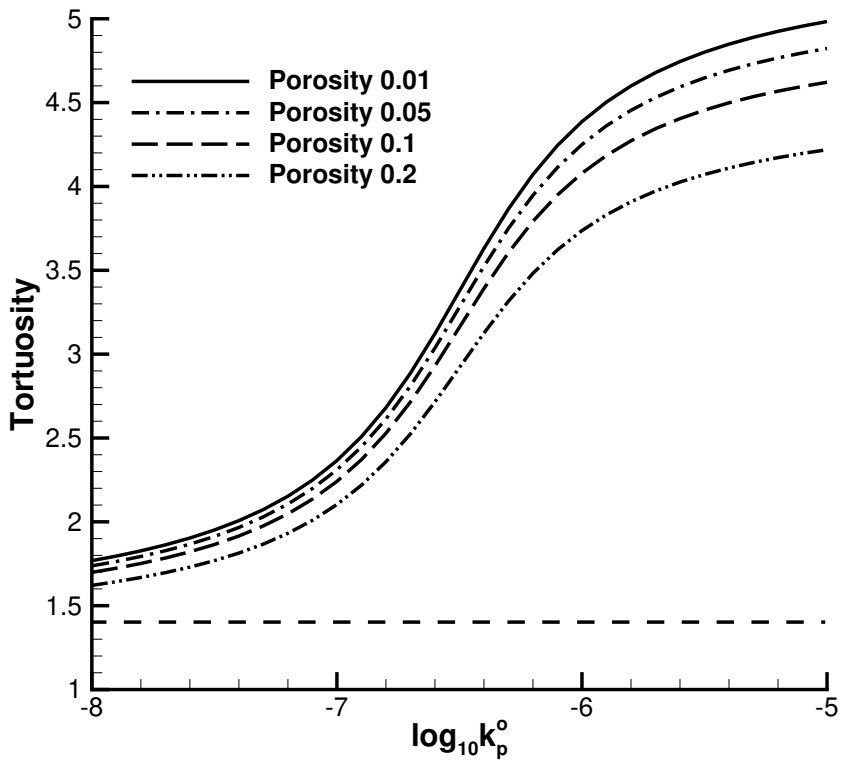

Figure 5.16: Designed tortuosity model.

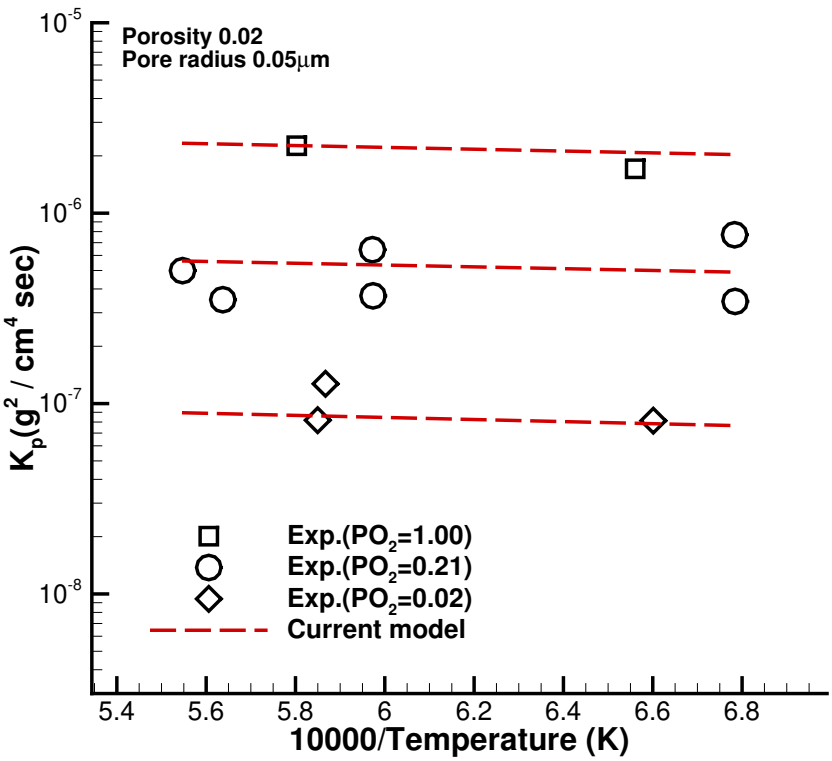

Figure 5.17: Final validation of the model with measurement.

High temperature range over 2,000 °C

A model result assuming the dissociation of an Oxygen molecule is compared with the experimental data in Fig. 5.18. Right triangle symbols on the left side with a '10000 / Temperature (K)' value of 4 to 4.8 are the experimental data in the temperature range of 1,800 °C to 2,200 °C. The blue line shows the results from the model without oxygen dissociation, and the red line shows the results assuming fully dissociated air. The predicted oxide growth rates from the model with dissociation were approximately 30 % higher than those without dissociation. The model results show good agreement with the test data when the temperatures are 1,800 °C and 2,000 °C. The experimental data of 2,200 °C is much bigger than the model result. The result at this temperature shows a considerable value that deviates significantly from the oxide growth rate trend that varied with temperature below 2,000 °C. This phenomenon can be explained in two ways. First, the reliability of the data is low because errors in the measurement process are expected. According to Holcomb, the oxide layer formation rate was estimated from the oxide layer thickness after the experiment without measuring the weight in real-time in the region of 1,800 degrees or more. Since it is an oxide growth rate estimated in this process, there may be errors. Also, it was mentioned that the void size was three times larger, unlike the case of up to 1,800 degrees. Therefore, the porosity may also be larger than in other experiments. The green line in Fig. 5.18 is a result when porosity is 0.06 at 2,200 K. Suppose a similar value is measured when repeated measurements are made over 2,000 degrees or more in the future. In that case, it will be possible to select parameters such as porosity and tortuosity suitable for this case by referring to the modeling process mentioned earlier.

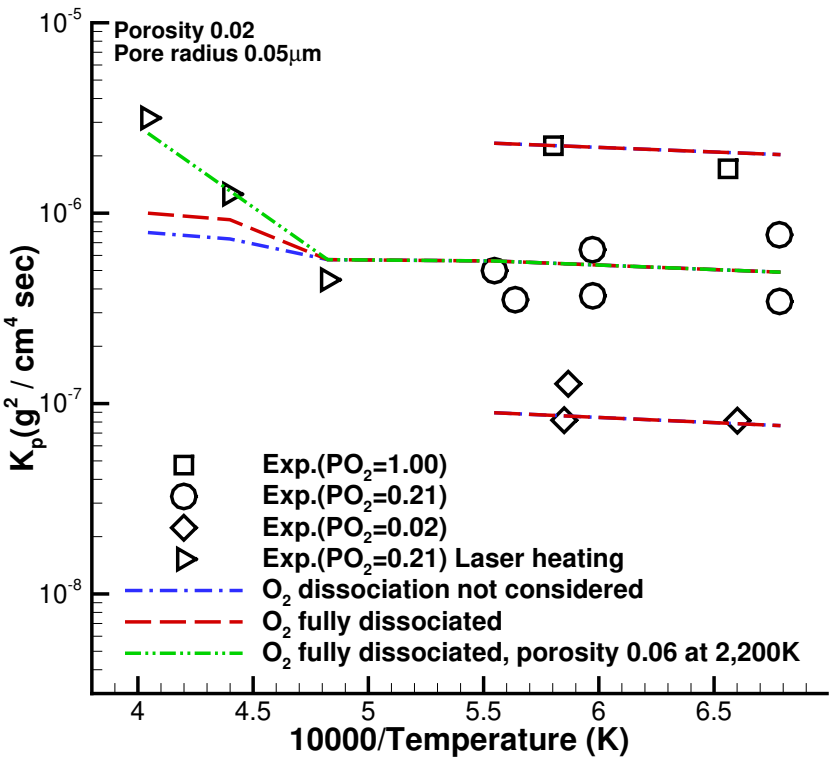

Figure 5.18: Oxide growth rate from the model with dissociation.

Chapter 6

Conclusions, Limitations, and Future Research

Conclusions

Models for predicting high-temperature oxidation through cracks and pores in oxidation protective coating layers were developed. First, an improved diffusion model for the prediction of the oxidation attack through oxidation-resistant coating cracks or slots was developed and validated at temperatures ranging from 1000 °C to 1300 °C. In addition to the assumptions made for previous counter-current gaseous diffusion models, four new assumptions were made while deriving the current model. The model was developed based on the original form of the MS equation, so it was improved to satisfy the law of mass conservation inside the path. The multi-component impact on diffusion has been investigated. The model based on ternary diffusion indicated a 6–7% reduction in the predicted values. Furthermore, the position of the flame front has been improved to move inward as the cavity grows. The reflection of the moving flame front exhibited no difference in the results for cases with craze cracks; however, the consideration increased the calculated rates up to 40% for cases with wide slots. The location of the flame front was assumed to be inside the crack.

However, there were cases where it was inside the cavity. Therefore, a model wherein the flame front was assumed to be inside the cavity was also studied. The results indicate that the oxidation model was not affected by the position of the flame front; it was only influenced by the diffusion path geometry. Finally, the diffusion through the intermediate space between $z = 0$ and $r = r_1$, which was neglected in the past models, was also considered in this study. The diffusion through the intermediate region also indicated no difference for the craze crack cases; however, the predicted rate decreased as the slot width increased.

The current model predicts oxidation rates in agreement with previously published experimental results, both for craze crack cases with extremely narrow crack widths and artificial slot cases with wide slot widths similar to the coating thickness. Therefore, this model adequately describes the kinetics of the oxidation attack through coating cracks. Finally, the dependence of carbon weight loss on crack geometry was studied using the model. The weight loss increased as the crack width increased and crack thickness decreased. In addition, it increased as temperature rose and the partial pressure of oxygen increased. However, the increment of total pressure reduced the weight loss rate when the oxygen partial pressure was constant.

Secondly, an improved diffusion model for the prediction of the oxide growth rate through oxidized oxidation-resistant coating layer was developed and validated at temperatures ranging from 1200 °C to 2000 °C in air, from 1200 °C to 1600 °C in oxygen partial pressure of 0.02 atm and 1 atm. The model was developed from the simplified MS equation as the previous model, but the method to obtain the effective diffusion coefficient and tortuosity is modified. The model with the modified effective diffusion coefficient showed an approximately 30-35% reduction in the predicted value. The previous model agreed with the experimental data when it used a pore

radius much smaller than the actual radius measured. However, the developed model can fit the test data with the actual pore radius at air and 1 atm oxygen partial pressure. The tortuosity function is also developed to fit the test data at 0.02 oxygen partial pressure because the grain size from the 0.02 condition differed from others. The tortuosity function was designed to have a value of 1.4 when the oxide growth rate is extremely low and approximately 5 when the oxide growth rate is high. Then the model for dealing with the dissociated oxygen is additionally developed. The model with dissociated oxygen indicated a 30% increment in the oxide growth rate.

The gaseous partial pressure at the surface and the temperatures are input conditions. The pore radius, porosity, and tortuosity are adjustable parameters that can be defined based on test data. The pore radius significantly affects the model result when the radius is smaller than approximately 0.02 microns. However, the pore radius has little impact when larger than 0.05 microns. The influence of porosity and tortuosity on the result is severe when porosity is smaller than approximately 0.1. Those modifiable factors can only evenly shift the growth rate for all oxygen partial pressure and temperature. If some tuning is needed only for some partial pressure or temperature range, the factor should be designed as a function of the oxide growth rate or temperature. Models developed in this study can be used to predict the performance of oxidation protective layer coatings, particularly SiC, HfC, and ZrC coated on C/C substrate for the operating temperature range of the coating material and wide pressure range.

Limitations and future research

Although the model developed in this study shows similar results to the experiment, there are still limitations due to simplification or assumptions in the modeling pro-

cess. Thus models can be improved through additional research acquisition in the future. First, the model was developed by assuming that the thickness of the coating, the width of cracks, the porosity of the oxide layer, and the pore radius were constant by taking average values. However, in reality, crack width, porosity, and pore radius exist differently depending on the thickness direction depth of the coating. In this study, when comparing the experimental results and the model, the width value of the surface side was used for the crack width, and the average porosity value was used for the porosity. It is necessary to study which values are similar to those of the test through further comparison of the experiment and the model. In addition, crack geometry was measured before heating, and the porous oxide values were measured from the specimen cooled to room temperature after the test. It is necessary to study the difference between the values before, after, and during the heating.

Next, in this study, the test for uniform high-temperature flow applied to the surface of an approximately 2-cm-sized specimen was compared with the model. But the flow applied to the surface of the coating layer of the actual vehicle is not uniform. The tendency of the crack formation may vary due to the curvature that varies depending on the surface position, and the properties of the oxide layer generated may vary depending on the surface temperature or flow characteristics. The model must reflect the crack and oxide layer parameters, which are different depending on the position when applied to 2D or 3D analysis. Meanwhile, when the coating is used for an aircraft, cracks are more likely to occur than in the case of a small specimen. Therefore, rather than making the sample smaller, it is thought that cutting a large specimen like Holcomb's test to make a small specimen will show a tendency that is more similar to the real one.

Finally, this model will be adapted into a conjugate analysis of hypersonic flow

and structure thermal response and applied to predict the damage on the carbon insulator under the oxidation protective coating during operation if the adjustable parameters of the model are further tuned for specific material. The modeling procedure can be applied to other systems such as oxidation attack through pinholes [11], notch defects [68], and hole defects caused by impact force [24]. Model developing methods and procedures in this study will be applicable because the kinetics of oxidation are similar.

Chapter A

Appendix

Table A.1: Molecular weight and Lennard-Jones parameters of gas molecules [47, 69].

Gas species	Molecular weight	Lennard-Jones parameters	
	$M(g/mol)$	ϵ/k (K)	σ(Å)
N_2	28.02	91.5	3.681
O_2	32.00	113	3.433
CO_2	44.01	190	3.996
CO	28.01	110	3.590
O^a	16.00	30.19	3.12
NO	30.01	119	3.470

[a] L-J parameters from supporting information of Lin. [70]

Table A.2: Density, molar mass, and molar volume of coating materials.

Material	Density (g/cm^3)	Molar mass (g/mol)	Molar volume (cm^3/mol)
SiC	3.16	40.28	12.75
SiO_2	2.196	60.08	27.36
ZrC	6.73	103.235	15.34
ZrO_2	5.68	123.218	21.69
HfC	12.1	190.50	15.34
HfO_2	9.68	210.49	21.74

Table A.3: Mass diffusivity [47, 69].

kT/ϵ_{ij}	$\Omega_{i,j}$	kT/ϵ_{ij}	$\Omega_{i,j}$	kT/ϵ_{ij}	$\Omega_{i,j}$	kT/ϵ_{ij}	$\Omega_{i,j}$
0.3	2.662	1.3	1.273	2.6	0.9878	4.6	0.8568
0.35	2.476	1.35	1.253	2.7	0.977	4.7	0.853
0.4	2.318	1.4	1.233	2.8	0.9672	4.8	0.8492
0.45	2.184	1.45	1.215	2.9	0.9576	4.9	0.8456
0.5	2.066	1.5	1.198	3	0.949	5	0.8422
0.55	1.966	1.55	1.182	3.1	0.9406	6	0.8124
0.6	1.877	1.6	1.167	3.2	0.9328	7	0.7896
0.65	1.798	1.65	1.153	3.3	0.9256	8	0.7712
0.7	1.729	1.7	1.14	3.4	0.9186	9	0.7556
0.75	1.667	1.75	1.128	3.5	0.912	10	0.7424
0.8	1.612	1.8	1.116	3.6	0.9058	20	0.664
0.85	1.562	1.85	1.105	3.7	0.8998	30	0.6232
0.9	1.517	1.9	1.094	3.8	0.8942	40	0.596
0.95	1.476	1.95	1.084	3.9	0.8888	50	0.5756
1	1.439	2	1.075	4	0.8836	60	0.5596
1.05	1.406	2.1	1.057	4.1	0.8788	70	0.5464
1.1	1.375	2.2	1.041	4.2	0.874	80	0.5352
1.15	1.346	2.3	1.026	4.3	0.8694	90	0.5256
1.2	1.32	2.4	1.012	4.4	0.8652	100	0.517
1.25	1.296	2.5	0.9996	4.5	0.861	200	0.4644

Table A.4: Equilibrium constants from NIST-JANAF Thermochemical Tables [51].

Temperature (K)	$\log K_f$		Temperature (K)	$\log K_f$	
	CO_2	CO		CO_2	CO
200	102.924	33.568	2100	9.858	7.322
298.15	69.095	24.03	2200	9.408	7.186
300	68.67	23.911	2300	8.998	7.062
400	51.539	19.11	2400	8.622	6.946
500	41.259	16.236	2500	8.275	6.84
600	34.404	14.32	2600	7.955	6.741
700	29.505	12.948	2700	7.658	6.648
800	25.829	11.916	2800	7.383	6.562
900	22.969	11.109	2900	7.126	6.481
1000	20.679	10.461	3000	6.886	6.404
1100	18.805	9.928	3100	6.661	6.333
1200	17.242	9.481	3200	6.45	6.265
1300	15.919	9.101	3300	6.251	6.201
1400	14.784	8.774	3400	6.064	6.14
1500	13.8	8.488	3500	5.888	6.082
1600	12.939	8.236	3600	5.721	6.027
1700	12.178	8.013	3700	5.563	5.974
1800	11.502	7.813	3800	5.413	5.924
1900	10.896	7.633	3900	5.27	5.876
2000	10.351	7.47	4000	5.134	5.83

Bibliography

[1] W. Hale and H. W. Lane, *Wings in orbit: scientific and engineering legacies of the Space Shuttle 1971-2010*. Government Printing Office, 2010.

[2] W. H. Heiser and D. T. Pratt, *Hypersonic airbreathing propulsion*. Aiaa, 1994.

[3] H. K. Rivers and D. E. Glass, "Advances in hot structure development," in *Thermal Protection Systems and Hot Structures*, vol. 631, 2006.

[4] C. W. Ohlhorst, D. E. Glass, W. E. Bruce III, M. C. Lindell, W. L. Vaughn, R. Dirling Jr, P. Hogenson, J. Nichols, N. Risner, and D. Thompson, "Development of x-43a mach 10 leading edges," in *56th International Astronautical Congress 2005*, no. Paper IAC-05-D2. 5.06, 2005.

[5] J. Young and R. Crippen, *Wings in Orbit: Scientific and Engineering Legacies of the Space Shuttle, 1971-2010*. Government Printing Office, 2011, vol. 3409.

[6] N. S. Jacobson, "High temperature chemistry at nasa: Hot topics," Tech. Rep., 2014.

[7] A. Paul, J. Binner, and B. Vaidhyanathan, "Uhtc composites for hypersonic applications," *Ultra-High Temperature Ceramics: Materials for Extreme Environment Applications*, pp. 144–166, 2014.

[8] A. Purwar and B. Basu, "Thermo-structural design of zrb2–sic-based thermal protection system for hypersonic space vehicles," *Journal of the American Ceramic Society*, vol. 100, no. 4, pp. 1618–1633, 2017.

[9] S. Mungiguerra, A. Cecere, R. Savino, F. Saraga, F. Monteverde, and D. Sciti, "Improved aero-thermal resistance capabilities of zrb2-based ceramics in hypersonic environment for increasing sic content," *Corrosion Science*, vol. 178, p. 109067, 2021.

[10] J.-F. Justin, A. Julian-Jankowiak, V. Guérineau, V. Mathivet, and A. Debarre, "Ultra-high temperature ceramics developments for hypersonic applications," *CEAS Aeronautical Journal*, vol. 11, no. 3, pp. 651–664, 2020.

[11] N. S. Jacobson, T. A. Leonhardt, D. M. Curry, and R. A. Rapp, "Oxidative attack of carbon/carbon substrates through coating pinholes," *Carbon*, vol. 37, no. 3, pp. 411–419, 1999.

[12] B. E. Deal and A. Grove, "General relationship for the thermal oxidation of silicon," *Journal of applied physics*, vol. 36, no. 12, pp. 3770–3778, 1965.

[13] Y. Song, S. Dhar, L. C. Feldman, G. Chung, and J. Williams, "Modified deal grove model for the thermal oxidation of silicon carbide," *Journal of Applied Physics*, vol. 95, no. 9, pp. 4953–4957, 2004.

[14] S. Chen, Y. Zeng, X. Xiong, H. Lun, Z. Ye, T. Jiang, L. Yang, J. Zhang, L. Liu, G. Wang *et al.*, "Static and dynamic oxidation behaviour of silicon carbide at high temperature," *Journal of the European Ceramic Society*, vol. 41, no. 11, pp. 5445–5456, 2021.

[15] T. Parthasarathy, R. Rapp, M. Opeka, and R. Kerans, "A model for the oxidation of zrb2, hfb2 and tib2," *Acta Materialia*, vol. 55, no. 17, pp. 5999–6010, 2007.

[16] T. A. Parthasarathy, R. A. Rapp, M. Opeka, and R. J. Kerans, "Effects of phase change and oxygen permeability in oxide scales on oxidation kinetics of zrb2 and hfb2," *Journal of the American Ceramic Society*, vol. 92, no. 5, pp. 1079–1086, 2009.

[17] M. Bykowski, A. Hudgins, R. Deacon, and A. Marder, "Failure analysis of the space shuttle columbia rcc leading edge," *Journal of Failure Analysis and Prevention*, vol. 6, no. 1, pp. 39–45, 2006.

[18] N. S. Jacobson and R. A. Rapp, "Thermochemical degradation mechanisms for the reinforced carbon/carbon panels on the space shuttle," Tech. Rep., 1995.

[19] J. A. Dever, M. V. Nathal, and J. A. DiCarlo, "Research on high-temperature aerospace materials at nasa glenn research center," *Journal of Aerospace Engineering*, vol. 26, no. 2, pp. 500–514, 2013.

[20] X. Yang, C. Zhao-hui, and C. Feng, "High-temperature protective coatings for c/sic composites," *Journal of Asian Ceramic Societies*, vol. 2, no. 4, pp. 305–309, 2014.

[21] S.-K. Lee, W. Ishida, S.-Y. Lee, K.-W. Nam, and K. Ando, "Crack-healing behavior and resultant strength properties of silicon carbide ceramic," *Journal of the European Ceramic Society*, vol. 25, no. 5, pp. 569–576, 2005.

[22] X. Yin, L. Cheng, L. Zhang, N. Travitzky, and P. Greil, "Fibre-reinforced multifunctional sic matrix composite materials," *International Materials Reviews*, vol. 62, no. 3, pp. 117–172, 2017.

[23] K. Ogi, T. Okabe, M. Takahashi, S. Yashiro, A. Yoshimura, and T. Ogasawara, "Experimental characterization of high-speed impact damage behavior in a three-dimensionally woven sic/sic composite," *Composites Part A: Applied Science and Manufacturing*, vol. 41, no. 4, pp. 489–498, 2010.

[24] H. Mei, D. Zhang, J. Xia, C. Yu, and L. Cheng, "The effect of hole defects on the oxidation behaviour of two-dimensional c/sic composites," *Ceramics International*, vol. 42, no. 14, pp. 15 479–15 484, 2016.

[25] H. W. Gehman, *Columbia accident investigation board report*. Columbia Accident Investigation Board, 2003, vol. 2.

[26] D. J. Roth, N. S. Jacobson, R. W. Rauser, R. A. Wincheski, J. L. Walker, and L. A. Cosgriff, "Nondestructive evaluation (nde) for characterizing oxidation damage in cracked reinforced carbon–carbon," *International Journal of Applied Ceramic Technology*, vol. 7, no. 5, pp. 652–661, 2010.

[27] S. Yurgartis, M. Bush, and B. Mast, "Morphological description of coating cracks in sic coated carbon-carbon composites," *Surface and Coatings Technology*, vol. 70, no. 1, pp. 131–142, 1994.

[28] N. S. Jacobson and D. M. Curry, "Oxidation microstructure studies of reinforced carbon/carbon," *Carbon*, vol. 44, no. 7, pp. 1142–1150, 2006.

[29] N. S. Jacobson, D. J. Roth, R. W. Rauser, J. D. Cawley, and D. M. Curry, "Oxidation through coating cracks of sic-protected carbon/carbon," *Surface and Coatings Technology*, vol. 203, no. 3-4, pp. 372–383, 2008.

[30] T. Aoki, H. Hatta, K. Goto, and H. Fukuda, "Characterization of coating cracks in oxidation-resistant sic coating on c/c composites," in *Proceedings of the*

Eighth Japan-US Conference on Composite Materials. CRC Press, 2019, pp. 409–416.

[31] Y.-l. Wang, X. Xiong, X.-j. Zhao, G.-d. Li, Z.-k. Chen, and W. Sun, "Structural evolution and ablation mechanism of a hafnium carbide coating on a c/c composite in an oxyacetylene torch environment," *Corrosion science*, vol. 61, pp. 156–161, 2012.

[32] Y.-l. Wang, X. Xiong, G.-d. Li, H.-f. Liu, Z.-k. Chen, W. Sun, and X.-j. Zhao, "Ablation behavior of hfc protective coatings for carbon/carbon composites in an oxyacetylene combustion flame," *Corrosion science*, vol. 65, pp. 549–555, 2012.

[33] G. R. Holcomb, *The high temperature oxidation of hafnium-carbide*. The Ohio State University, 1988.

[34] C. B. Bargeron, R. C. Benson, R. W. Newman, A. N. Jette, and T. E. Phillips, "Oxidation mechanisms of hafnium carbide and hafnium diboride in the temperature range 1400 to 2100 c," *Johns Hopkins APL Technical Digest;(United States)*, vol. 14, no. 1, 1993.

[35] H.-I. Yoo, H. S. Kim, B. G. Hong, I.-C. Sihn, K.-H. Lim, B.-J. Lim, and S. Y. Moon, "Hafnium carbide protective layer coatings on carbon/carbon composites deposited with a vacuum plasma spray coating method," *Journal of the European Ceramic Society*, vol. 36, no. 7, pp. 1581–1587, 2016.

[36] J. Bernstein and T. B. Koger, "Carbon film oxidation-undercut kinetics," *Journal of the Electrochemical Society*, vol. 135, no. 8, p. 2086, 1988.

[37] E. Courtright, J. Prater, G. Holcomb, G. S. Pierre, and R. Rapp, "Oxidation of hafnium carbide and hafnium carbide with additions of tantalum and praseodymium," *Oxidation of metals*, vol. 36, no. 5, pp. 423–437, 1991.

[38] G. Holcomb and G. S. Pierre, "Application of a counter-current gaseous diffusion model to the oxidation of hafnium carbide at 1200 to 1530° c," *Oxidation of metals*, vol. 40, no. 1, pp. 109–118, 1993.

[39] J. L. Smialek and N. S. Jacobson, "Oxidation of high-temperature aerospace materials," *High temperature materials and mechanisms*, pp. 95–162, 2014.

[40] S. G. Zhou, X. Liu, and Y. J. Guo, "Simulation of oxidation damage of coating crack on carbon/carbon matrix materials," *China Surface Engineering*, vol. 32, no. 2, pp. 154–162, 2019.

[41] T. Parthasarathy, R. Rapp, M. Opeka, and M. Cinibulk, "Modeling oxidation kinetics of sic-containing refractory diborides," *Journal of the American Ceramic Society*, vol. 95, no. 1, pp. 338–349, 2012.

[42] T. A. Parthasarathy, M. D. Petry, M. K. Cinibulk, T. Mathur, and M. R. Gruber, "Thermal and oxidation response of uhtc leading edge samples exposed to simulated hypersonic flight conditions," *Journal of the American Ceramic Society*, vol. 96, no. 3, pp. 907–915, 2013.

[43] G. Holcomb, "Countercurrent gaseous diffusion model of oxidation through a porous coating," *Corrosion*, vol. 52, no. 7, pp. 531–539, 1996.

[44] N. Jacobson, D. Roth, R. Rauser, J. Cawley, and D. Curry, "Oxidation of carbon/carbon through coating cracks," *ECS Transactions*, vol. 16, no. 44, p. 125, 2009.

[45] N. Jacobson, D. Hull, J. Cawley, and D. Curry, "Kinetics and mechanism of oxidation of the reinforced carbon/carbon on the space shuttle orbiter," in *Proceedings of 34th international conference and exposition on advanced ceramics and composites*, 2010, pp. 3–21.

[46] X. Chen, Z. Sun, H. Li, Y. Song, and X. Niu, "Modeling the effect of oxidation on the residual tensile strength of sic/c/sic minicomposites in stressed oxidizing environments," *Journal of Materials Science*, vol. 55, no. 8, pp. 3388–3407, 2020.

[47] R. Rapp and D. Shores, "Techniques of metals research, vol. iv," *Physicochemical Measurements in Metals Research, Part*, vol. 2, 1970.

[48] C. F. Curtiss and J. O. Hirschfelder, "Transport properties of multicomponent gas mixtures," *The Journal of Chemical Physics*, vol. 17, no. 6, pp. 550–555, 1949.

[49] S. Chapman and T. G. Cowling, *The mathematical theory of non-uniform gases: an account of the kinetic theory of viscosity, thermal conduction and diffusion in gases*. Cambridge university press, 1990.

[50] R. B. Bird, W. E. Stewart, and E. N. Lightfoot, "Transport phenomena, revised 2 nd edition," 2006.

[51] M. W. Chase and N. I. S. O. (US), *NIST-JANAF thermochemical tables*. American Chemical Society Washington, DC, 1998, vol. 9.

[52] L. Filipuzzi and R. Naslain, "Oxidation mechanisms and kinetics of 1d-sic/c/sic composite materials:ii, modeling," *Journal of the American Ceramic Society*, vol. 77, no. 2, pp. 467–480, 1994.

[53] Y. Zhao, Y. Chen, C. He, S. Ai, and D. Fang, "A damage-induced short-circuit diffusion model applied to the oxidation calculation of ceramic matrix composites (cmcs)," *Composites Part A: Applied Science and Manufacturing*, vol. 127, p. 105621, 2019.

[54] G. Yu, X. Shi, Y. Wang, J. Du, Z. Ni, X. Gao, F. Wang, and Y. Song, "An equivalent diffusion coefficient model of the oxidation of ceramic matrix composites," *Ceramics International*, 2021.

[55] L. B. Rothfeld, "Gaseous counterdiffusion in catalyst pellets," *AIChE Journal*, vol. 9, no. 1, pp. 19–24, 1963.

[56] L. Shen and Z. Chen, "Critical review of the impact of tortuosity on diffusion," *Chemical Engineering Science*, vol. 62, no. 14, pp. 3748–3755, 2007.

[57] B. Ghanbarian, A. G. Hunt, R. P. Ewing, and M. Sahimi, "Tortuosity in porous media: a critical review," *Soil science society of America journal*, vol. 77, no. 5, pp. 1461–1477, 2013.

[58] A. Chantong and F. E. Massoth, "Restrictive diffusion in aluminas," *AIChE journal*, vol. 29, no. 5, pp. 725–731, 1983.

[59] S. Kunze, R. Groll, B. Besser, and J. Thöming, "Molecular diameters of rarefied gases," *Scientific reports*, vol. 12, no. 1, pp. 1–12, 2022.

[60] M. Thommes, K. Kaneko, A. V. Neimark, J. P. Olivier, F. Rodriguez-Reinoso, J. Rouquerol, and K. S. Sing, "Physisorption of gases, with special reference to the evaluation of surface area and pore size distribution (iupac technical report)," *Pure and applied chemistry*, vol. 87, no. 9-10, pp. 1051–1069, 2015.

[61] N. Epstein, "On tortuosity and the tortuosity factor in flow and diffusion through porous media," *Chemical engineering science*, vol. 44, no. 3, pp. 777–779, 1989.

[62] K. Diao, L. Zhang, and Y. Zhao, "Measurement of tortuosity of porous cu using a diffusion diaphragm cell," *Measurement*, vol. 110, pp. 335–338, 2017.

[63] D. W. Richerson, *The magic of ceramics*. John Wiley & Sons, 2012.

[64] D. Bothe, "On the maxwell-stefan approach to multicomponent diffusion," in *Parabolic problems*. Springer, 2011, pp. 81–93.

[65] H. D. Vu and M. Nanko, "Crack-healing performance and oxidation behavior of sic dispersed yttrium silicate composites," *Journal of Asian Ceramic Societies*, vol. 8, no. 2, pp. 298–308, 2020.

[66] Z. Meng, T. W. Kim, S. M. Lee, and K. S. Lee, "Crack healing in the sic–sic ceramic matrix composites fabricated with different process," *Journal of the Korean Ceramic Society*, vol. 58, no. 1, pp. 86–93, 2021.

[67] H. Hatta, T. Aoki, H. Fukuda, and K. Goto, "Oxidation behavior modeling of ceramic coated carbon/carbon composites," in *Proceeding of the twelfth international conference on composite materials*, 1999.

[68] H. Mei, Y. Tan, P. Chang, S. Xiao, W. Huang, and L. Cheng, "Simplified approach to study oxidative damage of c/sic composites induced from notch defects," *Ceramics International*, vol. 45, no. 17, pp. 22 464–22 470, 2019.

[69] J. D. Anderson Jr, *Hypersonic and High-Temperature Gas Dynamics*, 3rd ed. American Institute of Aeronautics and Astronautics, Inc., 2019.

[70] L.-C. Lin, K. Lee, L. Gagliardi, J. B. Neaton, and B. Smit, "Force-field development from electronic structure calculations with periodic boundary conditions: applications to gaseous adsorption and transport in metal–organic frameworks," *Journal of Chemical Theory and Computation*, vol. 10, no. 4, pp. 1477–1488, 2014.

초 록

본 연구는 내산화 코팅층의 기공과 크랙을 통해 침투한 산소로 인해 발생하는 산화 현상을 예측하기 위한 모델 개발을 목표로 한다. 내산화층은 극초음속 유동 환경에서 산화에 취약한 탄소 소재의 내삭마 성능을 향상시키기 위해 사용된다. 그러나 코팅의 균열이나 산화된 내산화층에 존재하는 기공을 통해 산소가 침투하여 탄소 모재가 산화될 수 있다. 본 연구에서 개발된 모델은 carbon/carbon 모재를 방어하기 위한 내산화 코팅의 내산화 성능을 예측하기 위한 모델이다. 본 연구가 목표로 하는 소재는 실리콘 카바이드 (SiC), 하프늄 카바이드 (HfC), 지르코늄 카바이드 (ZrC)이며, 1,000 °C부터 이 소재의 용융점 이하의 온도 영역에서 모델링하였다. 크랙 모델은 마이크로미터 단위의 폭을 지난 미세한 크랙부터 밀리미터 단위의 큰 폭을 가진 균열을 통해 침투한 산소로 인해 탄소 모재가 산화되는 양을 예측한다. 기공 모델을 산화층의 기공을 통해 카바이드 층까지 확산된 산소로 인해 카바이드 내산화층이 산화층으로 변환되어 산화층이 생성되는 성장률을 예측한다.

크랙을 통한 산화를 예측하기 위한 모델은 완전한 형태의 다화학종 기체 확산 방정식으로부터 유도되었으며 탄소 모재에서 성장하는 구멍의 영향도 고려하였다. 모델 예측값은 기존 문헌의 실험 결과에 대해 검증되었다. 미세한 균열과 큰 폭의 균열에 대해 모두 검증되었으며, 우주왕복선의 재진입 환경인 1,000 °C부터 1,300 °C까지 검증되었다. 기존 모델은 시험 결과 대비 절반 이하의 값으로 예측하였으나 본 연구에서 개발된 모델은 시험 결과와 잘 일치하였다. 그리고 모델 개발

과정에서 가정된 요소들에 대해 각 요소들이 예측값에 미치는 영향을 분석하였다. 그리고 크랙의 형상과 대기 조건이 산화 속도에 미치는 영향을 분석하였다.

코팅의 산화층 생성을 예측하기 위한 모델은 유효 확산계수를 사용하는 단순화된 다화학종 기체 확산 방정식으로부터 유도되었다. 유효 확산계수는 Knudsen 확산과 다공성 물질의 영향을 고려한 분자 확산을 포함한다. 마찬가지로 기존 문헌의 실험 결과에 대해 검증되었다. 개발된 모델로부터 계산된 산화층 생성 속도는 공기 조건에 대하여 1,200 °C부터 2,000 °C까지, 그리고 0.02, 1 기압 산소 분압 조건에서는 1,200 °C부터 1,600 °C까지 제공된 시험 결과와 일치하는 경향을 보였다. 기공도, 기공 반지름, 비틀림 인자 등 모델에 포함된 조정가능한 파라미터가 예측 결과에 미치는 영향을 분석하였다.

주요어: 내산화층, 메탈카바이드 코팅, 코팅 크랙, 다공성 산화층, 산화층 성장
학번: 2014-21895